國立交通大學

電子工程學系 電子研究所

碩士論文

應用於非極性氮化鎵發光二極體元件以改善光萃取效率的極性選擇化學蝕刻

Integration of Nonpolar *A*-Plane Gallium Nitride Fabricating and Chemical Etching Processes for Lighting Efficiency Enhancement of Light-Emitting Diodes

研究生： 莊凱麟

指導教授： 張俊彥 院士

中華民國 九十九 年 七 月

應用於非極性氮化鎵發光二極體元件以改善光萃取效率的極性選擇化學蝕刻

Integration of Nonpolar *A*-Plane Gallium Nitride Fabricating and Chemical Etching Processes for Lighting Efficiency Enhancement of Light-Emitting Diodes

研究生：莊凱麟　　Student: Kai-Lin Chuang
指導教授：張俊彥 院士　　Advisor: Prof. Chun-Yen Chang

國立交通大學
電子工程學系　電子研究所
碩士論文

A Thesis
Submitted to Department of Electronics Engineering and
Institute of Electronics
College of Electrical and Computer Engineering
National Chiao Tung University
In Partial Fulfillment of the Requirements
For the Degree of Master
In
Electronics Engineering

July 2010
Hsinchu, Taiwan, Republic of China

中華民國 九十九 年 七 月

應用於非極性氮化鎵發光二極體元件以改善光萃取效率的極性選擇化學蝕刻

學生：莊凱麟　　　　　　　　　　　　指導教授：張俊彥 院士

國立交通大學 電子工程學系 電子研究所 碩士班

摘要

半導體發光二極體具有成為新世代高發光效率固態照明的特定必須條件，包含可調變發光頻譜以及材料磊晶特質…等等，其中三族氮化物可以磊晶形成具有藍光或紫外發光波段的多重量子井結構，而這正式實現白光固態照明所必需的光源。然而依據現有磊晶以及元件製程技術，依舊無法克服三族氮化物材料特性—非對稱晶體結構—所引發的特殊效應：量子侷限史塔克效應。此效應導致極性面三族氮化物材料中的電子電洞分佈機率最大值錯位，意即導電帶與價帶傾斜，使得電子電洞複合發光機率大幅下降，並間接導致低水平的「內部量子效益」。此外，如何有效將電子電洞複合產生的光子萃取出元件結構外，以直接對「照明」做出貢獻是另一項課題，因為此「光萃取效率」所影響的是「外部量子效益」，或者可通稱為半導體發光二極體的「發光效益」。

本篇論文包含了如何在溝渠圖形化的 m 面藍寶石基板上、溝渠圖形化的無極性 a 面氮化鎵模板上(磊晶於 γ 面藍寶石基板上)利用有機金屬化學氣相沉積方法磊晶出高結晶品質的無極性 a 面氮化鎵。利用在溝渠圖形化的 m 面藍寶石基板上成長高結晶品質無極性 a 面氮化鎵所得到的磊晶經驗，並將之應用到溝渠圖形化的無極性 a 面氮化鎵模板上，使用「溝渠圖形化側向磊晶成長方式」，可以

得到高結晶品質、平坦的無極性 a 面氮化鎵於 γ 面藍寶石基板上。在這一高品質的無極性 a 面氮化鎵基板上，無極性氮化銦鎵/氮化鎵多重量子井結構可以成功實現，並具有藍光 440nm 的發光波段。

此一有機金屬化學氣相沉積方法所依賴的實驗關鍵在於較低的五族/三族原子比例，其值大約 100。而成長模式主要依靠正 c 方向的快速成長面以達到側向完全癒合平坦的目標。使用「溝渠圖形化側向磊晶成長方式」所得到的高結晶品質、平坦的無極性 a 面氮化鎵，其差排密度可由初始 γ 面藍寶石基板上的 a 面氮化鎵的 $1\times10^{10}\text{cm}^{-2}$ 大幅降低到在側向成長區域的 $1\times10^{8}\text{cm}^{-2}$。本論文中並針對利用此兩種方式：「溝渠圖形化的 m 面藍寶石基板上磊晶」、「溝渠圖形化的無極性 a 面氮化鎵模板上磊晶」所得到的高結晶品質無極性 a 面氮化鎵進行分析，並搭配掃描式電子顯微鏡、穿透式電子顯微鏡進一步針對缺陷分布以及形成原因進行探究。

由於使用「溝渠圖形化側向磊晶成長方式」所得到的高結晶品質、平坦的無極性 a 面氮化鎵其存在特殊的孔洞於氮化鎵/γ 面藍寶石基板介面，因此本文中利用氫氧化鉀溶液針對這些因溝渠圖形化設計以及磊晶限制所留下的孔洞進行蝕刻處理。蝕刻處理所選定的試片包含了完整磊晶的無極性氮化銦鎵/氮化鎵多重量子井結構，以針對蝕刻分析是否對發光性質造成影響。氫氧化鉀溶液蝕刻條件控制在 100°C、120°C、140°C；濃度條件維持在 5 wt. %、10 wt. %以及 20 wt. %；蝕刻時間則選擇 10min、20min、40min、80min 以及 160min。藉由調整不同條件組合的蝕刻條件發現在低溫低濃度的狀況下，氫氧化鉀溶液對於存在高結晶品質、平坦的無極性 a 面氮化鎵/γ 面藍寶石基板介面的孔洞無顯著的蝕刻效果，蝕刻速率約為 2.35±1.67nm/min，速率慢且蝕刻差異大；高溫高濃度的狀況下則可以得到有效的蝕刻效果，蝕刻速率約為 26.0±1.90nm/min，速率雖快但蝕刻差異大。而中間溫度 120°C 以及 10 wt. %的組合提供了 13.6±0.90nm/min 的蝕刻速率，

具有可接受的蝕刻速率且蝕刻差異降低到 1nm/min 以下。

此一蝕刻方式可以將存在高結晶品質、平坦的無極性 a 面氮化鎵/γ 面藍寶石基板介面的孔洞蝕刻成由{11-22}面以及$+c$ 面所構成的等腰三角形、梯形或者因缺陷導致的混合形。這些蝕刻行為可歸類為「極性選擇蝕刻行為」以及「缺陷選擇蝕刻行為」。

進一步由變角度光激發光光譜量測可得知這些條狀的幾何形狀孔洞對於光萃取效率有顯著的提升，在垂直等腰三角孔洞側邊的方向上(約偏離法向量自 30°到 60°)可以得到 3 倍以上的光取出強度改善。藉由組合不同的蝕刻條件以及優化不同的孔洞幾何形狀，大角度範圍(自法向量到 60°以上)的光取出效率改善可被預期。

本論文成功整合高結晶品質、平坦的無極性 a 面氮化鎵的磊晶製程以及氫氧化鉀溶液的蝕刻製程以產生特殊形狀的孔洞，達到了同時針對內部量子效益(無極性材料性質)以及光萃取效益(蝕刻產生空氣孔洞)兩大影響半導體發光二極體發光效益的因素改善的目的。

Integration of Nonpolar *A*-Plane Gallium Nitride Fabricating and Chemical Etching Processes for Lighting Efficiency Enhancement of Light-Emitting Diodes

Student: Kai-Lin Chuang Advisor: Prof. Chun-Yen Chang

Department of Electronics Engineering and Institute of Electronics
National Chiao Tung University

Abstract

Based on semiconductor light-emitting diodes, solid state lighting is a promising approach for the realization of highly efficient white light sources. The Group-III nitrides materials provide a great potential of constructing the multiple quantum wells which can emit light in blue and UV region and be used as important sources of white lighting. However the asymmetry of the Group-III nitrides materials crystalline structure leads to an undesirable Quantum-Confined Stark Effect (QCSE) which is a barrier of the recombination of electrons and holes. Besides, guiding the emission light out of the devices is one another important issue for it determining the total lighting efficiency by light extraction efficiency.

In this thesis, the epitaxial growth of nonpolar *a*-plane GaN on trench-patterned *m*-plane sapphire and on trench-patterned *a*-plane GaN template with *γ*-plane sapphire by MOCVD was performed. The experimental knowledge was first constructed on the growth mode of *a*-plane GaN on trench-patterned *m*-plane sapphire and then applied to a modified technique, trench epitaxial lateral overgrowth (TELOG) on trench-patterned *a*-plane GaN template with γ-plane sapphire, and successfully gain the planar a-plane GaN and the corresponding InGaN/GaN MQWs on it. The critical growth methods, i.e. the low level of V/III ratio of ~100, growth mode, i.e. the +*c*-direction-dominated growth fronts, crystalline quality, i.e. dislocation density decreasing from 1×10^{10}cm^{-2} to 1×10^{8}cm^{-2} at lateral wing region, optical properties including photoluminescence (PL) and cathodoluminescence (CL) are observed in this thesis.

A chemical etching technique based on the KOH solution was applied to the TELOG *a*-plane GaN and InGaN/GaN MQWs. The etching conditions including the temperature between 100°C and 140°C, the concentration of KOH between 5 wt. % and 20 wt. % and the etching times: 10min, 20min, 40min, 80min and 160min. This integration provides air-voids with specific geometries, i.e. the isosceles triangle or trapezoid or the mixed one, in the nonpolar *a*-plane GaN. Under investigations, it provides great improvement of the light extraction ability at a wide range of direction. Based on the varied-angle PL measurement, an approximately 3 times enhancement of the PL intensity was achieved at the angle from 25° to 50° with respect to the normal direction of the sample surface. Furthermore, by the combination of the etching mechanisms and the techniques of substrate engineering, a possible chemical lift-off process is expected to be established.

The thesis provides an integrated process includes the fabrications of nonpolar *a*-plane GaN materials by TELOG and the etching procedures by KOH solution without extra damages, which would be a powerful solution to enhance the total

lighting efficiency from the factors of internal quantum efficiency and the light extraction efficiency at a same time.

誌謝

謹獻 **無限敬意**與**誠摯感謝** 與

指導教授 **張俊彥院士**。感謝老師提供無垠空間與以學生自由揮灑，並適時指明前進方向與途徑。感謝老師點亮學生的本質光芒與內斂、畢露的收放時宜。

口試委員：國立交通大學材料科學與工程學系 **張翼教授**、崑山科技大學 **蘇炎坤校長**。感謝悉心審閱論文並於口試期間不吝提出指正，以使論文更臻完整。

楊博(宗熺學長)：感謝您的帶領與指導而使 ECOE-Research-Group 得以順利運作，並為您的領導風範與表率表示敬意。

哲榮學長、博閔學長、世邦學長：感謝三位學長在 LED 領域的入門指導、實驗方向的指引、實驗技巧的傳授以及諸多實驗上的支援所提供的幫助，在此表示無盡感謝！此篇論文的架構與方向指導、2010 International Conference on Solid State Devices and Materials (SSDM)的投稿申請、2010 TSMC Outstanding Student Research Award 的申請……等諸多方面皆在三位學長指導下而有順利的過程與圓滿的結果。

亦感謝碩士班期間給予實驗上大量協助的 ECOE Research Group 成員：**怡誠學長、信淵學長、兆欽學長、弘斌學長、立偉學長、緯仁學長、耀峰學長、培維、朝淦、婉儀、昀瑾、林緯、祐誠、安城**；電物所**瑞泰學長**；材料所 CSD-Lab **延儀學長、家達學長、玉芳**；材料所 PKG-Lab **炯鑫學長**；光電所**鏡學學長、李鎮宇博士**；臺灣 ULVAC 研發中心**陳江耀先生、鄭凱文先生**；淡江大學**許世杰博士**；以及大學同學**胤誠、伯政、宏基**。祝福各位學業精進、平安順心。

ECOE-Research-Group 助理：**芝羽**，感謝對於實驗室日常事務、計畫事務…等的細心處理，以及在研究助理一職的申請上給予協助。

最後，感謝摯愛的家人、永遠的精神支柱：祖父**莊榮輝**、祖母**莊阮濆**、父親**莊岳忠**、母親**陳彩鳳**以及三個妹妹**涵雅**、**鈺欣**、**婉茹**。

Acknowledgement

The contribution of many people that made this work possible and helped me in immeasurable ways is recognized and gratefully acknowledged.

Professor Chun-Yen Chang: for the opportunity to be a member of his group, ECOE Research Group, his continued guidance and supports, and commitment to excellence in teaching and advising.

Professor Edward-Yi Chang and **Professor Yan-Kuin Su**: for being respected teachers and researchers and graciously agreeing to be part of my Master committee.

Dr. Tsung-His Yang: for his leading the ECOE Research Group and the guidance to a rookie in research realm.

Predecessors of ECOE Research Group: **Jet-Rung Chang**, **Po-Min Tu** and **Shih-Pang Chang**: for their expertise advice and help in so many areas about LED, epitaxy, experiments and for they making the results emerge in large numbers every day.

The ECOE Research Group staff, past, present and related, who have experienced the precious triumphs and frustrations with me: **Yi-Cheng Chen**, **Yuen-Yee Wong**, **Dr. Wei-Ren Chen**, **Jui-Tai Ku**, **Kevin Cheng**, **Yao-Feng Chang**, **Shin-Yuan Wang**, **Pei-Wei Chiang**, **Li-Wei Feng**, **Chris Yang**, **Wei Lin**, **Yun-Jin Li**, **Ching-Hsueh Chiu**, **Yu-Cheng Hsu**, **Wan-Yi Chen**, **Chiang-Yao Chen**, **An-Cheng Liu**, **Dr. Chao-Chin Cheng**, **Hong-Bin Chen**, **Chia-Da Chang**,

Jiong-Xin Wang, **Dr. Chen-Yu Li**, **Bo-Cheng Lai**, **Hong-Ji Wu**.

My ex-college mate, **Yin-Hsian Huang**, a great friend through it all, for encouragement of pursuing the beauty and truth of academic world.

The assistant of ECOE Research Group, **Shela Lin,** and all of her organizational skills that kept the research group on track.

Last I would like to thank my family, which makes my career take flight! : my grandparents **Jung-Hui Chuang** and **Juan-Fen Chuang**, my parents **Yueh-Chung Chuang** and **Tsai-Feng Chen** and my sisters **Han-Ya Chuang**, **Yu-Hsin Chuang** and **Wan-Ru Chuang**. Their persistent love and support have given me the strength to persevere in reaching my educational goals.

Contents

Table Captions

Figure Captions

Chapter 1

Introduction

1.1 Perspectives of Group-III Nitrides and Light-Emitting Diodes (LED)

Starting with the pioneering work of Maruska *et al.* on GaN in the late 1960s and early 1970s with hydride vapor-phase epitaxial growth [1.01, 1.02] and continuing with the subsequent major breakthrough by Amano et al. in the 1980s on two-step growth and *p*-type GaN activation [1.03, 1.04], and then by Nakamura *et al.* in the early to mid 1990s [1.05~1.09], nearly all work on GaN-based materials and devices has been on c-plane (0001)-oriented layers. Due to the inability to fabricate bulk GaN crystal at the time of early GaN pioneering work, an area that still remains a major challenge for nitride research, GaN-based technology, has been developed on foreign substrates. The highest quality GaN has been grown in the (0001) orientation on either (0001)-oriented sapphire or (0001)-oriented 4H-SiC or 6H-SiC.

At the mid-to-late 1990s, Nakamura was making major breakthrough in the GaN-based materials and devices. At the same time, Resta [1.10] and Vanderbilt and Kingsmith [1.11, 1.12] were developing the quantum theory of polarization. In their landmark Vanderbilt and Kingsmith showed that polarization in a sokid is a bulk property and can be determined quantum mechanically with knowledge of the phase of the valence electron wave function. Subsequently, Bernardini *et al.* [1.13] calculated the spontaneous polarization and piezoelectric constants of GaN, AlN, and InN; this work is the standard used currently for these important physical properties in Group-III nitrides.

In 2000, Waltereit *et al.* in Kaus Ploog's group at the Paul Drude Institute in Berlin reported on the first planar nonpolar (10-10) m-plane film on (100)-oriented γ-LiAlO$_2$ substrate [1.14]. In their breakthrough article Waltereit et al. demonstrated the absence of internal electric field in m-plane GaN quantum wells with AlGaN barriers. This work motivated a worldwide research effort in nonpolar and semipolar nitrides.

In 2001~2002, researchers at the UCSB and elsewhere learned that Group-III nitrides growth on *γ*-plane (10-12) sapphire yields *a*-plane {11-20} film with only film orientation; however, previous growth efforts always yielded rough films with faceted three-dimensional morphologies [1.15, 1.16]. Craven *et al.* [1.15] discovered by MOCVD growth and Ng [1.16] realized by molecular beam epitaxy planar a-plane films on *γ*-plane (10-12) sapphire. Until recently, the *γ*-plane was the most common orientation for sapphire substrate, and thus Craven's and Ng's results provided a pathway to large-area low-cost nonpolar films.

In 2005, using defective *m*-plane GaN-based LEDs grown on *m*-plane SiC, Gardner et al. demonstrated another interesting feature of nonpolar structure *i.e.* polarized light emission [1.17]. The potential for engineering In$_{1-x}$Ga$_x$N quantum wells in nonpolar orientations for polarized light emission and detection has been an active area of research.

During 2005~2006, there was a transformation in nonpolar and semipolar GaN research. Researcher at Furukawa Company and at Mitsubishi Chemical Corporation developed several millimeters thick *c*-plane GaN boules by HVPE [1.18]. Subsequently, low defect density nonpolar and semipolar GaN substrate can be prepared by wafering these boules in a suitable orientation. The group at Rohm and at UCSB has produced nonpolar and semipolar LEDs that rival the performance of state-of-art *c*-plane devices. The Rohm and UCSB groups demonstrated the first nonpolar laser diodes and the first AlGaN clad-free laser diodes [1.19].

The promise of nonpolar light emitters has now been realized. In the coming year, we will learn whether nonpolar structures will be the ultimate solution for realizing nitride emitters at many different wavelengths and for a variety of electron devices.

1.2 Specific Properties of Group-III Nitride (GaN) and LED Application

The Group-III nitrides are a remarkable materials system. With direct bandgap from 0.7 eV (InN) through 3.4 eV (GaN) to 6.0 eV (AlN), this materials system has enable deep ultraviolet ($\lambda < 300$nm or photon energy > 4.1 eV based on high Al content $Al_xGa_{1-x}N$ quantum wells), ultraviolet ($\lambda < 400$nm or photon energy > 3.1 eV), blue ($\lambda = 455$nm or photon energy = 2.7 eV based on $In_xGa_{1-x}N$ quantum wells), green ($\lambda = 525$nm or photon energy = 2.4eV) emitters based on $In_xGa_{1-x}N$ quantum wells, and longer wavelength light-emitting diodes. No other materials system offers the range of direct bandgap.

Prior to the development of the nitrides as optoelectronic materials, there were no efficient ultraviolet and blue LEDs. Devices based on Group-III nitrides perform well despite the threading dislocation densities typically in excess of 10^8 cm^{-2} in comparison to conventional III-V materials such as GaAs, where the dislocation densities are typically 10^4 cm^{-2} or less. However, when the nitrides are remarkably robust against oxidation, they are mechanically hard and show no evidence for extended defect motion at standard operation temperatures. GaN-based LEDs feature prominently in colored lighting application, such as green traffic light. When blue LEDs are combined with a yellow-emitting phosphor, white light is produced; thus GaN has become the material that enabled the field of solid-state lighting. Violet GaN-based laser diodes operating at a wavelength of 405nm are already in broad use in high definition optical data storage.

Through the mid-to-late 1990s, there was a broadening realization of the importance of piezoelectricity and polarization in Group-III nitrides [1.20~1.23]. Since the wurtzite structure (hexagonal, space group $P6_3mc$, point group 6mm) is noncentrosymmetric *i.e.* absence of inversion symmetry, it is polar, with spontaneous polarization occurring parallel to the –*c*-axis. Polarization-related effects are a dominant feature in common *c*-axis GaN-based heterostructures and a major differentiating feature of the wurtzite Group-III nitrides from other well-developed semiconductors, such as silicon or gallium arsenide.

For light emitting diodes based on GaN barriers and $In_xGa_{1-x}N$ quantum wells, the fixed charge at the heterostructure cause large electric field normal to the quantum well plane that are in the opposite sense to the polarization-related electric fields in $Al_{1-x}Ga_xN$/GaN system. The difference in spontaneous polarization between $In_xGa_{1-x}N$ and GaN is small, but the $In_xGa_{1-x}N$ layer are coherently strained and large internal electric field result in *c*-plane $In_xGa_{1-x}N$ quantum wells, as shown in figure

1.01, which were produced by self-consistent solutions to the Schrödinger and Poisson equations. In optoelectronic devices such as LEDs, the $In_xGa_{1-x}N$ quantum wells are placed in the depletion region of a *p-n* diode such that injected electrons and holes are captured by the quantum well without recombination in the surrounding materials. These internal polarization-related electric field causes spatial separation of electron and hole wave functions. When the electron and hole wave functions are spatially separated due to the internal polarization-related electric field in the quantum well (quantum-confined Stark effect [QCSE]), the likelihood of a radiative recombination event, which yields the desired photon, is reduced, and thus there is increased likelihood of the injected electrons or holes to nonradiatively recombine and the energy is squandered as heat. Thus, the polarization-related electric fields are seen to reduce efficiency in nitride LEDs and laser diodes.

The challenges associated with polar heterostructure in the nitrides could be avoided entirely by growth in nonpolar orientation (*i.e.* with the *c*-axis of wurtzite structure parallel to any heterojunction). Due to the crystal symmetry, there would be no polarization discontinuity to at the heterointerface. The low index *a*-plane {11-20} and *m*-plane {10-10} are candidate orientations for fabricating nonpolar heterostructures.

The absence of the polarization field effect in nonpolar quantum wells was confirmed by the distinctly short rediative lifetime of *m*-plane AlGaN/GaN quantum wells compared with the *c*-plane radiative lifetime because in the nonpolar quantum wells, the electron an hole wave function have strong overlap, whereas in the *c*-plane quantum wells, the wave functions are spatially separated [1.14]. At the same time, the cathodoluminescence peak energy of *m*-plane quantum well was higher than that of *c*-plane quantum well, which was explained purely by the quantum size effect. After the finding, a similar absence of the QCSE has been reported for *a*-plane AlGaN/GaN quantum wells in *a*-plane GaN [1.16, 1.24].

1.3 Motivation and Organization of the Thesis

Light emitting diodes (LEDs), in particular the Group-III nitride LEDs, have advanced from being low-power indicators to high-power, high-brightness lighting sources. To harness the full potential of it for next-generation solid-state lighting, further increasing in the quantum efficiency is required.

The lighting efficiency of LEDs is determined by mainly two most important factors: the internal quantum efficiency and the light extraction efficiency. The internal quantum efficiency is defined as the ratio of the number of injected electron-hole pairs to that of generated electrons. The light extraction efficiency is defined as the ratio of the number of generated photons to the number extracted from the devices.

As the aforementioned, quantum-confined Stark effect (QCSE) plays an important role in the realm of the Group-III nitride LEDs, especially the InGaN/GaN based LEDs. The nonpolar Group-III nitride materials have approved to overcome the effects of internal electric fields which are caused by the asymmetry of the Group-III nitride crystalline structure. In this thesis, the first part of the research is focusing on the MOCVD growth techniques and the substrate engineering to try to realize a nonpolar, high quality nonpolar *a*-plane GaN on the patterned m-plane sapphire. The results are available in chapter 4. Properties including the substrate engineering method, MOCVD growth modes, and crystalline quality inspection of *a*-plane GaN, the defects distribution and optical properties of the *a*-plane GaN epitaxy are investigated in detail. The experiments in this chapter give great learning of the senses and are a critical guidance to the further experiments.

Still we pay attention to the nonpolar *a*-plane GaN. In chapter 5, a complete planar *a*-plane GaN on patterned *a*-plane GaN tamplates on *γ*-plane sapphire by techniques of trenched epitaxial lateral overgrowth (TELOG) is achieved. And at the same time InGaN/GaN multiple quantum wells (MQWs) are grown on it. As the same in chapter4, the substrate engineering methods, the MOCVD growth modes, the inspections of crystalline qualities including SEM, XRD and TEM images are available. Meanwhile, optical properties including PL and CL of the *a*-plane GaN and the InGaN/GaN MQWs are measured.

So far, by the experiments and results in chapter 4 and 5, the polarity issues of Group-III nitride materials have been overcome. However, the light extraction efficiency is still a problem. Most of the generated photons remain in the LED owing to total internal reflection at its surface, arising because of the large refractive index difference between the semiconductor and air. This causes the ultra-low light extraction efficiency and leads to a low external quantum efficiency.

The fact strongly indicates that some air-voids in the Group-III nitride materials especially the interfaces of different materials would make improvements to the light extraction efficiency at a certain level. Thus we introduce some air-voids into the TELOG *a*-plane GaN and expecte it would help in modifying the light-propagation direction and helps more photons to leave the devices and thus increasing the light-extraction efficiency.

Although there are various competitive methods for improving light extraction efficiency in LEDs, including the introduction of surface roughness, the use of a patterned substrate and chip shaping, here in chapter 6 of the thesis we use KOH-ethylene glycol solution to enlarge the initial voids in the *a*-plane GaN which was formed during the MOCVD growth periods by TELOG techniques. The etching mechanisms under different etching condition are clarified and the etching rates have been determined. What's more, the effect of these etched air-voids on the enhancement of light extraction efficiency is measured. We successfully achieve the redistribution of the light emission and gain a significant increase in the emission intensity at certain ranges of angle.

Brief conclusions and future works are available in chapter 7, which will fulfill the related experiments and give a further potential application of the results in this thesis.

1.4 References

[1.01]H. P. Maruska, J. J. Tietjen, *Appl. Phys. Lett.* **15**, 327 (1969)

[1.02]H. P. Maruska, D. A. Stevenson, J. I. Pankov, *Phys. Lett.* **22**, 303 (1973)

[1.03]H. Amano, N. Sawaki, I. Akasaki, Y. Toyoda, *Phys. Lett.* **48**, 333 (1986)

[1.04]H. Amano, M. Kito, K.I. Hiramatsu, I. Akasaki, *Jpn. J. Phys. Lett.* **28**, L2112 (1989)

[1.05]S. Nakamura, *Jpn. J. Phys. Lett.* **30**, L1705 (1991)

[1.06]S. Nakamura, T. Mukai, M. Senoh, *Jpn. J. Phys. Lett.* **30**, L1998 (1991)

[1.07]S. Nakamura, N.Iwasa, T. Mukai, M. Senoh, *Jpn. J. Phys. Lett.* **31**, L1258 (1992)

[1.08]S. Nakamura, T. Mukai, M. Senoh, *Appl. Phys. Lett.* **64**, 1687 (1994)

[1.09]S. Nakamura, M. Senoh, S. Nagahama, N.Iwasa, T. Yamada, T. Matsushita, H. KIyoku, Y.Sugimoto, *Jpn. J. Phys. Lett.* **35**, L74 (1996)

[1.10]R. Resta, *Ferroelectrics* **136**, 51 (1992)

[1.11]R. D. Kingsmith, D. Vanderbilt, *Phys. Rev. B* **47**, 1651 (1993)

[1.12]D. Vanderbilt, R. D. Kingsmith, *Phys. Rev. B* **48**, 4442 (1993)

[1.13]F. Bernardini, F. Fiorentini, D. Vanderbilt, *Phys. Rev. B* **56**, 10024 (1997)

[1.14]P. Waltereit, O. Brandt, A. Trampert, H. T. Grahn, J. Meeiger, M. Ramsteiner, M. Reiche, K. H. Ploog, *Nature* **406**, 865 (2000)

[1.15]M. D. Craven, S. H. Lim, F. Wu, J. S. Speck, S. P. DemBaars, *Appl. Phys. Lett.* **81**, 469 (2002)

[1.16]H. M. Ng, *Appl. Phys. Lett.* **80**, 4369 (2002)

[1.17]N. F. Gardner, J. C. Kim, J. J. Wierer, Y. C. Shen, M. R. Krames, *Appl. Phys. Lett.* **86**, 111101 (2002)

[1.18]M. Funato, M. Ueda, Y. Kawakami, Y. Narukawa, T. Kosugi, M. Takahashi, T. Mukai, *Jpn. J. Phys. Lett.* **45**, L659 (2006)

[1.19]D. F. Feezell, M. C. Schmidt, R. M. Farrell, K. C. Kim, M. Saito, K. Fujito, D. A. Cohen, J. S. Speck, S. P. DemBaars, S. Nakamura, *Jpn. J. Phys. Lett.* **46**, L284 (2007)

[1.20]A. Byhovski, B. Gelmont, M. Shur, *J. Appl. Phys.* **74**, 6734 (1993)

[1.21]S. Chichibu, T. Azuhata, T. Sato, S. Nakamura, *Appl. Phys. Lett.* **69**, 4188 (1996)

[1.22]T. Takeuchi, S. Sato, M. Katsuragawa, M. Komori, H. Takeuchi, H. Amano,

I. Akasaki, *Jpn. J. Phys. Lett.* **36**, L382 (1997)

[1.23]J. S. Im, H. Kollmer, J. Off, A. Sohmer, F. Scholz, A. Hangleiter, *Phys. Rev. B* **57**, R9435 (1998)

[1.24]T. Koida, S.F. Chichibu, T. Sato, M. D. Craven, B. A. Haskell, J. S. Speck, S. P. DemBaars, S. Nakamura, *Appl. Phys. Lett.* **84**, 3768 (2004)

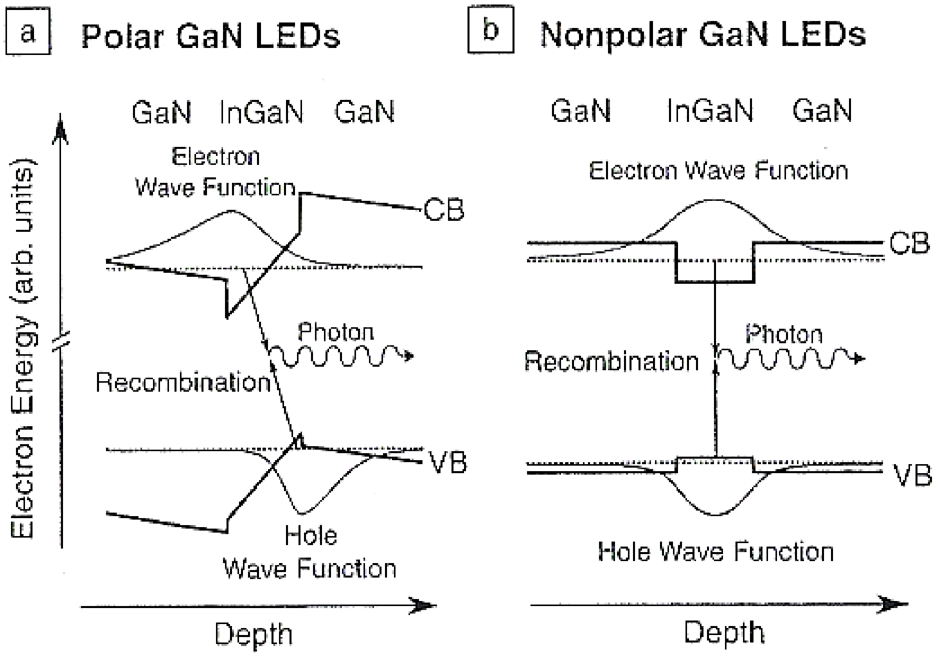

Figure 1.01. Self-consistent solutions to the Schrödinger-Poisson solutions for the band profile for GaN/ $In_xGa_{1-x}N$/GaN quantum well in polar and nonpolar orientation.

Chapter 2

Experimental Apparatus

2.1 Sapphire Substrate

The crystal lattice of crystalline sapphire is formed by Al^{3+} and O^{2-} ions. If the O^{2-} anions are depicted as balls, the crystal lattice takes the form of their closest hexagonal packing in figure 2.01. The Al^{3+} cations are located in a crystalline field that has no symmetry center (due to crystal lattice distortions). These cations lie in the octahedral hollows between the closely packed O^{2-} ions, filling two thirds of these hollows. The octahedron hollow is surrounded by six balls. If the radius of each is taken as a unit, then the hollow contains a ball with a relative radius of 0.41. Due to the ratio of the ionic radii of O^{2-} and Al^{3+} (equal to 1.40 and 0.57 Å, respectively), the cations are located within the hollows of the anion packing. They slightly distort the lattice, but do not fall outside the stability limits of the octahedron position.

Lattice parameters, or hexagonal lattice constants of crystalline sapphire are $a = b$ and c, and the interplanar distances are given by the equation 2.01

$$\mathrm{d}_{hkl}=1 / [(4/3\alpha^2)(h^2+k^2+hk) + (1+1/c^2)\mathrm{l}^2]^{1/2} \tag{2.01}$$

The values of the interplanar distances are presented in Table 2.01. The lattice parameters increase with increasing temperature. At 295.65K a=4.759213Å, c=12.991586 Å [2.01], and the ratio c/a=2.729776 far exceeds that of a crystal with ideal hexagonal packing $(8/3)^{0.5}$=1.633. Precise measurements of the temperature dependence of the lattice parameters within 4.5~374K temperature range in figure 2.02 were carried out using ^{57}Fe Mössbauer radiation [2.02].

Cleavage in sapphire arises at the intersections of a pair of parallel nets formed by anions. Nets with like charges reduce attractive forces. The larger the distance between the nets, the more vividly the cleavage manifests itself. In a perfect crystal the plane of chipping must pass between these nets. In the basal plane with interchanging O–Al–Al–O–Al–O layers there are no conditions for cleavage, whereas in the plane (10-11) with interchanging O–O–Al–O–Al–O–O—O–Al–O–Al–O layers the bonds between the layers O–O located at a distance of 1.06 Å are weakened.

Sapphire does not have such a vivid cleavage as diamond and other crystals. For a long period of time, sapphire was considered to exhibit no cleavage at all. Theoretically, it has nine cleavage planes. Six planes are parallel to the facets {11-20}and {10-11}, and to the *c*-axis; three planes are parallel to the facets {10-11} and inclined to the *c*-axis at an angle of 33°, the normal vectors to them make an angle of 57° with the *C*-axis. Crystals with a small quantity of dislocations and which do not contain blocks may have perfect cleavage in the plane of the morphological rhombohedron {10-11}. However, when block-containing and stressed crystals grown by the Verneuil method are chipped along the prismatic planes, mirror chips with steps of several atomic parameters are often observed as in figure 2.03. To achieve more desirable chipping of these crystals, the direction of the *c*-axis is set at an angle 57° to the crystal growth axis at the location of the prism and rhombohedron planes, as shown in figure 2.03 [2.03].

The energy required for destruction along the plane {10-11} is 6 J/m^2, whereas for the basal plane the corresponding value is more than 40 J/m^2 [2.04]. Shown by the estimation of the surface energy of the planes, considered to be defined by the quantity of free bonds per unit of surface, the minimum quantity of such bonds corresponds to the plane (10-11) [2.05].

The shape of natural crystals usually has the following facets (denoted by the most often used literal symbols): c(0001), a{11-20}, γ{10-11}, n{22-43}, m{10-10}, s{02-21}, s{22-43}, R{01-12}, p{11-23}(figure 2.04) and others. The symbols of crystallographic planes in the morphological and the structural classification systems, the stereographic projections of sapphire for some planes are given in Tables 2.02 and 2.03. Besides the main crystallographic planes, tens of others exist which have their own symbols. The main forms with their spherical coordinates are presented in Table 2.04. The planes that are most often encountered in the practice of sapphire usage are shown in Fig. 2.05. The plane (1012) is inclined to (0001) plane at an angle of 57°36’, while with the plane (1120) it makes an angle of 32°24’. The angles between the normals to the facets of sapphire are given in Table 2.05.

2.2 Metalorganic Chemical Vapor Deposition (MOCVD)

Metalorganic Chemical Vapor Deposition (MOCVD) is the most common epitaxial technique used in both industry and research. It has the benefit of high growth rate on large area wafers. One problem with MOCVD is that it requires complicated and sometimes vary hazardous gases in order to produce the epitaxial layer. Compound semiconductors are grown from the surface reaction of organic compounds or metalorganics and hydrides containing the required species. In growing

GaN hydride mixture containing ammonia and trimethyl-gallium (TMGa), highly diluted by hydrogen or nitrogen, is led into the reactor separately. Figure 2.06 shows a schematic drawing of the MOCVD subsystem. The vapor pressure of the MO source is a function of temperature. By placing the MO bottle in a bath containing a mixture of water and glycol, the vapor pressure can be controlled over a wide range of temperature. The carrier gas is “bubbled” through the MO liquid and transport into the line. The amount of vapor transported into the line depends on the flow rate of the carrier gas (Φ_c), the pressure in the bottle (P_b) and the vapor pressure P_{vap} of the MO (Φ_{MO}). When growing epitaxial films in the reactor, it is of great importance to know how much source material is introduced. Since the volume and the temperature of the source bottle is constant, the perfect gas law can be used to determine the flow rate of MO (Φ_{MO}). During a time interval Δt, $\Phi_{MO} \cdot \Delta t \, \alpha$ n moles of source material is defined from the bottle. According to the perfect gas law

$$\frac{\phi}{P_b} = constant \rightarrow \frac{\phi_{MO}}{P_{vap}} = \frac{\phi_c}{P_s} \qquad (2.02)$$

where P_c is the partial pressure of the carrier gas in the bottle. In the gas panel configuration shown in figure 2.06, the pressure in the bottle is controlled from the following line. The partial pressure of the source gas can be expressed as $P_c = P_b - P_{vap}$. Inserting into equation 2.02 the flow rate of the MO (in cm^3/min) can be evaluated.

The precursor molecules NH3 and TMGa are fed in separately into the reactor chamber. In the reactor reactions take place both on the wafer and before the molecules reach the wafer. Formation of the epitaxial layer occurs by the reaction

$$Ga(CH_3)_3 + NH_3 \rightarrow GaN + CH_4 \qquad (2.03)$$

Figure 2.07 illustrate the growth process with impinging precursors and rest products. Due to the low cracking efficiency of ammonia and adatom mobility the growth of GaN is carried out at very high temperature around 1000°C ~1100°C to high crystalline quality. Many of the difficulties involving the growth of GaN are due to the high volatility of nitrogen. The pressure of nitrogen in the vapor must not be below a certain value to produce the solid without other phases. If the pressure is too low, a Ga liquid phase is formed resulting in droplet formation on the surface of crystal ($GaN + 3/2H_2 \rightarrow Ga + NH_3$). An alternative precursor to NH3 for atomic nitrogen is dimethyl-hydrazine [2.06]. It has successively been used for growth of GaN [2.07]. Dimethyl-hydrazine has a relatively low decomposition temperature compared to NH3. At 420°C it decompose up to 50% [2.08], while NH3 only 15% at 950°C [2.09].

One thing to be mentioned is that MOCVD is a diffusion controlled process, as the region II in figure 2.08. This regime appears at moderate temperatures. Compared with the chemical reaction regime the mass transport rate of the reactant gaseous species is much lower than that of the chemical reaction, *i.e.* $h_G \ll k_S$. The coating growth is limited by the mass transport from the bulk gas to the substrate surface. In this case a steep concentration gradient within the boundary layer is generated and the reactant gaseous species are nearly consumed on the substrate surface.

In this regime, the temperature dependence of the growth rate becomes mild, which is attributed to the gaseous species diffusivity. The growth rate of the coating increases linearly with the partial pressure increasing of the reactant gaseous species (p_{react}), which is confirmed through experimental work as shown in figure 2.08. The growth rate is inversely proportional to the total pressure in the system. The mass transport rate can be considerably enhanced through a decrease in the total pressure.

This is the main reason that most CVD processes are operated at reduced pressures. An increase in the gas velocity in the bulk is useful to reduce the thickness of the boundary layer and, hence, results in a more rapid growth rate of coatings.

For the growth of monolithic materials the high growth rate is much more important than the thickness uniformity from an economical view. The MOCVD processes are often performed in the mass transport regime. The higher processing temperatures are used for thermal gradient CVI and forced CVI processes in which fast growth rates are needed to ensure the rapid densification of the composites.

2.3 Inductively Coupled Plasma Reactive Ion Etching (ICP-RIE)

It has been demonstrated that conventional RIE is perfectly capable of etching sub-100 nm structures. The only limitation is its relatively low etch rate, which is normally less than 200 nm min^{-1} for Si. The etching rate in RIE directly depends on plasma density. For the conventional RIE system as shown in Figure 2.09, plasma density increases with increase of RF power. However, increasing RF power will also increase the self-biasing voltage on the cathode where the etching sample is situated. The consequence is the increase of ion bombardment energy, hence deterioration of etching selectivity. This becomes a particularly serious problem in sub-100 nm RIE, because the masking layer is always thin to enable photon or e-beam patterning of polymer resist at sub-100 nm feature dimension.

Inductively coupled plasma (ICP) system has cleverly solved the problem. In an ICP source, the plasma generation is separated from etching chamber, as shown in Figure 2.10. Radio frequency power is coupled into plasma chamber by an induction coil from outside. The sample stage is connected to a second RF power source as an auxiliary RF source to enhance the production of plasma. Electromagnetic field generated by inductive coupling coil can sustain electron cycling movement in plasma for a long period, which has greatly increased ionization probability while keeping the pressure low in the etching chamber. As the sample stage has an independent input of RF power, the self-biasing voltage can be independently controlled. Therefore, an ICP system can produce very high plasma density ($>5\times10^{11}$ cm^{-3}) compared to conventional RIE (10^{8}~10^{10} cm^{-3}), as well as maintain low ion bombardment energy. The conflict between high plasma density and high etch selectivity encountered in conventional RIE systems has been resolved. With such high plasma density and high etching selectivity, high etching rate and deep RIE (DRIE) become possible.

ICP-RIE has been widely used for etching other materials, especially the III-nitride semiconductors. The ICP with high plasma density offers much higher etch rate and selectivity than it is possible by conventional RIE. For example, GaN or sapphire is known to be difficult to etch. With a conventional RIE, the etch rate is less than 5nm min^{-1}. Using an ICP-RIE the etch rate is nearly 10 times enhanced. Inductively coupled plasma systems are widely used to etch III–V semiconductor materials which are of great importance in high frequency and optoelectronic applications currently.

2.4 Potassium Hydroxide (KOH)-Ethylene Glycol Solution

Potassium hydroxide is an inorganic compound with the formula KOH. Along with sodium hydroxide (NaOH), this colorless solid is a prototypical "strong base". It has many industrial and niche applications. Most applications exploit its reactivity toward acids and its corrosive and etching nature to many materials including the GaN semiconductors. Potassium hydroxide can be found in pure form by reacting sodium hydroxide with impure potassium. Potassium hydroxide is usually sold as translucent pellets, which will become tacky in air because KOH is hygroscopic. Consequently, KOH typically contains varying amounts of water (as well as carbonates). Its dissolution in water is strongly exothermic, meaning the process gives off significant heat. Concentrated aqueous solutions are sometimes called potassium lyes. Even at high temperatures, solid KOH does not dehydrate readily [2.10].

Approximately 121g of KOH will dissolve in 100 ml of water at room temperature (compared with 100 g of NaOH in the same volume). Lower alcohols such as methanol, ethanol, ethylene glycol and propanol are also excellent solvents. The solubility in ethanol is about 40 g KOH/100 ml.

In the experiments for the thesis, the solvent chosen for KOH is ethylene glycol. Ethylene glycol, with molecular formula $C_2H_6O_2$, density 1.1132g/cm^3, melting point 240K (-12.9°C) and most important of all, boiling point 470K (197.3°C), is perfectly suitable to make the KOH- ethylene glycol solution to the concentration of >30% and heat up to >140°C. At the same time, the high boiling temperature protects the solution from evaporation seriously at high temperature and maintains the concentration of KOH at a relatively stable level. The properties of viscosity of ethylene glycol is 1.61×10^{-2}N · s/m^2, which do not hinder the solution from flowing into the specifically designed structure in the experiment.

One more thing to note is that the ethylene glycol enhances the etching rate of GaN, excepting the higher boiling point, by the higher solubility of Ga_2O_3 in it. The faster the product during GaN etching process is dissolved, the faster the etching rate performed. The easily-prepared, low-temperature KOH-ethylene glycol solution provides a relatively higher etching rate to GaN than that of extremely high-temperature molten KOH.

2.5 Scanning Electron Microscopy (SEM)

It is worthwhile to understand the technique and type of instrument of SEM. Very simply; the SEM scans a sample with a beam of electrons that interact with the sample. Some of those electrons and other electrons generated during this process escape from the sample and reach a detector. The number of electrons that reach the detector at each point on the sample depends on the topology of the sample and the atomic weight of the atoms at the surface, and these variations in signal strength lead to image formation.

A SEM column consists of an electron gun, one or two condenser lenses, an objective aperture, and an objective lens [2.11]. The electron gun produces a source of electrons and accelerates the electrons to energy of 1~30 keV. This occurs in a vacuum environment ranging from 10^{-4} to 10^{-10} Torr. The electron lenses in the column are used to demagnify the image of the gun crossover and focus a final spot on the specimen on the order of 1 nm~1 μm with a beam current in the range of

1pA~1μA. The condenser lens controls the amount of demagnification and the probe forming or objective lens focuses the final probe on the specimen. A schematic of a typical SEM is shown in Figure 2.11.

The lens and aperture system in the column provide control of the beam through manipulation of the probe diameter, probe current, and convergence angle. These three parameters can be controlled and used to achieve high depth-of-field, high-resolution, or high beam current for x-ray microanalysis. A small convergence angle is needed for high depth-of-field imaging and can be obtained with a small objective aperture and a long working distance. High resolution imaging requires a small probe size which can be obtained with a strong condenser lens, an objective aperture, and a short working distance. Finally, x-ray microanalysis may require higher beam currents which can be obtained by weakening the condenser lens and removing the objective aperture.

The interactions between the electron beam and the specimen in a SEM are the source for a wide variety of signals that can be collected and used to characterize the sample as in figure 2.12. The electron beam-specimen interactions are a result of elastic and inelastic scattering processes that occur simultaneously within the sample. The region in which the electrons interact with the specimen is called the interaction volume. The interaction volume can extend from a few nanometers to a few microns below the surface depending on the beam and sample parameters. Elastic scattering events produce large angular changes in the trajectory of the beam electrons inside the sample, but result in little or no change to the energy of the electron, thus giving rise to the overall shape of the interaction volume. Elastic scattering primarily gives rise to backscattered electrons (BSE). Inelastic scattering events result in the transfer of energy from the beam electrons to the tightly bound inner-shell electrons and loosely bound outer-shell electrons of the atoms in the specimen with very little angular change in the trajectory of the beam electron. During a single inelastic scattering event the beam electron can transfer an amount of energy ranging from less than 1 eV to the full energy carried by the beam electron. Inelastic scattering limits the range of the electrons within the specimen by eventually reducing the electron energy to zero. Inelastic scattering gives rise to phonons (lattice vibrations), plasmons (electron oscillations), auger electrons, characteristic x-rays, continuum x-rays, secondary electrons (SE), and electron hole pair (EHP) generation. EHP generation in a material with a bandgap is the basis for the EBIC and CL signals.

The incident electrons interact with a certain volume of the sample called the interaction volume. There are numerous analytical expressions that have been used to model the size and shape of this interaction volume, which will not be covered here. The interaction volume depends on a number of factors, including the beam energy, the atomic number of the specimen, and the angle the incoming probe beam makes with the sample surface. The number of backscattered and secondary electrons (BSE and SE) produced will depend on these parameters and others such as the topology of the sample, and will result in the image contrast observed. Several detection systems are depicted in figure 2.13 and 2.14.

2.6 Scanning Transmission Electron Microscopy (STEM)

High-resolution STEM capabilities are needed in order to overcome the SEM resolution limits created by the interaction volume in bulk samples. Originally, STEM capabilities were achieved by using convergent-beam TEM in spot mode. In the traditional TEM mode, two condenser lenses are adjusted to illuminate the specimen with a nearly parallel beam of electrons. The transmitted electrons are then focused by the objective lens to form a real image. Convergent-beam TEM in spot mode uses a series of condenser lenses to demagnify the original gun crossover to a spot on the specimen [2.12]. Scan coils can then be used to move the spot across the specimen. A TEM with scanning capabilities is often referred to as a STEM in the literature [2.13].

In a dedicated STEM, the optical design is more closely related to a SEM than a TEM. A source of electrons is produced by an electron gun and accelerated to an energy of approximately 200~400keV. In a cold Field Emission STEM (FESTEM), the initial crossover is on the order of 5.0 nm. The vacuum is capable of reaching 1.0×10^{-8} Pascal in the electron gun and approximately 3.0×10^{-5} Pascal in the specimen chamber. The optics system focuses the electron beam to a final spot on the sample on the order of 0.5 nm with a beam current of approximately 1 nA [2.12]. While bulk specimens can be analyzed in a SEM, a thin sample on the order of hundreds of nanometers is used for STEM analysis. The high energy electron beam and thin sample decrease the size of the interaction volume and improve the resolution. As discussed in Section 2.5, several signals including SE, BSE, x-rays, photons, and EHPs are produced from the interaction volume that is created within the thin specimen and can be detected and used for imaging. In addition, the transmitted electrons can be detected with a high-angle annular dark field (HAADF) detector or a bright field (BF) detector. The HAADF detector is an annular detector placed concentrically about the post-specimen optical axis. The HAADF detector detects transmitted electrons that have been scattered through high angles. The acceptance angle of the HAADF detector is typically between 50mrad~200mrad, but can often be controlled with a projector lens. HAADF images are often called “Z-contrast” images because the cross section for Rutherford elastic scattering is proportional to Z^2 [2.12, 2.13]. Therefore, high-Z regions of a specimen would scatter more electrons and have a higher intensity than low-Z regions [2.12, 2.13]. The BF detector is an axial detector that is usually placed after the HAADF detector and detects transmitted electrons that have undergone low angles of scatter.

2.7 Transmission Electron Microscopy (TEM)

The transmission electron microscopy (TEM) is used to characterize the microstructure of materials with very high spatial resolution. Information about the morphology, crystal structure and defects, crystal phases and composition, and magnetic microstructure can be obtained by a combination of electro-optical imaging (2.5Å point resolution), electron diffraction, and small probe capabilities. The trade-off for this diverse range of structural information and high resolution is the challenge of producing very thin samples for electron transmission.

The TEM uses a high energy electron beam transmitted through a very thin sample to image and analyze the microstructure of materials with atomic scale resolution. The electrons are focused with electromagnetic lenses and the image is observed on a fluorescent screen, or recorded on film or digital camera. The electrons are accelerated at several hundred kV, giving wavelengths much smaller than that of light: 200kV electrons have a wavelength of 0.025Å. Unfortunately, whereas the resolution of the optical microscope is limited by the wavelength of light, that of the electron microscope is limited by aberrations inherent in electromagnetic lenses, to about 1~2 Å.

Because even for very thin samples one is looking through many atoms, one does not usually see individual atoms. Rather the high resolution imaging mode of the microscope images the crystal lattice of a material as an interference pattern between the transmitted and diffracted beams. This allows one to observe planar and line defects, grain boundaries, interfaces, *etc.* with atomic scale resolution. The bright-field/dark-field imaging modes of the microscope, which operate at intermediate magnification, combined with electron diffraction, are also invaluable for giving information about the morphology, crystal phases, and defects in a material. Finally the microscope is equipped with a special imaging lens allowing for the observation of micro-magnetic domain structures in a field-free environment.

The TEM is also capable of forming a focused electron probe, as small as 20Å, which can be positioned on very fine features in the sample for micro-diffraction information or analysis of x-rays for compositional information. The latter is the same signal as that used for SEM composition analysis, where the resolution is on the order of one micron due to beam spreading in the bulk sample. The spatial resolution for this compositional analysis in TEM is much higher, on the order of the probe size, because the sample is so thin. Conversely the signal is much smaller and therefore less quantitative. The high brightness field-emission gun improves the sensitivity and resolution of x-ray compositional analysis over that available with more traditional thermionic sources.

Sample preparation for TEM generally requires more time and experience than for most other characterization techniques. A TEM specimen must be approximately 1000Å or less in thickness in the area of interest. The entire specimen must fit into a

3mm diameter cup and be less than about 100 μm in thickness. A thin, disc shaped sample with a hole in the middle, the edges of the hole being thin enough for TEM viewing, is typical. The initial disk is usually formed by cutting and grinding from bulk or thin film/substrate material, and the final thinning done by ion milling. Other specimen preparation possibilities include direct deposition onto a TEM-thin substrate (Si_3N_4, carbon); direct dispersion of powders on such a substrate; grinding and polishing using special devices (t-tool, tripod); chemical etching and electro-polishing; lithographic patterning of walls and pillars for cross-section viewing; and focused ion beam (FIB) sectioning for site specific samples.

Artifacts are common in TEM samples, due both to the thinning process and to changing the form of the original material. For example surface oxide films may be introduced during ion milling and the strain state of a thin film may change if the substrate is removed. Most artifacts can either be minimized by appropriate preparation techniques or be systematically identified and separated from real information

2.8 Photoluminescence Spectroscopy (PL) and Cathodoluminescence Spectroscopy (CL)

When a solid is supplied with a certain type of energy it may emit photons, or undergo a process called luminescence. The luminescence process can be categorized according to the excitation source. Photoluminescence (PL) is due to photon excitation, chemiluminescence is due to energy supplied by a chemical reaction, thermoluminescence is due to energy supplied by heating, electroluminescence is due to excitation by application of an electric field, and cathodoluminescence (CL) is due to excitation by an electron source. The mechanisms leading to the emission of light in a solid are similar for the different types of excitation sources described above and can provide complimentary information [2.14, 2.15].

Photoluminescence (PL) depends on the nature of the optical excitation. The excitation energy selects the initial photoexcited state and governs the penetration depth of the incident light. The emission signal depends on the density of photoexcited electrons, and the intensity of the incident beam can be adjusted to control this parameter. When the type or quality of material under investigation varies spatially, the PL signal will change with excitation position. In addition, pulsed optical excitation provides a powerful means for studying transient phenomena. Short laser pulses produce virtually instantaneous excited populations, after which the PL signal can be monitored to determine recombination rates.

PL is simple, versatile, and nondestructive. The instrumentation that is required for ordinary PL work is modest: an optical source and a spectrophotometer. A typical PL set-up is shown in Figure 2.15. Because the measurement does not rely on electrical excitation or detection, sample preparation is minimal. This feature makes PL particularly attractive for material systems having poor conductivity or undeveloped contact technology. Measuring the continuous wave PL intensity and spectrum is quick and straightforward. Instrumentation for time-resolved detection, such as single photon counting, can be expensive and complex. Even so, PL is one of the only techniques available for studying fast transient behavior in materials.

The advantages of PL analysis derive from the simplicity of optical measurements and the power to probe fundamental electronic properties. The chief drawback of PL analysis also follows from the reliance on optical techniques: the sample under investigation must emit light. Indirect-bandgap semiconductors, where the conduction band minimum is separated from the valence band maximum in momentum space, have inherently low PL efficiency. Nonradiative recombination tends to dominate the relaxation of excited populations in these materials. This problem can be augmented by poor surface quality, where rapid nonradiative events may occur. Nevertheless, once a PL signal is detected, it can be used to characterize both radiative and nonradiative mechanisms.

The choice of excitation is critical in PL measurement. The excitation energy and intensity will have profound effects on the PL signal. Although the excitation conditions must be considered carefully, the strength of the PL technique relies heavily on the flexibility that these adjustable parameters provide. Because the absorption of most materials depends on energy, the penetration depth of the incident light will depend on the excitation wavelength. Hence, different excitation energies probe different regions of the sample. The excitation energy also selects the initial excited state in the experiment. Because lasers are monochromatic, intense, and readily focused, they are the instruments of choice for photoluminescence excitation. A relatively inexpensive He-Cd or diode laser will often satisfy the basic requirement of light exceeding the bandgap energy. In more demanding experiments, the laser is chosen carefully to probe a particular depth or to excite a particular species.

Cathodoluminescence (CL) is a SEM-based technique that can be used for the characterization of semiconductor materials and devices. SEM-based and CL can provide information on the concentration and distribution of luminescent centers, distribution and density of electrically active defects, and electrical properties including minority carrier diffusion lengths and lifetimes. CL is the emission of light as the result of electron or “cathode-ray” bombardment. The CL phenomenon was first reported in the middle of the 19th century during experiments on electrical discharges in evacuated glass tubes. Luminescence was observed when cathode rays struck the glass tubes [2.14, 2.15]. The observation of luminescence due to cathode ray bombardment eventually led the J.J. Thomson to the discovery of electron in 1897. Now, CL is widely used in cathode-ray tubebased instruments such as oscilloscopes, televisions, and electron microscope fluorescent screens [2.14, 2.15].

The CL signal is generated by detecting photons, in the ultraviolet to infrared range, that are emitted as a result of electronic transitions between the conduction band and valence band, between levels due to impurities and defects in the fundamental gap, or between impurity and defect levels and the valence band. The transition energies and probabilities can be affected by external perturbations, such as stress and electric fields. CL analysis performed in an electron microscope can be divided into spectroscopy and microscopy.

In CL microscopy, luminescence images or maps of areas of interest are obtained by a scanning or parallel beam. In panchromatic CL imaging the combined intensity of all CL wavelengths within the response of the detector are used to create the image. In monochromatic CL imaging, the light is coupled into a monochromator and CL images can be created from a selected wavelength bandpass [2.14, 2.15].

In direct band gap semiconductor materials, the minimum of the conduction band and the maximum of the valence band occur at the same momentum value in an energy versus momentum plot. Momentum is conserved in direct band gap transitions and the transitions appear vertical on energy versus momentum plots. In these materials, the most likely radiative transitions are between the filled states of the conduction band minimum and the empty states of the valence band maximum. If the material is an indirect band-gap material, the maximum of the valence band and minimum of the conduction band do not occur at the same momentum value, and therefore phonon participation is required to conserve momentum. The recombination of electrons and holes results in the simultaneous emission of a photon and a phonon. Since the probability of this process is lower than direct transitions, intrinsic emission is relatively weak compared to extrinsic luminescence in an indirect band gap material. A simplified set of radiative transitions that lead to luminescence emission in semiconductors containing impurities is shown in Figure 2.16 and a description of each process follows.

Process 1 produces intrinsic luminescence due to direct recombination between an electron in the conduction band and a hole in the valence band and results in the emission of a photon with energy close to that of the band gap. The recombination may occur from states close to the corresponding band edges, but the thermal distribution of carriers typically leads to a Gaussian shaped spectrum with the peak corresponding to the transition with the maximum electron and hole concentrations [2.14, 2.15].

Process 2 is excition decay that is typically observable at lower temperatures. An excition is a bound electron-hole pair and excitionic states exist just below the conduction band. In most III-V compounds, recombination emission of the excitonic state produces photons of energies approximately equal to the band gap of the semiconductor; therefore this process can also be considered an intrinsic process. The intrinsic luminescence band is often referred to as the near-band-gap band because excitons and shallow recombination centers may contribute to the emission at room temperature [2.14, 2.15].

Process 3, 4, and 5 correspond to transitions that start or finish on localized states of impurities within the band gap, such as donors or acceptors. These transitions produce extrinsic luminescence. Transitions between deep donor and deep acceptor levels can lead to emission with photon energies significantly below the band gap. Shallow donor or acceptor levels can be very close to the conduction band and valence bands. For example, silicon is a shallow donor in gallium nitride located approximately 20 meV below the conduction band [2.17]. Transitions that occur between a shallow donor and acceptor states or between donor and acceptor states and the conduction band or valence bands may be difficult to distinguish from intrinsic luminescence. In these cases, CL measurements can be performed at cryogenic temperatures using liquid nitrogen or liquid helium as a cryogen. CL spectra can be sharpened into lines and series of lines corresponding to transitions between well defined energy levels due to a reduction in the thermal excitation of carriers. There is also an increase in the CL intensity as the temperature is lowered because radiative recombination becomes more favored as compared to the competing non-radiative recombination. An additional advantage of performing CL at cryogenic temperatures is the reduction of electron bombardment damage [2.14, 2.15].

2.9 X-ray Diffraction (XRD)

X-rays are electromagnetic radiation with typical photon energies in the range of 100 eV~100 keV. For diffraction applications, only short wavelength x-rays in the range of a few Å to 0.1 Å (1 keV~120 keV) are used. Because the wavelength of x-rays is comparable to the size of atoms, they are ideally suited for probing the structural arrangement of atoms and molecules in a wide range of materials. The energetic x-rays can penetrate deep into the materials and provide information about the bulk structure.

X-rays are produced generally by either x-ray tubes or synchrotron radiation. In an X-ray tube, which is the primary X-ray source used in laboratory X-ray instruments, x-rays are generated when a focused electron beam accelerated across a high voltage field bombards a stationary or rotating solid target. As electrons collide with atoms in the target and slow down, a continuous spectrum of X-rays are emitted, which are termed Bremsstrahlung radiation. The high energy electrons also eject inner shell electrons in atoms through the ionization process. When a free electron fills the shell, a x-ray photon with energy characteristic of the target material is emitted. Common targets used in x-ray tubes include Cu and Mo, which emits 8 keV and 14 keV X-rays with corresponding wavelengths of 1.54 Å and 0.8 Å, respectively.

X-rays primarily interact with electrons in atoms. When x-ray photons collide with electrons, some photons from the incident beam will be deflected away from the direction where they originally travel, much like billiard balls bouncing off one another. If the wavelength of these scattered x-rays did not change, the process is called elastic scattering (Thompson Scattering) in that only momentum has been transferred in the scattering process. These are the x-rays that measured in diffraction experiments, as the scattered x-rays carry information about the electron distribution in materials. On the other hand, in the inelastic scattering process (Compton Scattering), x-rays transfer some of their energy to the electrons and the scattered x-rays will have different wavelength than the incident x-rays.

Diffracted waves from different atoms can interfere with each other and the resultant intensity distribution is strongly modulated by this interaction. If the atoms are arranged in a periodic fashion, as in crystals, the diffracted waves will consist of sharp interference maxima with the same symmetry as in the distribution of atoms. Measuring the diffraction pattern therefore allows us to deduce the distribution of atoms in a material.

The peaks in X-ray diffraction pattern are directly related to the atomic distances. Consider an incident x-ray beam interacting with the atoms arranged in a periodic manner. For a given set of lattice planes with an inter-plane distance of d, the condition for a diffraction (peak) to occur can be simply written as $2d \cdot \sin\theta = n\lambda$ which is known as the Bragg's law. The Bragg's Law is one of most important laws used for interpreting x-ray diffraction data.

It is important to point out that although we have used atoms as scattering points in this example, Bragg's Law applies to scattering centers consisting of any periodic distribution of electron density. In other words, the law holds true if the atoms are replaced by molecules or collections of molecules, such as colloids, polymers, proteins and virus particles.

X-ray crystallography is a standard technique for solving crystal structures. Its basic theory was developed soon after X-rays were first discovered more than a century ago. However, over the years it has gone through continual development in data collection instrumentation and data reduction methods. In recent years, the advent of synchrotron radiation sources, area detector based data collection instruments, and high speed computers has dramatically enhanced the efficiency of crystallographic structural determination. Today X-ray crystallography is widely used in materials and biological research. Structures of very large biological machinery have been solved using this method.

2.10 References

[2.01]Shvid'ko Yu.V., Lucht M., Gerdau E. et al. *J. Synchr. Rad.* **9**, 2002, 17

[2.02]Lucht M., Lerche M., Wille H.C. et al. *J. Appl. Cryst.* **36**, 2003, 1075

[2.03]Gumilevskiy A.A. *Watches and Watch Mechanisms*. **1** (131), 1962, 26

[2.04]Wiederhorn S.M. *J. Am. Ceram. Soc.* **59**, 1969, 485

[2.05]Hartman P., *Proceedings of Mineralogical Society. Leningrad: USSR Academy of Sciences*. **91** (6), 1962, 672

[2.06]C. Sartel, S. Gautier, S. Ould Saad Hamady, N. Maloufi, J. Martin, A. Sirenko, and A. Ougazzaden, *Superlattices Microstruct.,* **40**, 2006, 476.

[2.07]Hitoshi Sato, Hirohazu Takahashi, Atsushi Watanabe and Hiroyuki Ota, *Appl. Phys. Lett.*, **68**, 1996, 3617.

[2.08]R. T. Lee and G. B. Stringfellow, *J. Electron. Mater.,* **28** (8).

[2.09]S. S. Liu and D. A. Stevenson, *J. Electrochem. Soc.*, **125** (7), 1978, 1161

[2.10]Holleman, A. F.; Wiberg, E. "Inorganic Chemistry" Academic Press: San

Diego, 2001. ISBN 0-12-352651-5.

[2.11]J.I. Goldestein, D.E. Newbury, P. Echlin, D.C. Joy, C.E. Lyman, and E. Lifshin, L. Sawyer and J.R. Michael: *Scanning Electron Microscopy and X-Ray Microanalysis,* 3rd edition, (Plenum Press, New York 2003).

[2.12]D.B. Williams and C. B. Carter: *Transmission Electron Microscopy,* Plenum Press, New York 1996.

[2.13]R.J. Keyse, A.J. Garratt-Reed, R.J. Goodhew, and G.W. Lorimer: *Introduction to Scanning Transmission Electron Microscopy,* Springer, New York 1998.

[2.14]B.G. Yacobi and D.B. Holt: *Cathodolumiescence Microscopy of Inorganic Solids* (Plenum Press, New York 1990).

[2.15]B.G. Yacobi: *Encyclopedia of Materials Characterization: Cathodoluminescence, CL,* edited by C.R. Brundle, C.A. Evans, S. Wilson, and L.E. Fitzpatrick (Butterworth-Heinemann, Boston 1992), 149-159.

[2.16]S.O. Kasap: *Principles of Electronic Materials and Devices* (McGraw-Hill, New York 2002).

[2.17]H. Morkoç: *Nitride Semi-conductors and Devices,* 2nd edition (Springer, Berlin Heidelberg 1999).

Table 2.01. Interplanar distances in sapphire. (Cu-radiation)

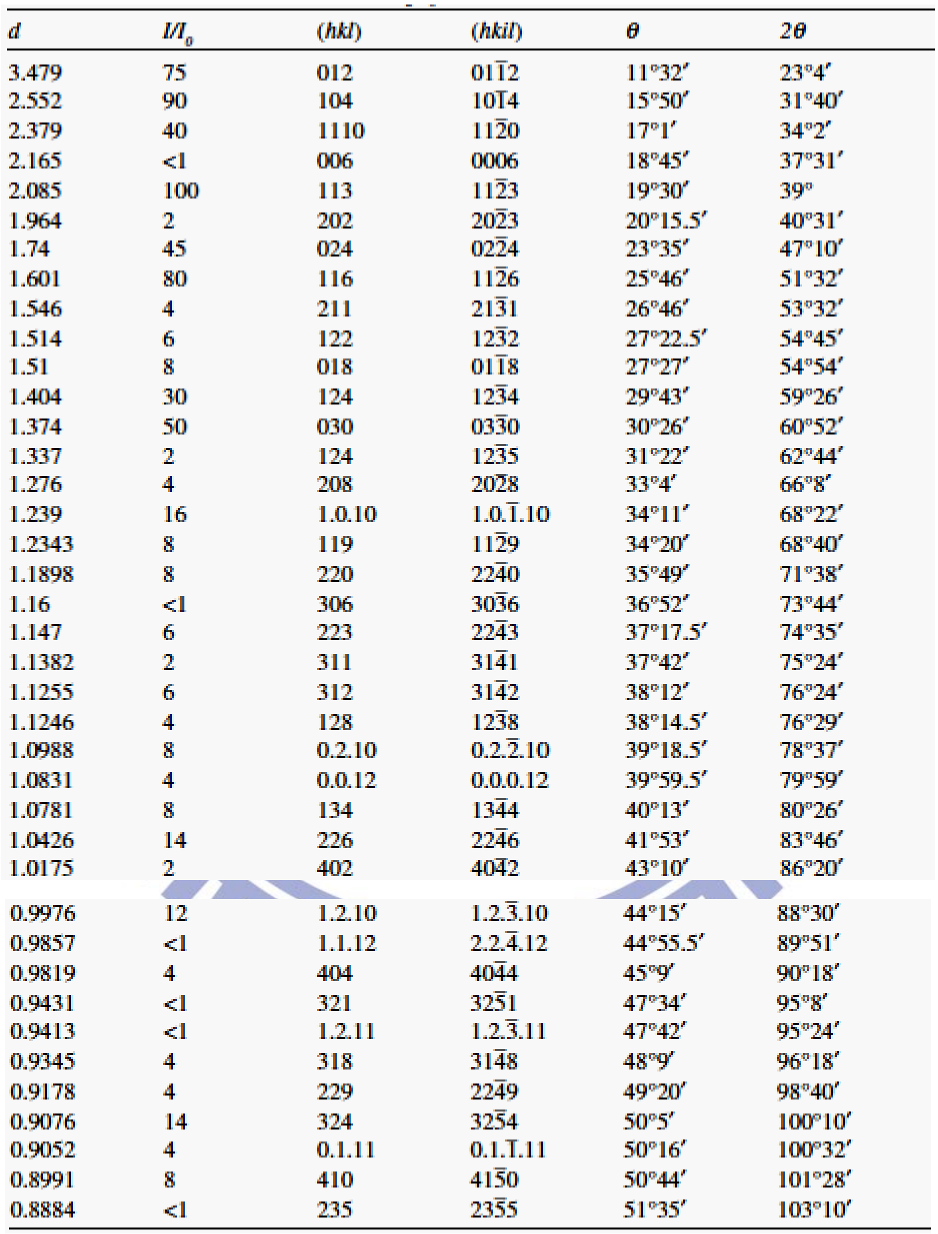

d	I/I_0	(*hkl*)	(*hkil*)	θ	2θ
3.479	75	012	$01\bar{1}2$	11°32′	23°4′
2.552	90	104	$10\bar{1}4$	15°50′	31°40′
2.379	40	1110	$11\bar{2}0$	17°1′	34°2′
2.165	<1	006	0006	18°45′	37°31′
2.085	100	113	$11\bar{2}3$	19°30′	39°
1.964	2	202	$20\bar{2}3$	20°15.5′	40°31′
1.74	45	024	$02\bar{2}4$	23°35′	47°10′
1.601	80	116	$11\bar{2}6$	25°46′	51°32′
1.546	4	211	$21\bar{3}1$	26°46′	53°32′
1.514	6	122	$12\bar{3}2$	27°22.5′	54°45′
1.51	8	018	$01\bar{1}8$	27°27′	54°54′
1.404	30	124	$12\bar{3}4$	29°43′	59°26′
1.374	50	030	$03\bar{3}0$	30°26′	60°52′
1.337	2	124	$12\bar{3}5$	31°22′	62°44′
1.276	4	208	$20\bar{2}8$	33°4′	66°8′
1.239	16	1.0.10	$1.0.\bar{1}.10$	34°11′	68°22′
1.2343	8	119	$11\bar{2}9$	34°20′	68°40′
1.1898	8	220	$22\bar{4}0$	35°49′	71°38′
1.16	<1	306	$30\bar{3}6$	36°52′	73°44′
1.147	6	223	$22\bar{4}3$	37°17.5′	74°35′
1.1382	2	311	$31\bar{4}1$	37°42′	75°24′
1.1255	6	312	$31\bar{4}2$	38°12′	76°24′
1.1246	4	128	$12\bar{3}8$	38°14.5′	76°29′
1.0988	8	0.2.10	$0.2.\bar{2}.10$	39°18.5′	78°37′
1.0831	4	0.0.12	0.0.0.12	39°59.5′	79°59′
1.0781	8	134	$13\bar{4}4$	40°13′	80°26′
1.0426	14	226	$22\bar{4}6$	41°53′	83°46′
1.0175	2	402	$40\bar{4}2$	43°10′	86°20′
0.9976	12	1.2.10	$1.2.\bar{3}.10$	44°15′	88°30′
0.9857	<1	1.1.12	$2.2.\bar{4}.12$	44°55.5′	89°51′
0.9819	4	404	$40\bar{4}4$	45°9′	90°18′
0.9431	<1	321	$32\bar{5}1$	47°34′	95°8′
0.9413	<1	1.2.11	$1.2.\bar{3}.11$	47°42′	95°24′
0.9345	4	318	$31\bar{4}8$	48°9′	96°18′
0.9178	4	229	$22\bar{4}9$	49°20′	98°40′
0.9076	14	324	$32\bar{5}4$	50°5′	100°10′
0.9052	4	0.1.11	$0.1.\bar{1}.11$	50°16′	100°32′
0.8991	8	410	$41\bar{5}0$	50°44′	101°28′
0.8884	<1	235	$23\bar{5}5$	51°35′	103°10′

Table 2.02. Symbols of crystallographic planes in morphological and structural units

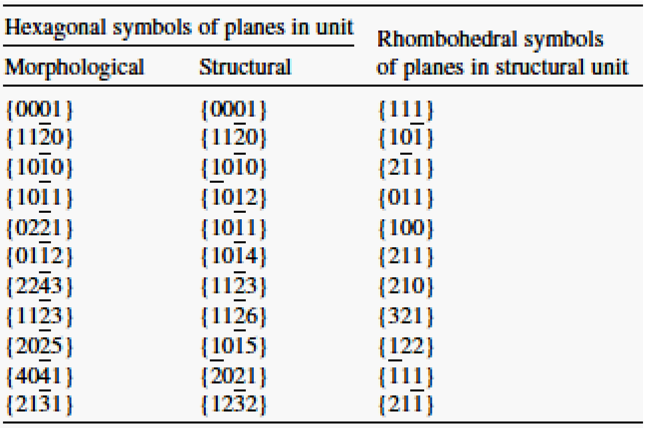

Hexagonal symbols of planes in unit		Rhombohedral symbols of planes in structural unit
Morphological	Structural	
$\{0001\}$	$\{0001\}$	$\{111\}$
$\{11\bar{2}0\}$	$\{11\bar{2}0\}$	$\{10\bar{1}\}$
$\{10\bar{1}0\}$	$\{10\bar{1}0\}$	$\{2\bar{1}1\}$
$\{10\bar{1}1\}$	$\{\bar{1}012\}$	$\{011\}$
$\{02\bar{2}1\}$	$\{10\bar{1}1\}$	$\{100\}$
$\{01\bar{1}2\}$	$\{10\bar{1}4\}$	$\{211\}$
$\{22\bar{4}3\}$	$\{11\bar{2}3\}$	$\{210\}$
$\{11\bar{2}3\}$	$\{11\bar{2}6\}$	$\{321\}$
$\{20\bar{2}5\}$	$\{\bar{1}015\}$	$\{122\}$
$\{40\bar{4}1\}$	$\{\bar{2}021\}$	$\{\bar{1}11\}$
$\{21\bar{3}1\}$	$\{12\bar{3}2\}$	$\{21\bar{1}\}$

Table 2.03. Wulff-Bragg's angles for some GaN planes

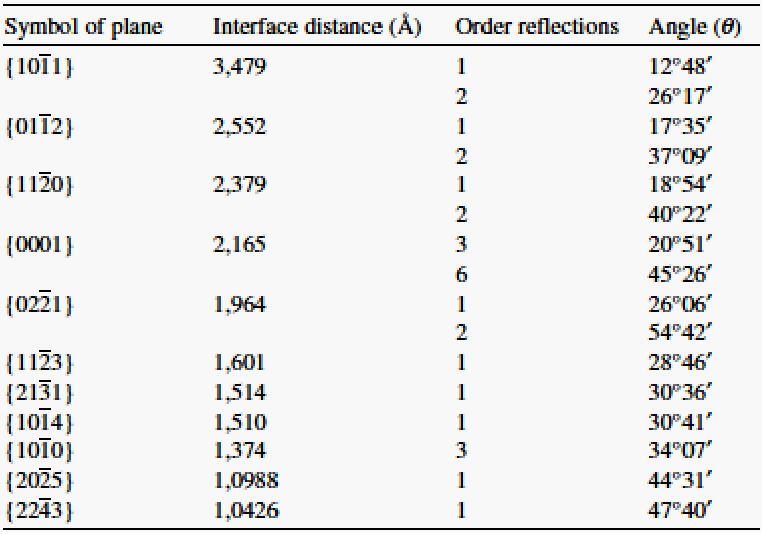

Symbol of plane	Interface distance (Å)	Order reflections	Angle (θ)
$\{10\bar{1}1\}$	3,479	1	12°48′
		2	26°17′
$\{01\bar{1}2\}$	2,552	1	17°35′
		2	37°09′
$\{11\bar{2}0\}$	2,379	1	18°54′
		2	40°22′
$\{0001\}$	2,165	3	20°51′
		6	45°26′
$\{02\bar{2}1\}$	1,964	1	26°06′
		2	54°42′
$\{11\bar{2}3\}$	1,601	1	28°46′
$\{21\bar{3}1\}$	1,514	1	30°36′
$\{10\bar{1}4\}$	1,510	1	30°41′
$\{10\bar{1}0\}$	1,374	3	34°07′
$\{20\bar{2}5\}$	1,0988	1	44°31′
$\{22\bar{4}3\}$	1,0426	1	47°40′

Table 2.04. Crystallographic planes of sapphire lattice and their spherical coordinates

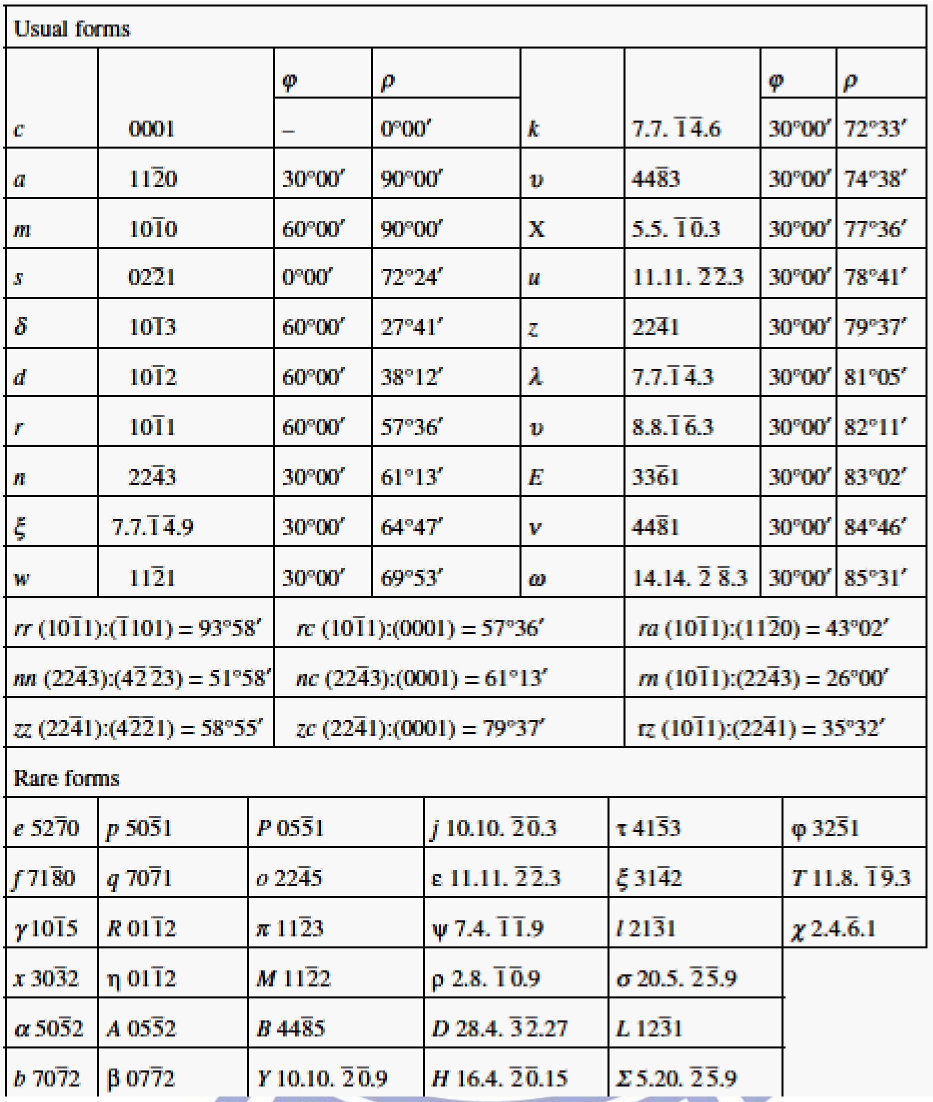

Usual forms

		φ	ρ			φ	ρ
c	0001	–	0°00′	*k*	$7.7.\overline{14}.6$	30°00′	72°33′
a	$11\bar{2}0$	30°00′	90°00′	*υ*	$44\bar{8}3$	30°00′	74°38′
m	$10\bar{1}0$	60°00′	90°00′	X	$5.5.\overline{10}.3$	30°00′	77°36′
s	$02\bar{2}1$	0°00′	72°24′	*u*	$11.11.\overline{22}.3$	30°00′	78°41′
δ	$10\bar{1}3$	60°00′	27°41′	*z*	$22\bar{4}1$	30°00′	79°37′
d	$10\bar{1}2$	60°00′	38°12′	*λ*	$7.7.\overline{14}.3$	30°00′	81°05′
r	$10\bar{1}1$	60°00′	57°36′	*υ*	$8.8.\overline{16}.3$	30°00′	82°11′
n	$22\bar{4}3$	30°00′	61°13′	*E*	$33\bar{6}1$	30°00′	83°02′
ξ	$7.7.\overline{14}.9$	30°00′	64°47′	*ν*	$44\bar{8}1$	30°00′	84°46′
w	$11\bar{2}1$	30°00′	69°53′	*ω*	$14.14.\overline{28}.3$	30°00′	85°31′

rr $(10\bar{1}1):(\bar{1}101) = 93°58′$	*rc* $(10\bar{1}1):(0001) = 57°36′$	*ra* $(10\bar{1}1):(11\bar{2}0) = 43°02′$
nn $(22\bar{4}3):(4\bar{2}\bar{2}3) = 51°58′$	*nc* $(22\bar{4}3):(0001) = 61°13′$	*rn* $(10\bar{1}1):(22\bar{4}3) = 26°00′$
zz $(22\bar{4}1):(4\bar{2}\bar{2}1) = 58°55′$	*zc* $(22\bar{4}1):(0001) = 79°37′$	*rz* $(10\bar{1}1):(22\bar{4}1) = 35°32′$

Rare forms

e $52\bar{7}0$	*p* $50\bar{5}1$	*P* $05\bar{5}1$	*j* $10.10.\overline{20}.3$	τ $41\bar{5}3$	φ $32\bar{5}1$
f $71\bar{8}0$	*q* $70\bar{7}1$	*o* $22\bar{4}5$	ε $11.11.\overline{22}.3$	ξ $31\bar{4}2$	*T* $11.8.\overline{19}.3$
γ $10\bar{1}5$	*R* $01\bar{1}2$	*π* $11\bar{2}3$	ψ $7.4.\overline{11}.9$	*l* $21\bar{3}1$	*χ* $2.4.\bar{6}.1$
x $30\bar{3}2$	η $01\bar{1}2$	*M* $11\bar{2}2$	ρ $2.8.\overline{10}.9$	*σ* $20.5.\overline{25}.9$	
α $50\bar{5}2$	*A* $05\bar{5}2$	*B* $44\bar{8}5$	*D* $28.4.\overline{32}.27$	*L* $12\bar{3}1$	
b $70\bar{7}2$	β $07\bar{7}2$	*Y* $10.10.\overline{20}.9$	*H* $16.4.\overline{20}.15$	*Σ* $5.20.\overline{25}.9$	

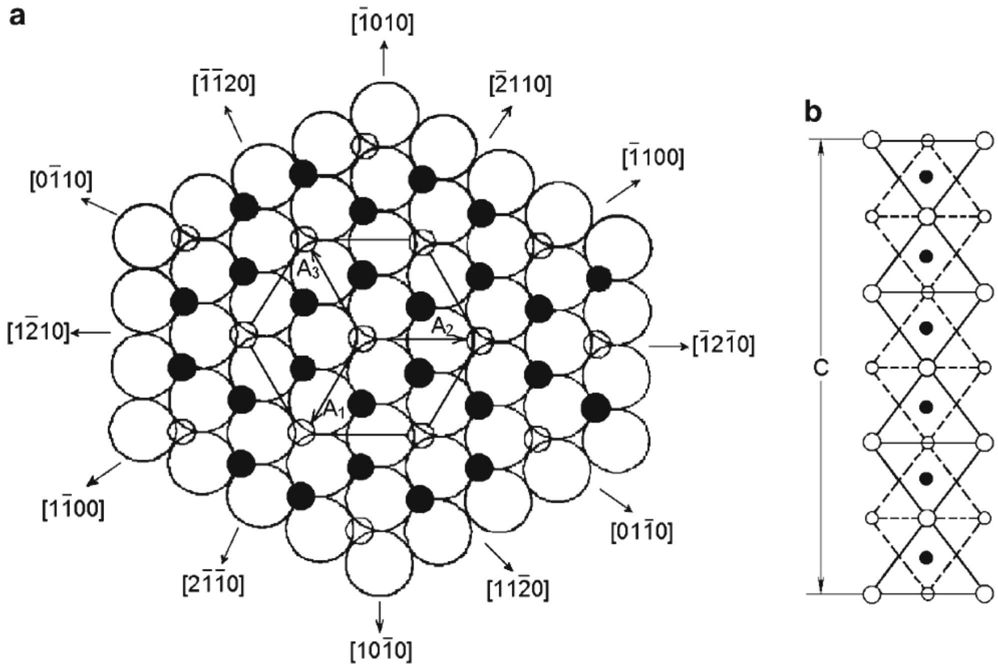

Figure 2.01. (a)Schematic of the arrangement of Al^{3+} (black circles) and octahedral hollows (small light circles) between two layers of O^{2-} (large light circles) in the basal plane.

(b) Schematic of the packing of O^{2-} ions (light circles) and Al^{3+} in the direction of the axis *c*.

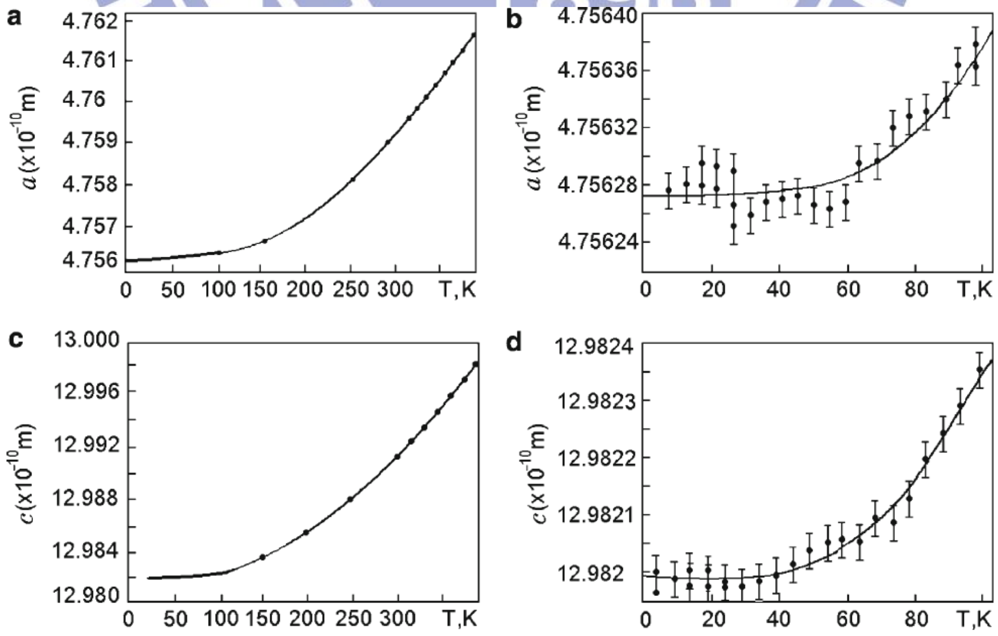

Figure 2.02. Sapphire lattice parameters in the 4.5~374K temperature range (a, c) and more detailed measurements at temperatures below 100K (b, d).

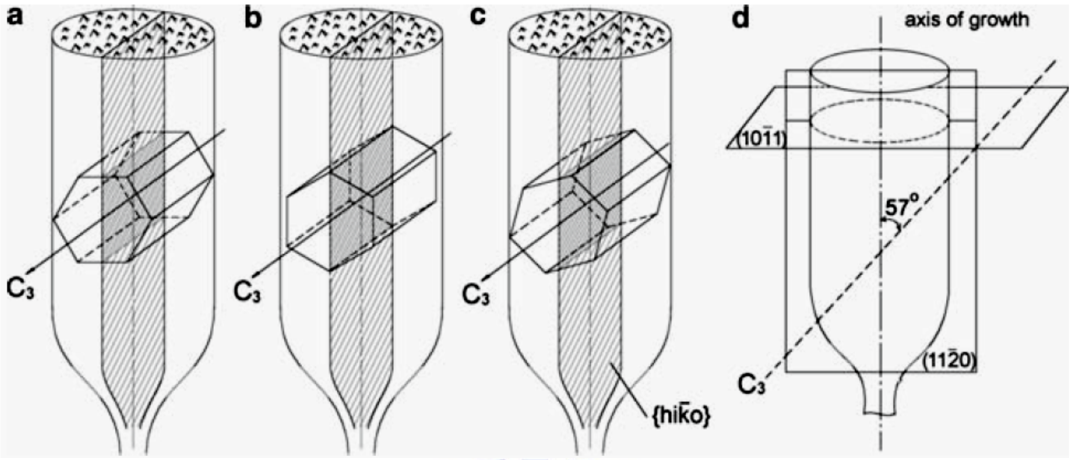

Figure 2.03. Location of the symmetry elements and the plane of chipping in the crystals grown by the Verneuil method: (a) chip along the plane (11-20); (b) chip along the plane (10-10), (c) chip along the prism (*hi*-*k*0), (d) The location of the planes (11-20) and (10-11) with respect to the growth axis and to the *c*-axis for optimization of chipping.

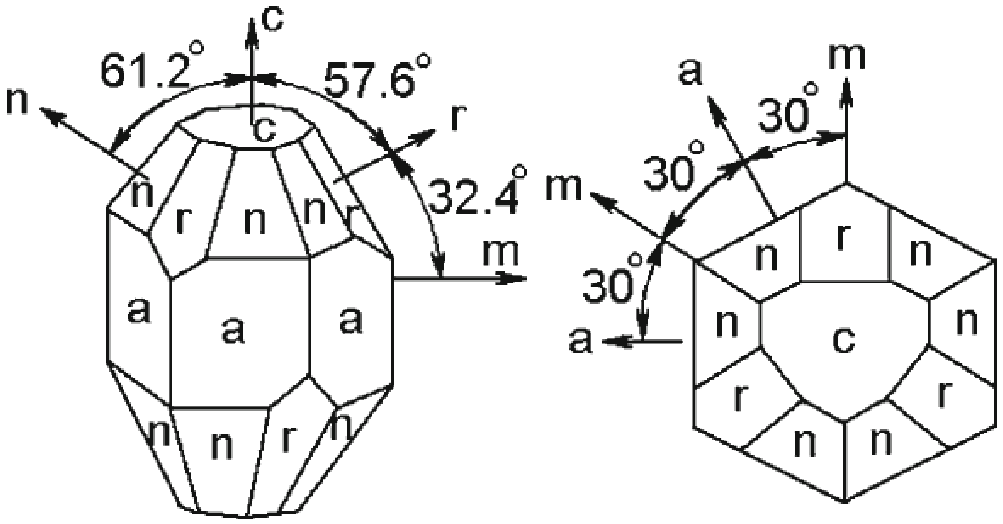

Figure 2.04. Crystallographic diagram of sapphire.

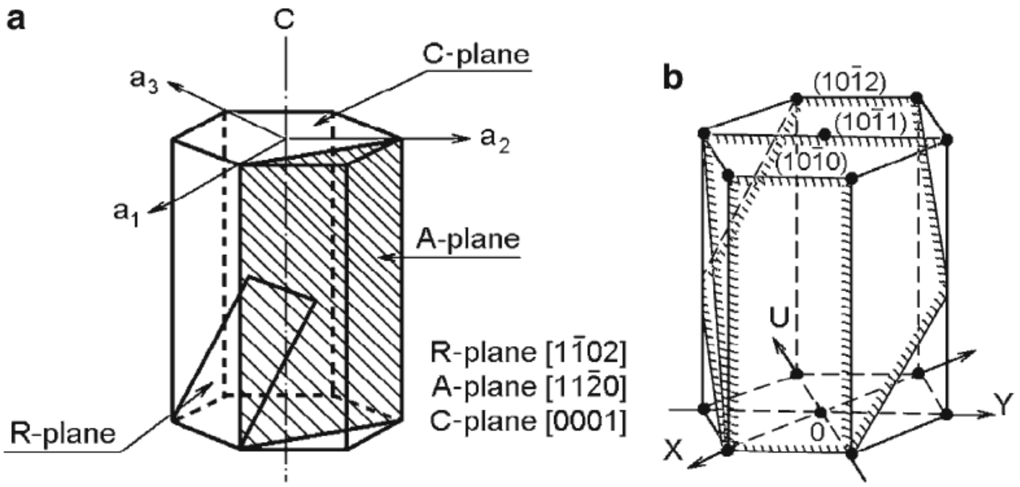

Figure 2.05. (a) Location of the crystallographic planes of sapphire often met in practice. (b) Comparison of the symbols of facets with common trace.

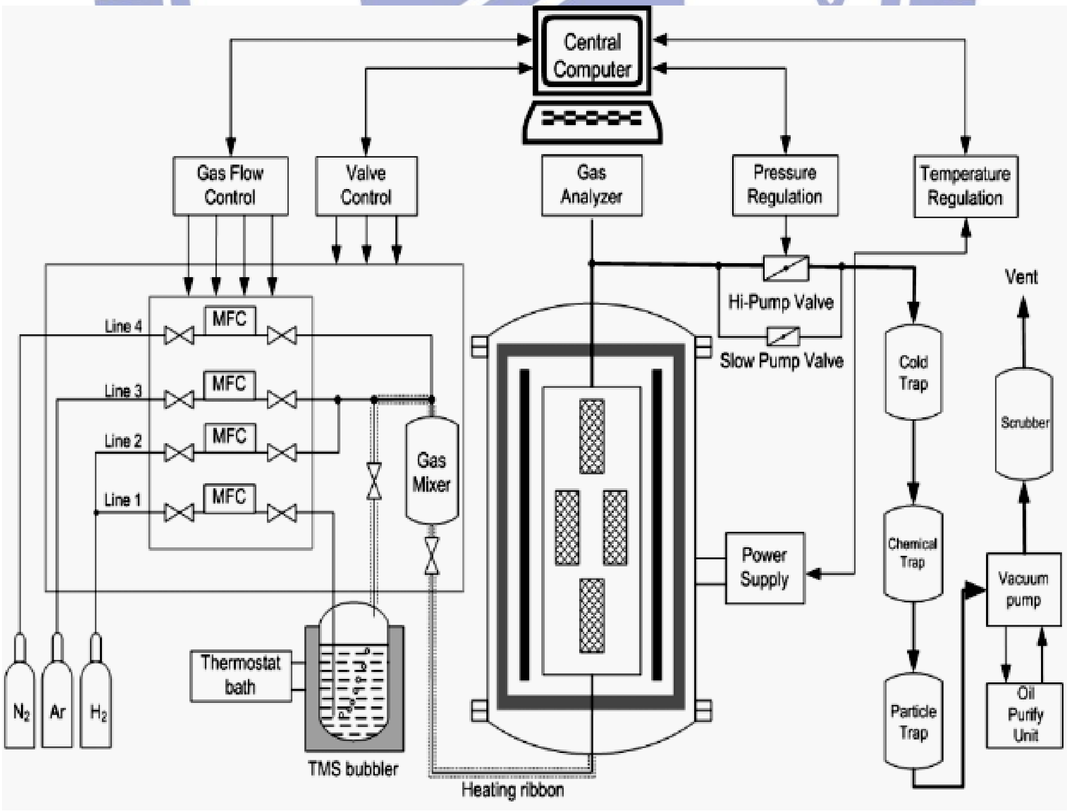

Figure 2.06. Description of subsystems in a MOCVD apparatus.

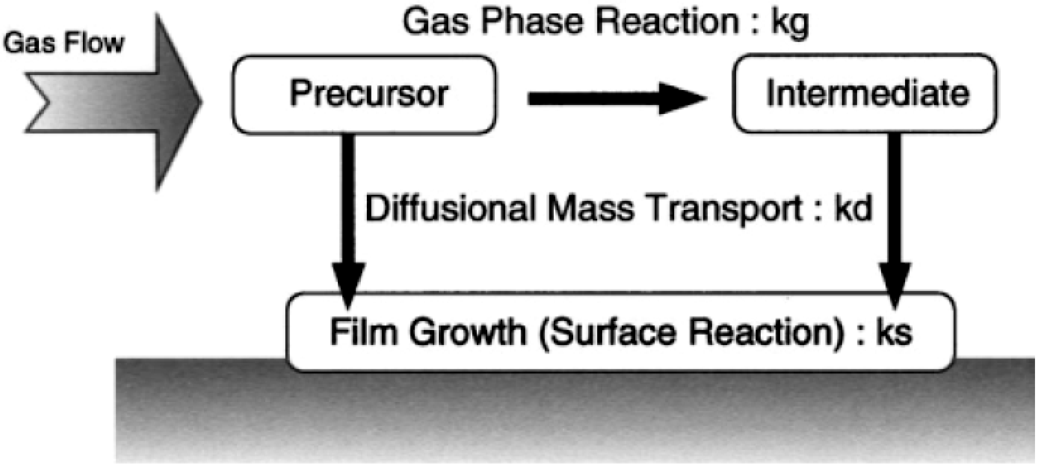

Figure 2.07. Illustration of the precursors impinging on the wafer surface and the rest products.

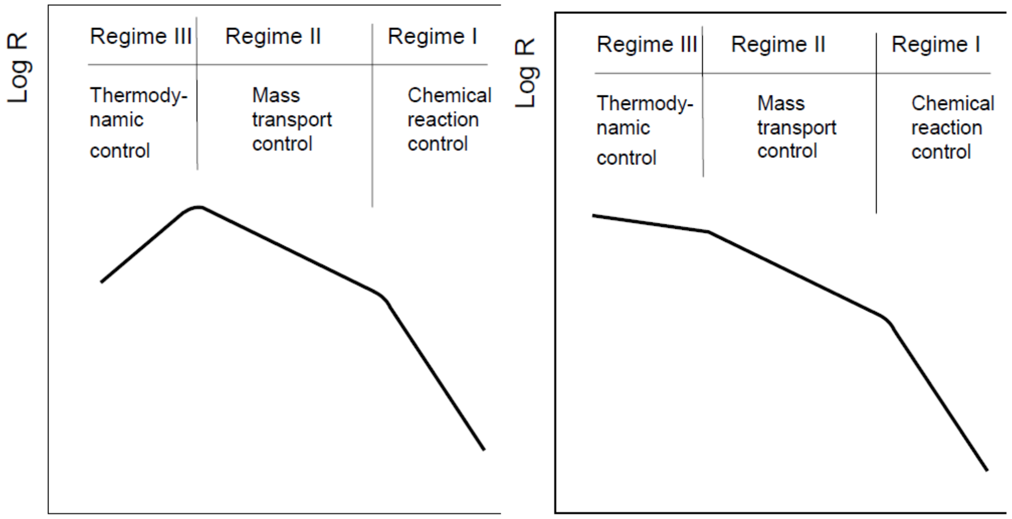

(a) (b)

Figure 2.08. Temperature dependence of the deposition rate: (a) exothermic reaction and (b) endothermic reaction

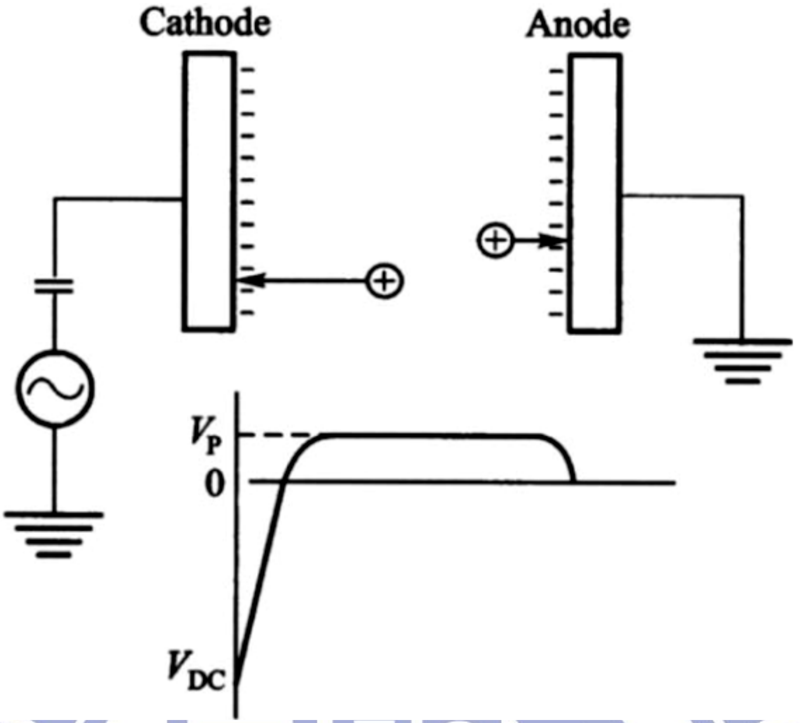

Figure 2.09. Fundamental physical operating mechanism of HDP-RIE.

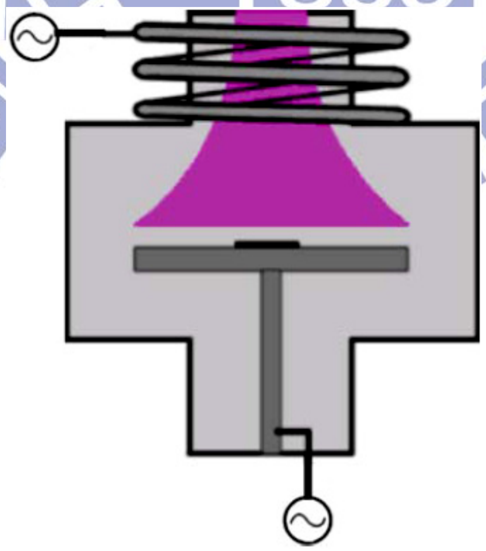

Figure 2.10. Schematic of inductive coupling plasma source.

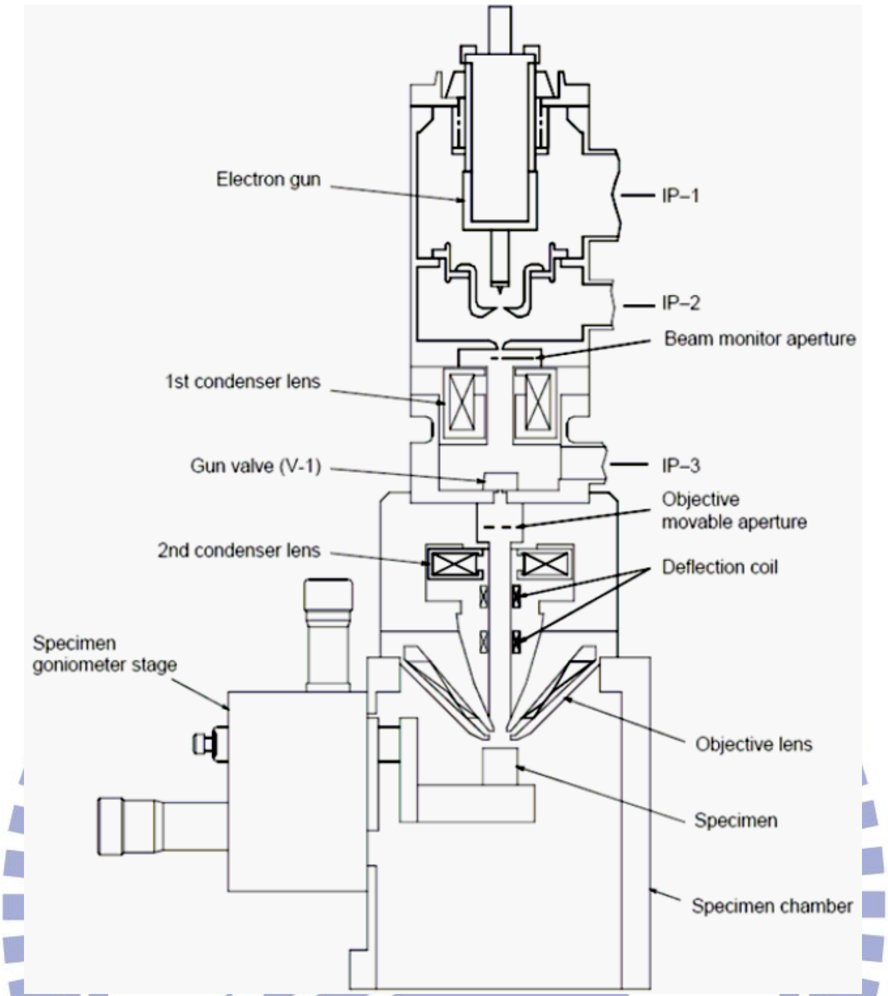

Figure 2.11. Schematic of SEM.

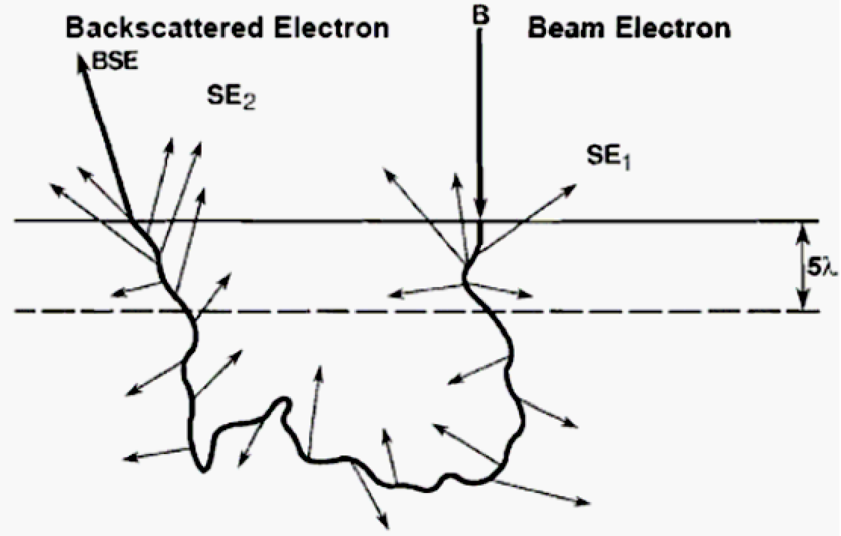

Figure 2.12. Schematic illustration of the origin of two sources of secondary electron generation in the sample.

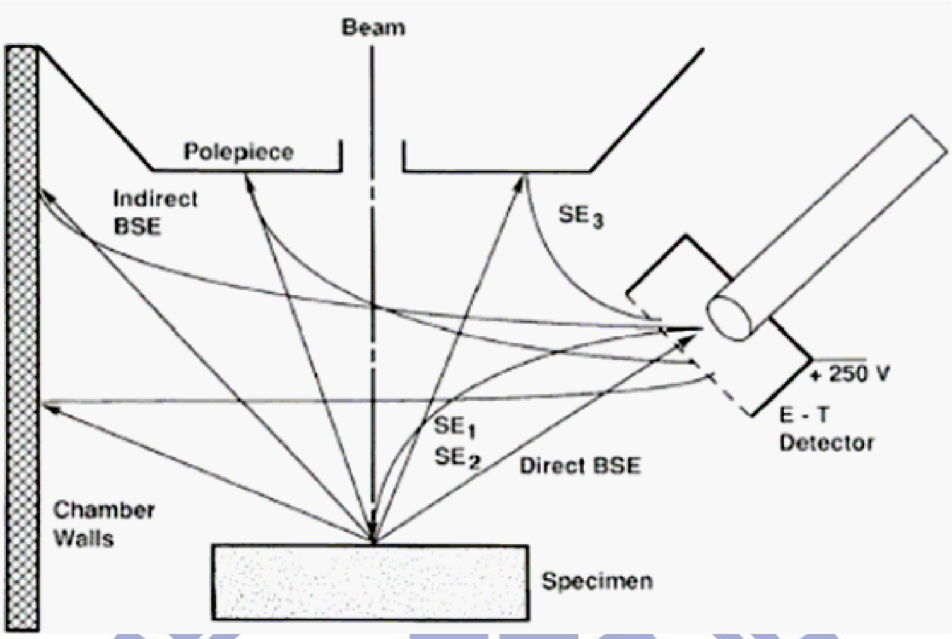

Figure 2.13. Schematic illustration of the indirect collection of backscattered electrons by a positively biased E-T detector.

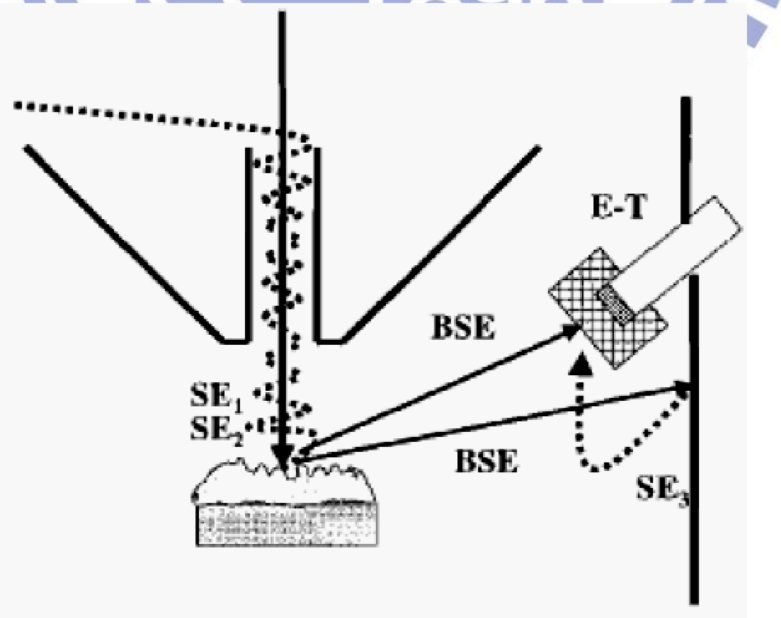

Figure 2.14. Through-the-lens (TTL) detector for SE used in high-performance field emission SEMs.

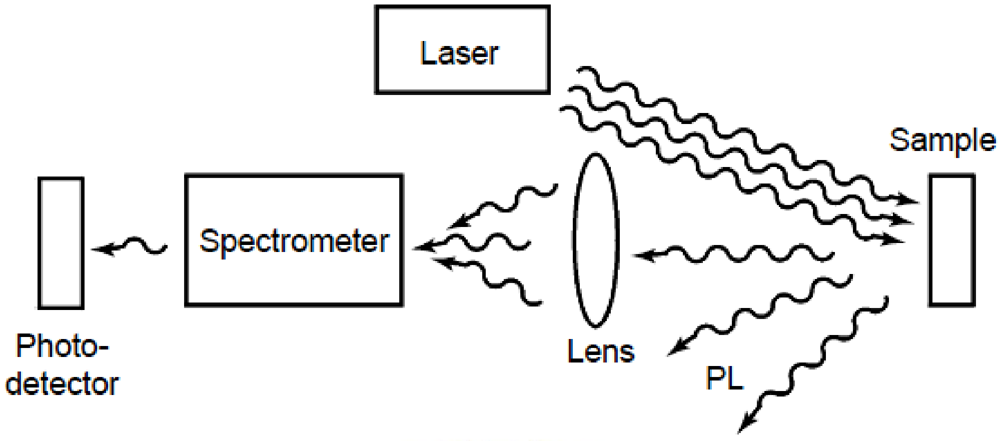

Figure 2.15. Typical experimental set-up for PL measurements.

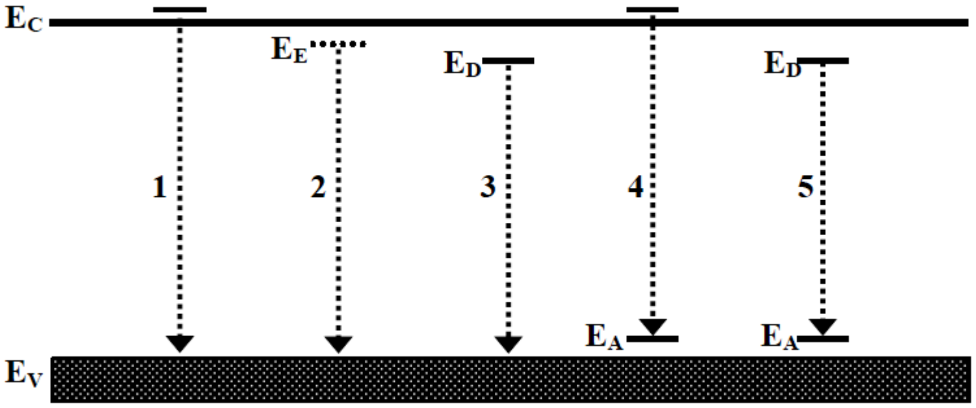

Figure 2.16. Schematic of the luminescence transitions between the conduction band (E_C), valence band (E_V), excition (E_E), donor (E_D), and acceptor (E_A) levels in a luminescent material.

Chapter 3

Experimental Procedures

3.1 Epitaxial Relationship of Gallium Nitride on Sapphire Heterosubstrate

Lacking of native substrate for GaN epitaxy layer, it is grown on foreign substrates, usually with huge lattice mismatch. Therefore, the tendency of internal strain minimization leads to a substrate-dependent atomic arrangement different from that of the heterosubstrate.

Sapphire, an ubiquitous substrate, on which can grow semiconductors including GaN. It remains the most frequently used substrate for group III-nitride epitaxial growth owing to low cost, the availability of 3-inches diameter crystals, transparent nature, thermal stability and a mature technology for nitride growth.

Delving into the orientation relationship between the GaN epilayer and underlying sapphire substrate, notations of Miller ($hjkl$) indices is warranted.

The orientation order of the GaN films grown on the main sapphire planes {basal, *c*-plane (0001), *a*-plane (11-20), and γ-plane (1-102)} by both MBE and MOCVD has been studied in great detail [3.01-3.03]. The epitaxial relationship between GaN and sapphire is insensitive to the method of growth. A few examples of the film/substrate epitaxial relationships are [3.04]: $(0001)_{\mathrm{GaN}} \parallel (0001)_{\mathrm{sapphire}}$ with [2-1-1

0]$_{\mathrm{GaN}}$ || [1-100]$_{\mathrm{sapphire}}$ and [1-100]$_{\mathrm{GaN}}$ || [1-210]$_{\mathrm{sapphire}}$; (2-1-10)$_{\mathrm{GaN}}$ || (01-12)$_{\mathrm{sapphire}}$ with [0001]$_{\mathrm{GaN}}$ || [0-111]$_{\mathrm{sapphire}}$ and [0-110]$_{\mathrm{GaN}}$ || [2-1-10]$_{\mathrm{sapphire}}$.

In the case of *a*-plane GaN on *γ*-plane sapphire, the epitaxial relationships are (11-20) *a*-plane GaN on (1-102) *γ*-plane sapphire with [11-20]$_{\mathrm{GaN}}$ || [1-102]$_{\mathrm{sapphire}}$, [0001]$_{\mathrm{GaN}}$ || [-1101]$_{\mathrm{sapphire}}$, and [-1100]$_{\mathrm{GaN}}$ || [11-20]$_{\mathrm{sapphire}}$ owing to hexagonal symmetry. Table 3.01 shows the summary representation of epitaxial relationships of GaN grown on various planes of sapphire heterosubstrate.

The calculated lattice mismatch between the basal GaN and the basal sapphire plane is larger than 30%. However, the actual mismatch is only

$$\frac{\sqrt{3}a_{w\mathrm{GaN}} - a_{\mathrm{sapphire}}}{a_{\mathrm{sapphire}}} = 0.16, \tag{3.01}$$

because the small cell of Al atoms on the basal sapphire plane is oriented 30° away from the larger sapphire unit cell. This smaller lattice mismatch can be calculated by adopting the model explained in figure 3.01. It is on this plane that the best gallium nitride has been grown with relatively small in- and out-of-plane misorientations. In general, gallium nitride on this plane show almost perfect wurtzite phase.

GaN grown on the (11-20) *a*-plane sapphire turns out to be (0001) oriented and anisotropically compressed. The in-plane relationship of GaN and sapphire is depicted in figure 3.02 where the [11-20]$_{\mathrm{GaN}}$ is aligned with the [0001]$_{\mathrm{sapphire}}$. In this orientation, the bulk positions of both the substrate and the GaN cations lie along the sapphire [0001] direction. The mismatch between the substrate and the film is

$$\frac{c_{\mathrm{sapphire}} - 4a_{w\mathrm{GaN}}}{c_{\mathrm{sapphire}}} = 0.02, \tag{3.02}$$

and for the [1-100]$_{\text{GaN}}$ parallel to the [1-100]$_{\text{sapphire}}$ by

$$\frac{c_{\text{sapphire}} - 1.5a_{w\text{GaN}}}{c_{\text{sapphire}}} = -0.005 . \tag{3.03}$$

The aforementioned discussion is academic in that GaN grown on *a*-plane sapphire still has [0001] direction normal to the surface. However, growth on *γ*-plane with MOCVD leads to *a*-plane GaN, as in the figure3.03.

GaN films have been grown on the *γ*-plane (1-102) of sapphire purportedly to achieve a lattice mismatch smaller than on the *c*-plane sapphire. GaN grown on the *γ*-plane sapphire has been reported to assume an orientation similar to (2-1-10). The arrangement in the case of the (1-102)$_{\text{sapphire}}$ and (2-1-10)$_{\text{GaN}}$ is depicted in figure 3.04. The lattice mismatch between the [-1101]$_{\text{sapphire}}$ and the [0001]$_{\text{GaN}}$ parallel to the [-1101]$_{\text{sapphire}}$ is equal to

$$\frac{3c_{\text{GaN}} - \sqrt{\left(3a_{\text{sapphire}}^2 + c_{\text{sapphire}}^2\right)}}{\sqrt{\left(3a_{\text{sapphire}}^2 + c_{\text{sapphire}}^2\right)}} = 0.01 . \tag{3.04}$$

In the case when [1-100]$_{\text{GaN}}$ direction is parallel to the [01-2 0]$_{\text{sapphire}}$ direction, the lattice mismatch is

$$\frac{a_{w\text{GaN}} - \left(a_{\text{sapphire}}/\sqrt{3}\right)}{\left(a_{\text{sapphire}}/\sqrt{3}\right)} = 0.16 . \tag{3.05}$$

The mismatch along the [0001]$_{\text{GaN}}$ parallel to the [-1101]$_{\text{sapphire}}$ is 1%, which is much smaller than the 16% mismatch along [1-100]$_{\text{GaN}}$ parallel to the [11-20]$_{\text{sapphire}}$. Growth on the *γ*-plane exhibits ridge-like features that allow relaxation of the mismatch. It is assumed that the topmost O layer is desorbed and the Al layer of sapphire is then exposed. One thing must be stated is that the representation in figure 3.04 is very simple intended only to give a first-order glimpse as to how the *a*-plane GaN might be organized on the *γ*-plane sapphire with no consideration to energy minimization. More detail information about *γ*-plane sapphire can be seen in figure 3.05.

3.2 Nonpolar *a*-Plane GaN on m-Plane Sapphire

On considering the aforementioned epitaxial relationship between GaN and sapphire substrate, the best GaN can be grown with relatively small in- and out-of-plane misorientations from the *c*-plane sapphire. Therefore the epitaxial direction and initial plane we chose are along c-direction from *c*-plane sapphire respectively. From the basic crystalline structure of wurtzite, as in figure 3.06, it is clear that *c*-plane, *a*-plane and *m*-plane are perpendicular to each other. To achieve the demand of growing nonpolar *a*-plane GaN on *m*-plane sapphire substrate, appropriate substrate engineering is necessary to effectively expose the *c*-plane of sapphire.

The applied substrate engineering here in this experiment was artificial surface patterning. The trench-patterned nonpolar *m*-plane sapphire substrate was fabricated by e-gun evaporated nickel mask and Cl_2-based inductively coupled plasma reactive ion etching (ICP-RIE). Via accurate lithography aligning, symmetric crystallographic *c*-plane facets of sapphire with terrace/trench width 4μm/2μm and 3μm etching depth were illustrated in Figure 3.07. To effectively expose the *c*-plane sapphire sidewalls, terrace/trench stripes orientation were chosen parallel to $[11\text{-}20]_{\text{sapphire}}$.

The growth of GaN on the trench-patterned m-plane sapphire was performed by Metal Organic Chemical Vapor Deposition (MOCVD) system. After heating up and reaching the appropriate temperature, a 30 nm GaN buffer layer was grown at 550°C, followed by main GaN growth at 1050°C with a pressure of 100 mtorr. The different growth rate and growth mode of nonpolar *a*-plane GaN on trench-patterned *m*-plane sapphire was achieved via tuning the V/III ratio of GaN growth duration from 72 to 350, 1800 and up to 9000. In order to know the dependency of growth rate of specific plane of GaN on different V/III ratio, all the growth period are fixed to the same time. Additionally, an optimized substrate with lower terrace/trench width ratio (*i.e.* 2um/4um) is used to attempt to suppress the growth of GaN from the $(10\text{-}10)_{\text{sapphire}}$ terraces under the V/III ratio of 72. The condition of growth temperature versus growth time was summarized in figure 3.08 where the critical timing of V/III ratio tuning was depicted also.

3.3 Nonpolar *a*-plane GaN on γ-plane Sapphire

It has been demonstrated that wavy, stripe-like growth feature of nonpolar *a*-plane GaN growing epitaxially on *γ*-plane sapphire leads to a large amount of threading dislocations and stacking faults [3.06, 3.07]. These defects form nonradiative centers and bring difficulty and great challenge to the growth of high quality *a*-plane GaN inevitably. The acquirement of crystalline quality of *a*-plane GaN for further optoelectronics devices application is urgent and necessary.

Recently, the technique of epitaxially lateral overgrowth (ELOG) provided a power solution to grow *a*-plane GaN on *γ*-plane sapphire [3.08]. ELOG improves the crystalline quality by reducing the density of threading dislocations and alleviates the strain-related surface roughening and faceting. Despite the ability of improving morphology and crystalline quality, the coalescence thickness of ELOG is often more than 20μm, which is too thick to effectively control the growth uniformity. Therefore, in this experiment, a modified technique by using epitaxially lateral overgrowth on trench-patterned *a*-plane GaN buffer layer (TELOG, where "T" represents trench-patterned) is performed. Via applying this technique to growth procedure, *a*-plane GaN with relatively low dislocation density is expected. It would show the potential of simple fabrication process, low cost, and, most important of all, thinner coalescence thickness in comparison with the previous ELOG.

Figure 3.09 shows the flow chart of TELOG *a*-plane GaN growth. Initially, the *a*-plane GaN template with 1.5μm thickness was grown by MOCVD on *γ*-plane sapphire substrate using conventional two-step growth technique. Then a 3μm-seed/ 3μm-trench was applied parallel to the direction to realize vertical *c*-plane sidewalls followed by etching of SiO_2 using inductively coupled plasma reactive ion etching through the windows to the GaN epitaxial template film. These well-organized GaN stripes were etched down to the *γ*-plane sapphire substrate by reactive ion etching. The SiO_2 etching-mask was removed by hydrofluoric acid solution to avoid the complexity of growth mode. The deposition procedure of TELOG *a*-plane GaN film was performed by using a two-step growth technique. At initial, the sapphire substrate was heated to 700°C and then a nitridation process was revealed under gradually increasing temperature. A short period of ramping growth followed until the substrate was heated to the suitable growth temperature, *i.e.* 970°C. TELOG *a*-plane GaN was grown mainly at 970°C for a specific long period to achieve the fully coalescence of the surface. From nitridation step to the main TELOG step, the growth condition of V/III of MOCVD was fixed at the level of 50~100. Under this specific condition, the growth direction can be selective to +*c*-direction of sapphire and the growth rate is enhanced. To apply a pre-strain superlattice prior to the multiple quantum wells, the temperature was slightly down to 855°C. After the supperlatice growth, the quantum wells and quantum barriers were grown periodically at the temperature of 760°C and 855°C respectively. The growth temperature of wells and barriers can be changed to achieve different lighting optical wave length from UV to green light. And one thing to note is that the samples we took to perform the further experiments were in blue lighting region. From supperlattice growth step to the MQWs growth step, the growth condition of V/III of MOCVD was fixed at the level of 5000~10000. The specific condition was chosen to be similar to the general growth condition of *c*-plane GaN on *c*-plane sapphire substrate. It would be helpful in controlling the growth rate, growth mode and achieving the smooth morphology of each layer. After all, the aforementioned growth conditions are summarized in figure 3.10.

3.4 KOH Etching Procedures

The KOH etching processes are performed under standard environments with normal pressure and uniform agitation of the KOH-ethylene glycol solution. These were the controlled independent variables, *i.e.* remained fixed through the whole experimental duration of experiments. To know the complete etching behavior of TELOG *a*-plane GaN with related MQWs in KOH-ethylene glycol solution, variables including etching time, concentration of KOH-ethylene glycol solution and etching temperature were considered.

What responsible for the determination of the duration of etching is not specific but epitaxial-crystalline-quality-dependent. Here in this experiment, the etching time performed from 10 minutes to 80 minutes. An extreme long etching duration was tested to ensure the optimized window of etching.

The concentration of KOH-ethylene glycol solution is undoubtedly one of the most important factors. For the nature of chemical etching, the influence of solution concentration on etching rate of general materials is self-evident. Crystalline gallium nitride, however, shows more unique etching characteristics in chemical solutions. To effectively clarify those characteristics, different concentration with 5 wt.%, 10 wt.% and 20 wt.%, of KOH was prepared in ethylene glycol. The high boiling point and thermal stability of ethylene glycol ensured solvent against evaporation and the concentration of KOH-ethylene glycol solution, therefore, was maintained.

Temperature, which hastens etching reactions if raised, since higher temperature increases the energy of the etchants molecules, creates more collisions between etchants and materials per unit time. In general, higher temperature leads to faster reaction. The temperature effect is usually discussed in terms of activation energy, i.e. the chemical potential barrier. Here in this experiment, the etching temperature was controlled in the range of 100°C ~120°C. The heat source was supplied by commercial hot plate. To ensure the uniformity of temperature inside the solution, a gentle agitation was performed by magnetic stirring.

Briefly, the three factors, i.e. time, concentration and temperature will show its own dependency to the etching results. These specifically-arranged conditions can help in clarifying the etching windows of nonpolar gallium nitride in KOH-ethylene glycol solution. The integration of the variables is organized on the basis of the coordinate systems constructed by time, concentration and temperature. The integrated variables and experimental direction are schematically shown in figure 3.11.

3.5 Measurement and Characterization

The crystalline quality of grown samples, *a*-plane GaN on patterned *m*-plane sapphire and TELOG *a*-plane GaN on *γ*-plane sapphire were characterized by X-ray diffraction (XRD). Additionally, scanning electron microscopy (SEM) and transmission electron microscopy (TEM) are used to observe the surface morphology, growth mode, and defect distribution of the epitaxial film.

The scanning electron microscopy also provided the ability of observing the cross-sectional image of these epitaxial samples. Specially, the etching effects of TELOG *a*-plane GaN in KOH-ethylene glycol solution under different conditions are clear and unequivocal in scanning electron microscopy. This offered the important information of clarifying the etching characteristics including etching direction, etching rate, and most of all, etching mechanism.

The capable of imaging at a significantly higher resolution of Transmission electron microscopy can help in determining the defects distribution and arrangement. In accompany with the electron diffraction patterns, the types of defects in *a*-plane GaN on *m*-plane sapphire and *a*-plane GaN on *γ*-plane sapphire are clarified.

Optical properties of these *a*-plane GaN samples were investigated by uncontact and nondestructive photoluminescence spectroscopy and cathodoluminescence spectroscopy. The luminescence results can be categorized to show the lighting behavior and the crystalline quality respectively. Photoluminescence spectroscopy, in addition, provided the information of light extraction ability of KOH-ethylene glycol solution etched TELOG *a*-plane GaN MQWs. Cathodoluminescence spectroscopy mapping of the cross-sectional image of *a*-plane GaN on *m*-plane sapphire and top-plane of *a*-plane GaN on *γ*-plane sapphire revealed the relative threading dislocation density and crystalline quality of each specific region, including the original templates or lateral overgrown layers.

3.6 References

[3.01]Lei, T., Ludwig, K.F., Jr and Moustakas, T. (1993) Journal of Applied Physiology, 74, 4430.

[3.02]Powell, R.C., Lee, N.E., Kim, Y.-W. and Green, J. (1993) Journal of Applied Physiology, 73, 189.

[3.03]Tansley, T.L., Goldys, E.M., Godlewski, M., Zhou, B. and Zuo, H.Y. (1997) The contribution of defects to the electrical and optical properties of GaN, in GaN and Related Materials (ed. S. Pearton), Gordon and Breach, Amsterdam, pp. 233–295.

[3.04]Leszczynski, M. (1999) Common Crystal Structure of the Group III-Nitrides (ed. J.H. Edgar), IEE EMIS Data Review Series, No. 23, INSPEC, London, p. 6.

[3.05]Liu, L. and Edgar, J.H. (2002) Substratesfor gallium nitride epitaxy. Materials

Science & Engineering R: Reports, 37, 61–127.

[3.06]M. D. Craven, S. H. Lim, F. Wu, J. S. Speck, S. P. DenBaars, (2002) Applied Physics Letter, 81, 469.

[3.07]D. N. Zakharov, Z. L. Weber, (2005) Physical Review B, 71, 235334.

[3.08]M. D. Craven, S. H. Lim, F. Wu, J. S. Speck, S. P. DenBaars, (2002) Applied Physics Letter, 81, 1201.

Table 3.01. Crystallographic relationship between GaN films and sapphire substrates.

Crystal plane	Miller indices		GaN plane $\parallel$ sapphire surface plane ($hjkl$)	GaN direction $\parallel$ sapphire direction ($hjkl$)
	($hjkl$)	(hkl)		
c	(0001)	(001)	(0001) always	$[\bar{1}2\bar{1}0] \parallel [\bar{1}100]$, $[\bar{1}2\bar{1}0] \parallel [1\bar{1}00]$
a	$(11\bar{2}0)$	(110)	(0001) or $(10\bar{1}0)$	$[11\bar{2}0] \parallel [\bar{1}000]$, $[11\bar{2}0] \parallel [0003]$
m	$(10\bar{1}0)$	(100)	$(10\bar{1}3)$ or $(1\bar{2}12)$	$[\bar{1}2\bar{1}0] \parallel [0001]$, $[10\bar{1}0] \parallel [1\bar{2}10]$
r	$(10\bar{1}2)$	(102)	$(11\bar{2}0)$ or $(1\bar{2}10)$	$[0001] \parallel [\bar{1}\bar{1}01]$, $[0001] \parallel [\bar{1}011]$, $[1\bar{1}00] \parallel [1120]$, or $[11\bar{2}0] \parallel [\bar{1}\bar{1}02]$

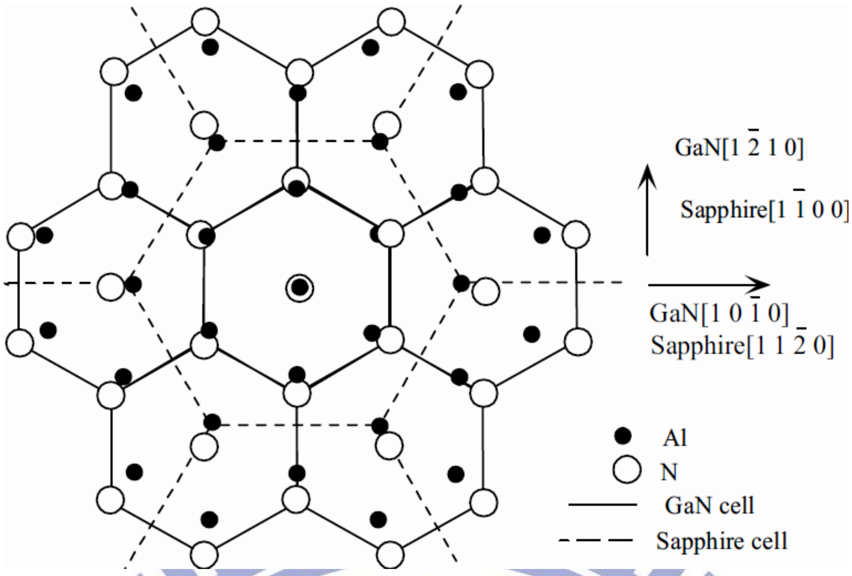

Figure 3.01. Projection of bulk basal plane sapphire and GaN cation positions for the observed epitaxial growth orientation. The circles mark Al atom positions and the dashed lines show the sapphire basal plane unit cells. The open circles mark the N-atom positions and solid lines show the GaN basal plane unit cell.

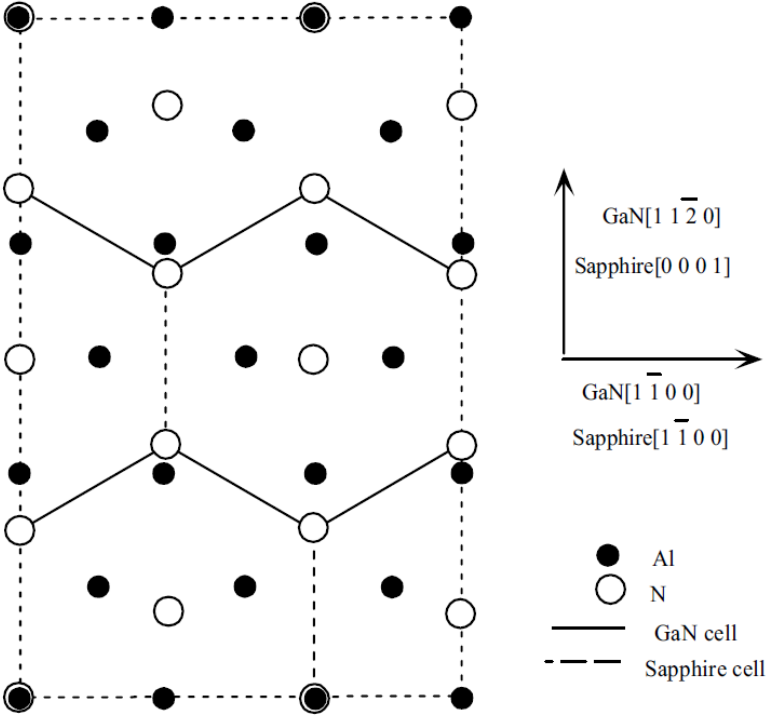

Figure 3.02. Projection of bulk *a*-plane sapphire and basal plane GaN cation positions for the observed epitaxial growth orientation. The solid circles mark the Al atom positions and the dashed lines show the sapphire *a*-plan unit cells. The open circles mark the N-atom positions and the solid lines show the GaN basal plane unit cell.

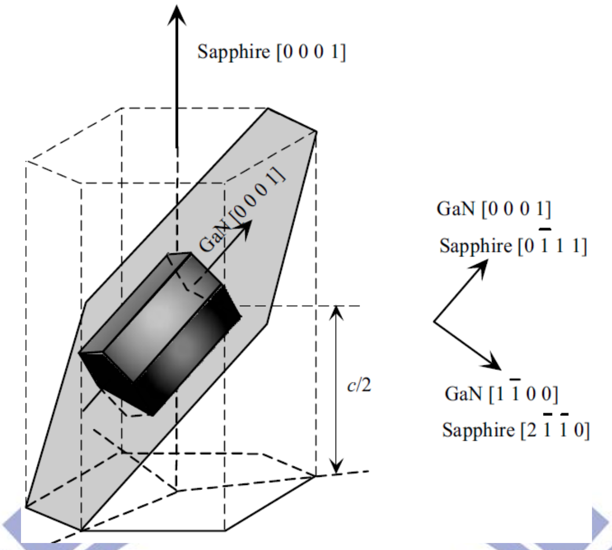

Figure 3.03. Schematics of crystallographic relationship between *a*-plane GaN and *γ*-plane sapphire.

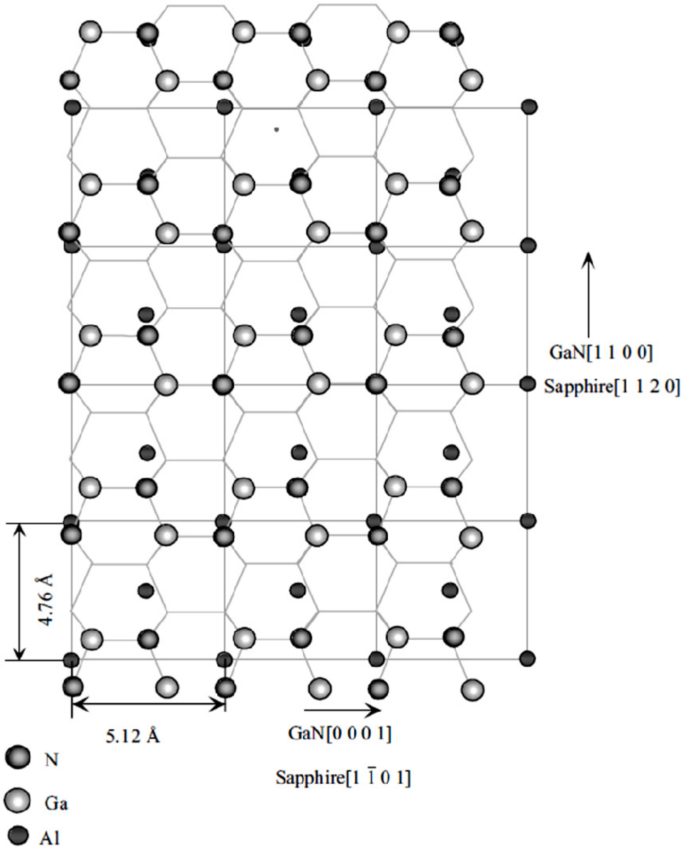

Figure 3.04. Projection of bulk *γ*-plane sapphire and *a*-plane GaN anion and cation positions for the observed epitaxial growth orientation.

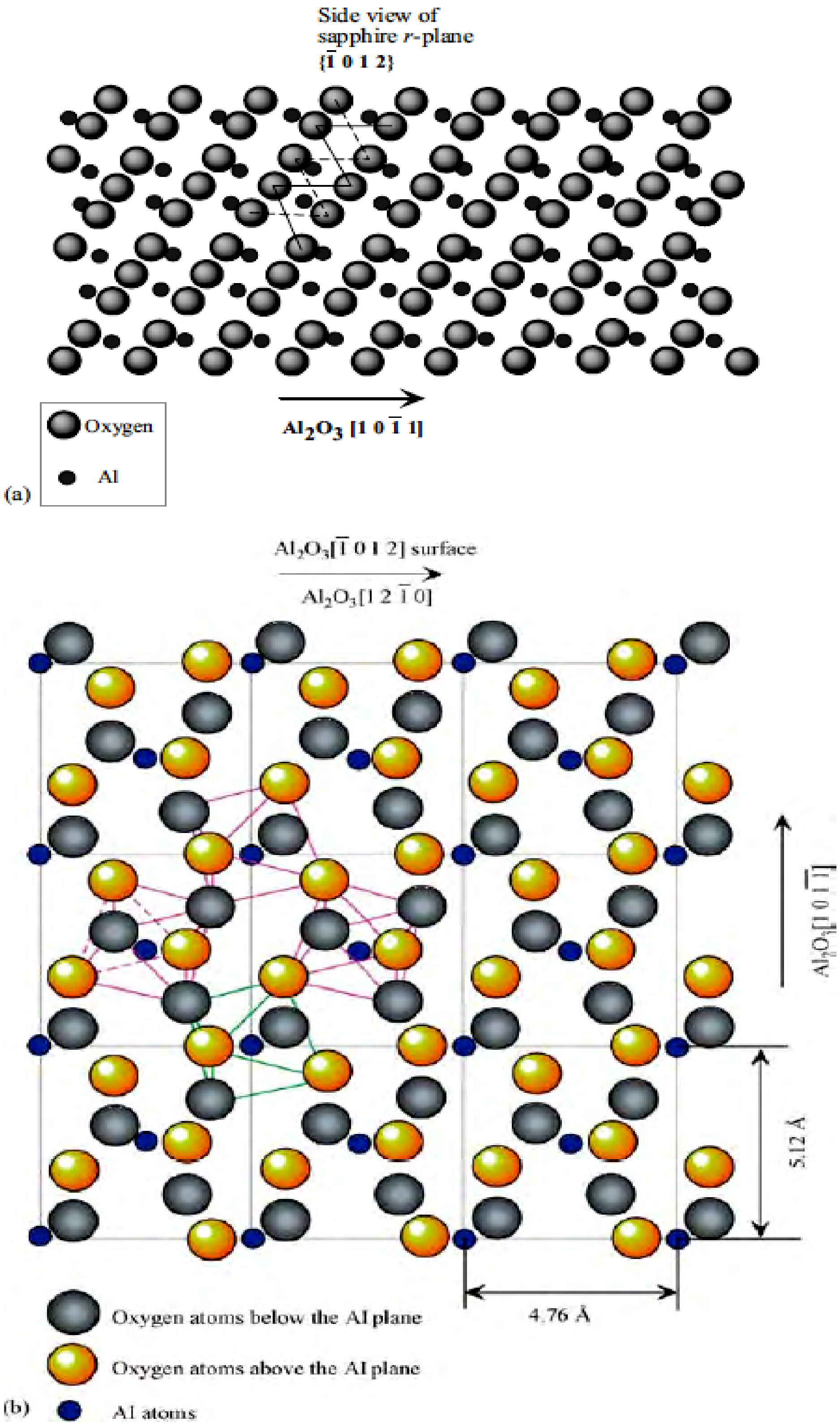

Figure 3.05. (a) Sapphire γ-plane stacking sequence showing O atoms in larger clear circles and Al atoms in smaller, filled circles. (b) The atomic arrangement on three layers (the uppermost one is O, immediately below is Al and third layer down is another O layer) on the γ-plane of sapphire.

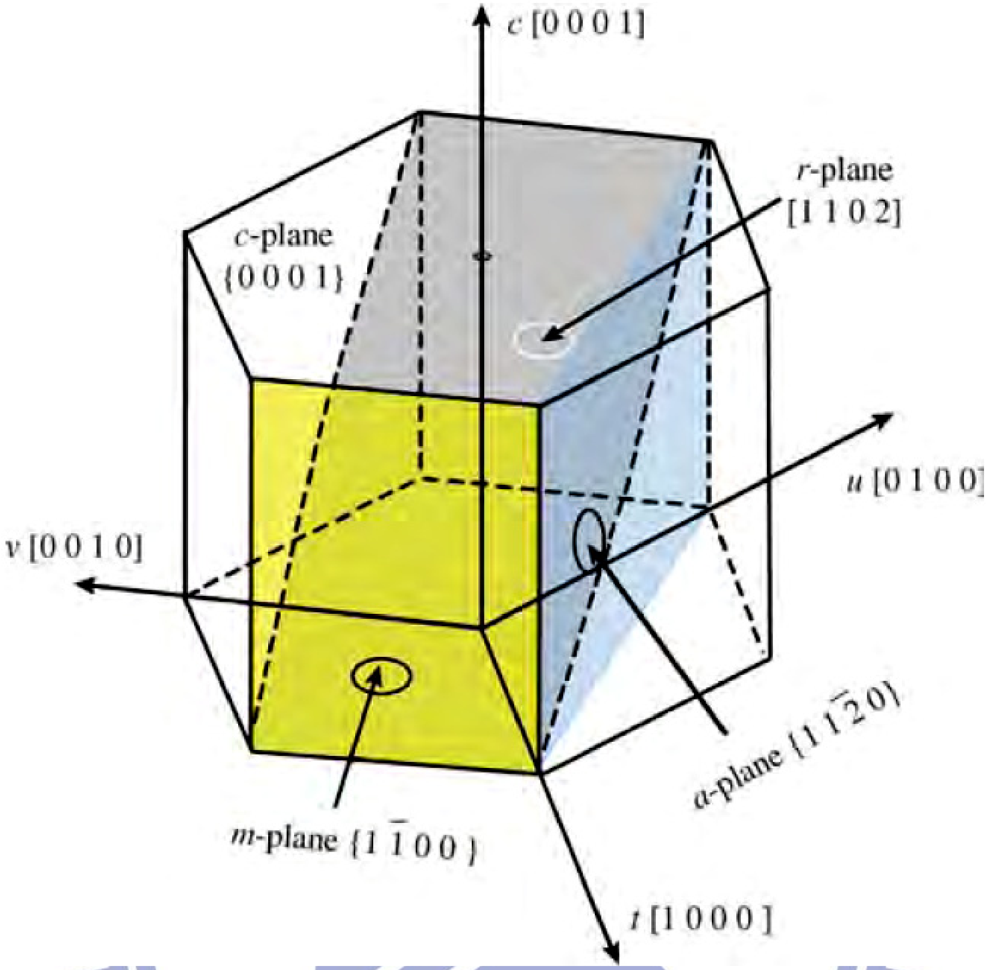

Figure 3.06. Depiction of *c*-plane, *a*-plane, *m*-plane, *γ*-plane in GaN.

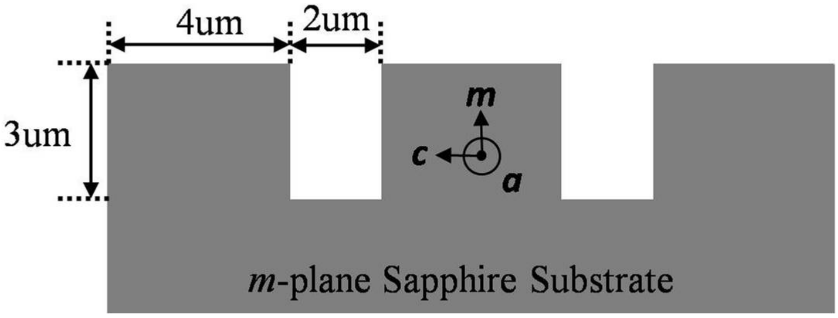

Figure 3.07. Trench-patterned *m*-plane sapphire substrate for *a*-plane GaN overgrowth.

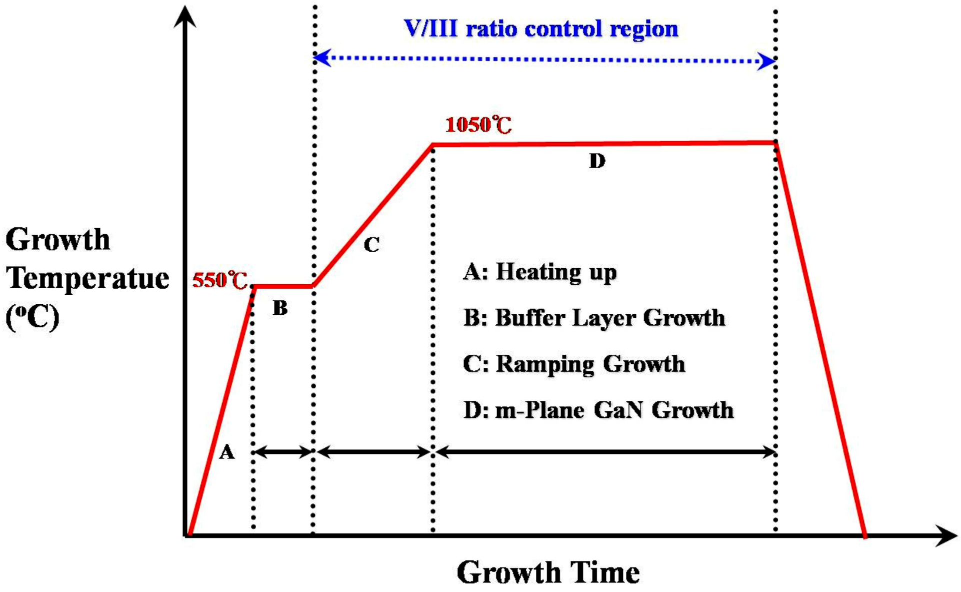

Figure 3.08. The MOCVD growth procedure for *a*-plane GaN on *m*-plane sapphire.

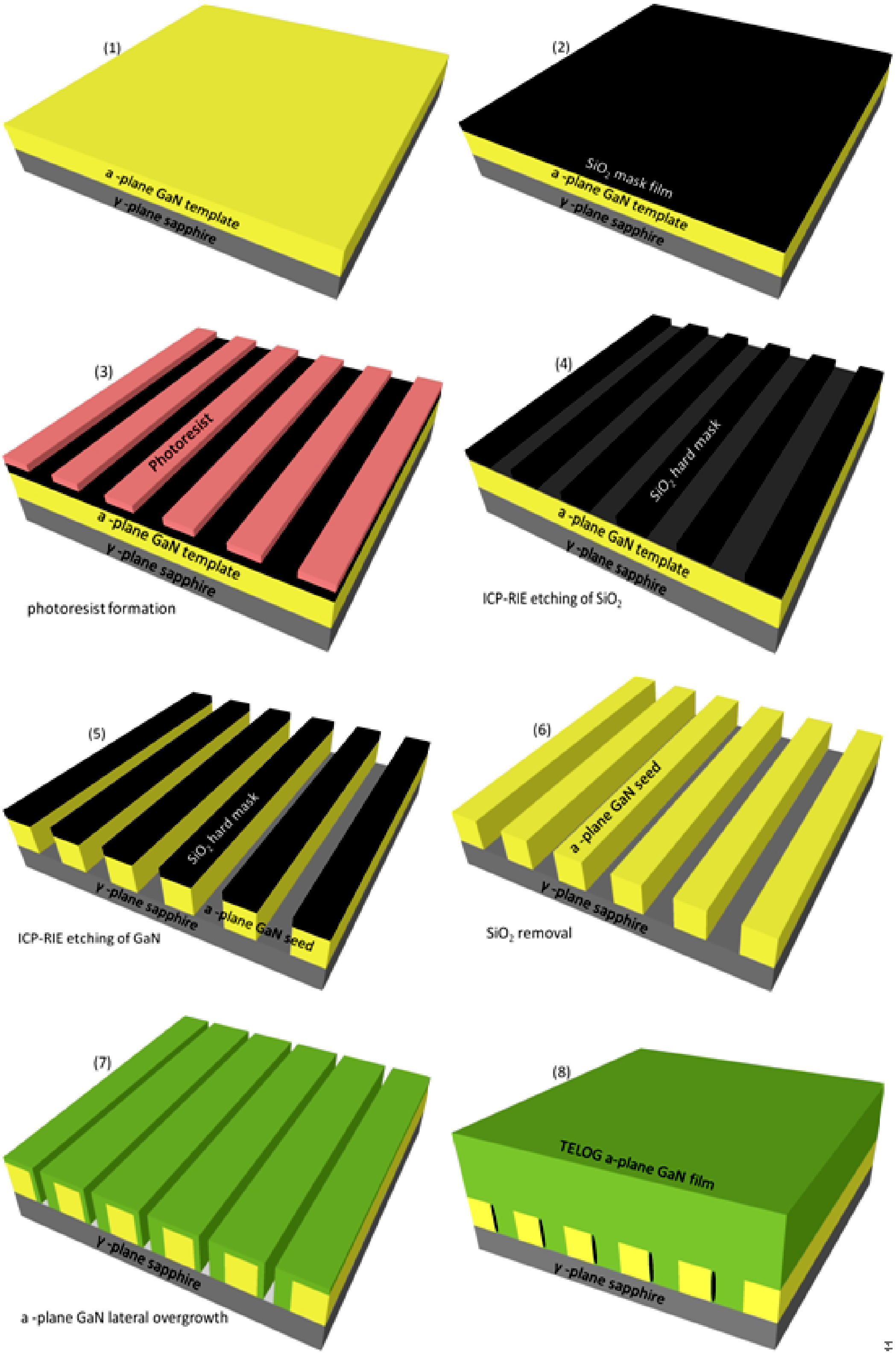

Figure 3.09. Schematics of TELOG *a*-plane GaN technique.

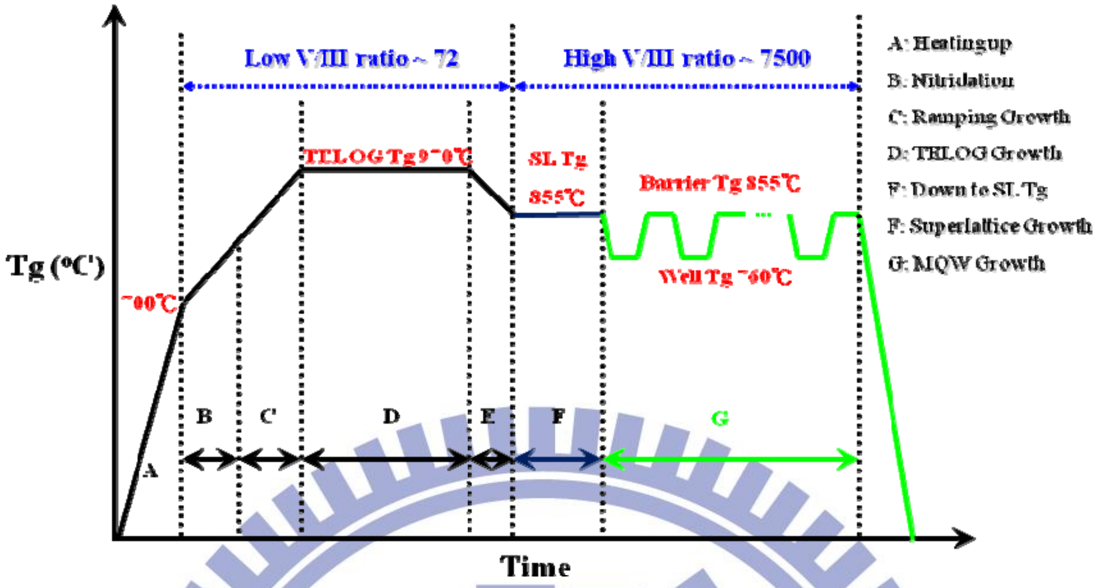

Figure 3.10. The MOCVD growth procedure for *a*-plane GaN by TELOG technique.

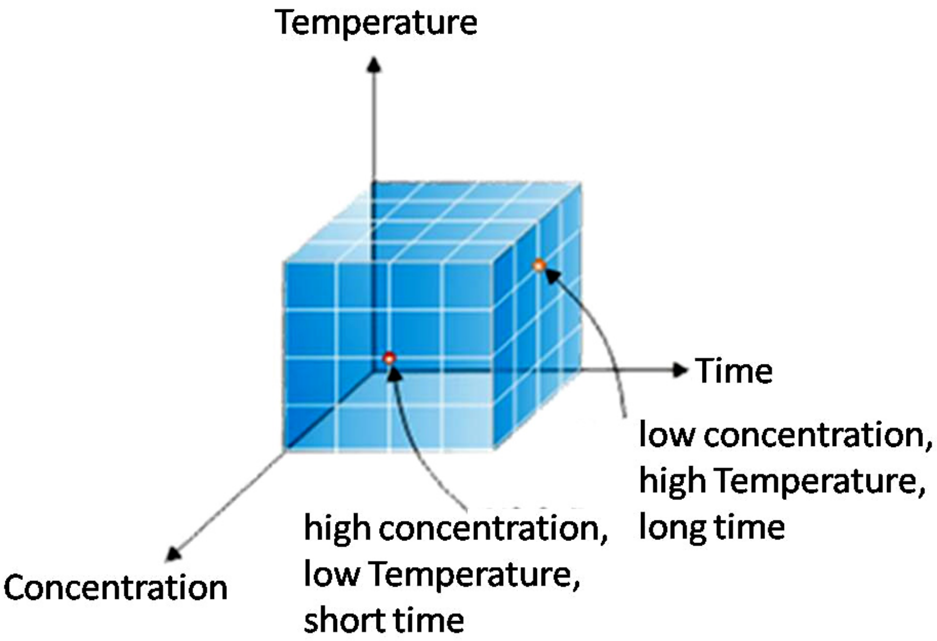

Figure 3.11. Conditions of KOH etching of TELOG *a*-plane GaN and InGaN/GaN MQWs.

Chapter 4

Result I – Nonpolar *a*-Plane GaN on Patterned m-Plane Sapphire

4.1 The Epitaxial Mode and Morphology under Different Level of V/III Ratio

Te artificially-etched exposed symmetric *c*-plane vertical sidewalls and *m*-plane terraces of sapphire (as in figure 3.07) during MOCVD growth resulted in two kinds of GaN crystallites; each of the crystallite has unique growth orientation and terminal planes and outlines. First, on-axis XRD scans figure 4.01 indicated that pure *a*-plane GaN was carried out under the V/III ratio of 9000, 1800, and 350. Figure 4.02 ~4.04 showed that the selective area epitaxy of *c*-plane GaN was grown laterally only from the artificially-etched *c*-plane sapphire sidewalls. On the contrary, deposition of GaN was completely absent on the *m*-plane terraces. It's confirmed[4.01] experimentally that the crystallographic orientation relationships of GaN epitaxial stripes grown from c plane sidewalls of trench-patterned *m*-plane sapphire are $(11\text{-}20)_{GaN} \parallel (10\text{-}10)_{sapphire}$, $[0001]_{GaN} \parallel [0001]_{sapphire}$, and $[10\text{-}10]_{GaN} \parallel [11\text{-}20]_{sapphire}$.

The SEM images in figure 4.05~4.07 show clearly the representative cross-sectional morphology of GaN stripes selectively grown on trench-patterned *m*-plane sapphire. The shapes of GaN stripes were a strong function of the V/III ratio. Figure 4.05 shows the sample carried out with a V/III ratio of 9000 for 30 min. GaN grew from the *c*-plane trench sidewalls only with faster growth rate along +*c*-direction than that in *a*-direction, and therefore the upward planes are inclined by 58.5° with respect to the trench sidewalls. Additionally, the upwardly inclined plane was tentatively attributed to (11-22) planes, since the growth front was constructed by the competition between +*c*-planes and *a*-planes of GaN.

Figure 4.06 revealed that when the V/III ratio was decreased to 1800, the growth mode is similar to that with a V/III ratio 9000 for 30 min. The reduction of V/III ratio led to a more conspicuous increase of growth rate in both +*c* and *a* direction of GaN which leads to the coalescent tip and level-raising respectively. As a matter of fact, the upwardly inclined (11-22) planes are maintained.

Next, a different growth mode was presented under a still lower V/III ratio, *i.e.* 350, with the same growth time. As in figure 4.07, the growth along the +*c* direction advanced overwhelmingly faster than that in *a* direction and was stymied by itself while these planes coalescence in +*c* direction. This formed the upwardly flat *a*-plane. Something must be mentioned that the growth along the -*c* direction was almost stationary, no matter how much the V/III ratio vary, from 9000 to 350. Furthermore, the growth on the (10-10) sapphire terraces has been completely forbidden.

The schematic depictions of the shape of GaN stripes under different growth V/III ratio 9000, 1800 and 350 were in figure 4.08 ~ 4.10. As in these figures, the blue-color region are grown GaN. It depicts out that the lower III-V ratio leads to higher growth rate of +*c*-direction and suppresses the revelation of *a*-planes. In figure 4.10, the slow growth rate of GaN –*c*-direction is also depicted.

Figure 4.11 showed the dramatically-altered growth mode and crystal orientations by decreasing the value of V/III ratio to 72. The GaN grown laterally (from *c*-plane sidewalls) and vertically (from *m*-plane terraces) were obtained simultaneously which revealed in figure 4.12. The GaN stripes grown from *c*-plane sapphire sidewalls performed similar behavior with that at V/III ratio of 350, but it played another role as the mask for the epitaxial lateral overgrowth (ELO) of GaN on the *m*-plane sapphire terraces. These well-defined in-situ-forming GaN-masks in [11-20]$_{\text{sapphire}}$ direction suppressing the growth of (10-11) GaN on *m*-plane sapphire terraces and leading to pure growth of (11-22) GaN, and the in-plane epitaxial relationships of (11-22) GaN on *m*-plane terraces are (11-22)$_{\text{GaN}}$ || (10-10)$_{\text{sapphire}}$, [10-10]$_{\text{GaN}}$ || [1-210]$_{\text{sapphire}}$, and [1-21-1]$_{\text{GaN}}$ || [0001]$_{\text{sapphire}}$[4.01]. It's worth noting that the gradual growth of lateral-GaN limited the epitaxial lateral overgrowth of (11-22) GaN. As a result, the (11-22) GaN shows no noticeable wing-region over the lateral-GaN but it contains 32° inclined +*c*-planes with respect to the upwardly flat (11-22) plane.

4.2 Defects Distribution and Clarification

Figure 4.13 shows the STEM image of GaN under a V/III ratio of 72 on a lower terrace/trench width ratio (2μm/4μm) substrate. The growth mode is equivalent to that of higher terrace/trench width ratio (*i.e.* 4μm/2μm); meanwhile, the stacking faults were localized in the GaN grown from the *m*-plane terraces. The orientation of stacking faults in the GaN on the *m*-plane terraces, completely parallel to the inclined (0001) GaN planes, are in close correlation with its growth rate along the +*c*-direction, which advances overwhelmingly faster than that in *a*-direction.

In figure 4.14, the bright field cross-sectional TEM image shows the distribution of stacking faults and threading dislocations in (11-22) GaN on *m*-plane terraces and epitaxial lateral overgrowth (11-22) GaN, respectively. By correlating the growth mechanism in section 4.1 for the V/III ratio of 72 with the transmission electron microscopy observations, the reasons of defects formation are attributed to atomic-rearrangement-related deposition and strain.

The stacking faults in (11-22) GaN on *m*-plane sapphire terraces are caused by the growth front which advances too fast to completely fill each atomic layer parallel to (0001) plane of GaN, and thus leads to a series of stacking faults parallel to each other in (0001) plane. Figure 4.15 and figure 4.16 show the dark field cross-sectional TEM images with different *g* vectors. The visibility of specific type of stacking faults is different under these two kinds of *g* vector. However, it needs more careful experiments and observations to determine the type of stacking faults exactly.

The epitaxial lateral overgrowth (11-22) GaN region in figure 4.14 showed some threading dislocations started from the local region near the corner-edge of *m*-plane terraces and penetrated directly through the (11-22) GaN bulk layer to the surface. The distribution of these threading dislocations did not spread far into the (11-22) GaN bulk layer in [0001] direction. In this observation, we concluded here that the strain field introduced by the interaction the epitaxial lateral overgrowth (ELO) of GaN stripes from *c*-plane sapphire sidewalls and the epitaxial growth of GaN on the *m*-plane sapphire terraces. Fortunately, the slow growth rate of epitaxial lateral overgrowth of GaN along –*c*-direction prevented the distribution of threading dislocations extending into the lateral overgrowth region. Here the slow growth rate can be regarded as smaller interaction forces between ELO-GaN and GaN stripes from *c*-plane sapphire and led to the confined strain field.

Figure 4.17 depicted out the cross-sectional cathodoluminescence image of the epitaxial lateral overgrowth (ELO) of GaN stripes from *c*-plane sapphire sidewalls. By correlating the mechanism of cathodoluminescence spectroscopy and the crystalline quality, the bright, clear light region represents the high crystalline quality of epitaxial lateral overgrowth region of GaN. Obviously, the infinitesimal region which contained threading dislocations and stacking faults do almost no effect on the crystalline quality of lateral overgrowth region of GaN.

Apparently, the narrower terraces did effectively restrain the volume of semipolar (11-22) GaN growing from *m*-plane sapphire terraces; however, the growth of (11-22) GaN cannot be eliminated by decreasing width of *m*-plane terraces. To summarize, the growth mode of GaN on trench-patterned m-plane sapphire is strongly depends on the V/III ratio during MOCVD growth rather than the terrace/trench width ratio of the patterned substrate.

4.3 Summary

In this chapter the growth mechanism and epitaxial mode of *a*-plane GaN on trench-patterned *m*-plane sapphire by MOCVD under different V/III ratio was demonstrated. For V/III ratio from 350 up to 9000, the epitaxial lateral growth of GaN from the +*c*-plane sidewalls and forming high crystalline quality *a*-plane GaN is dominated. Under low level V/III ratio of 72, the growth of lateral-GaN accompanied the aroused (11-22) GaN on *m*-plane sapphire terraces. This unexpected appearance of semipoalr (11-22) GaN can be suppressed by optimizing the V/III ratio. On the other hand, lower terrace/trench width ratio doesn’t interdict it. By optimizing the level of V/III ratio during MOCVD growth and appropriate terrace/trench width ratio of patterned *m*-plane sapphire substrate, we expect that a high crystalline quality nonpolar *a*-plane GaN epilayer on *m*-plane sapphire is achievable.

4.4 References

[4.01] X. Ni, *et al*. Appl. Phys. Lett.**90**, (2007) 182109.

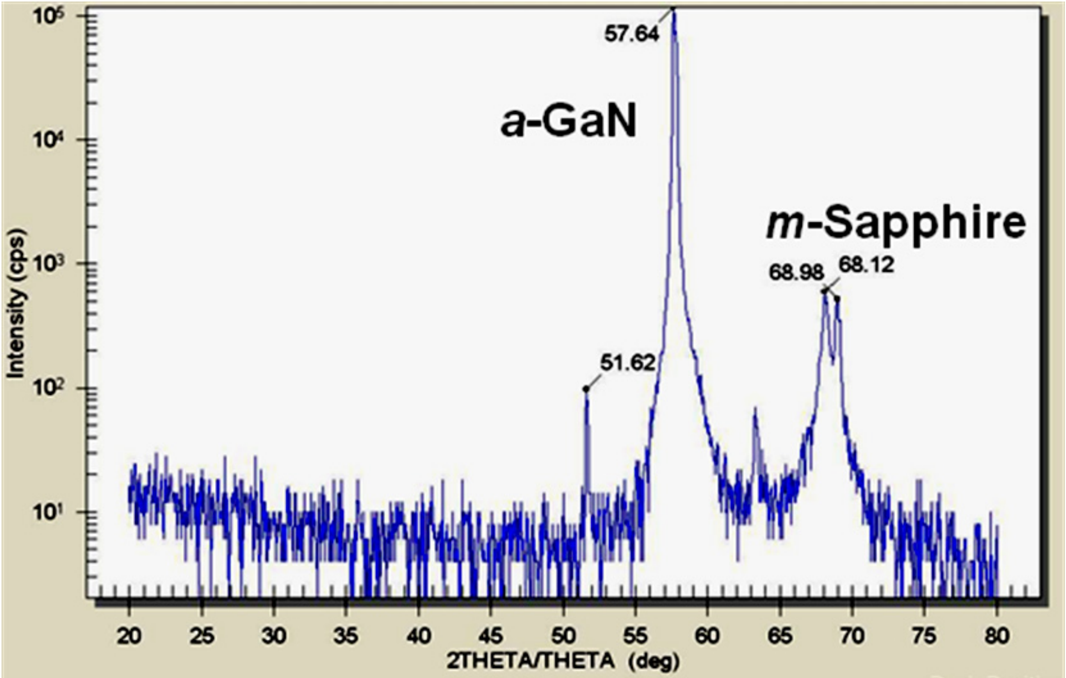

Figure 4.01. XRD θ-2θ spectrum of *a*-plane epitaxy on trench-patterned *m*-plane sapphire.

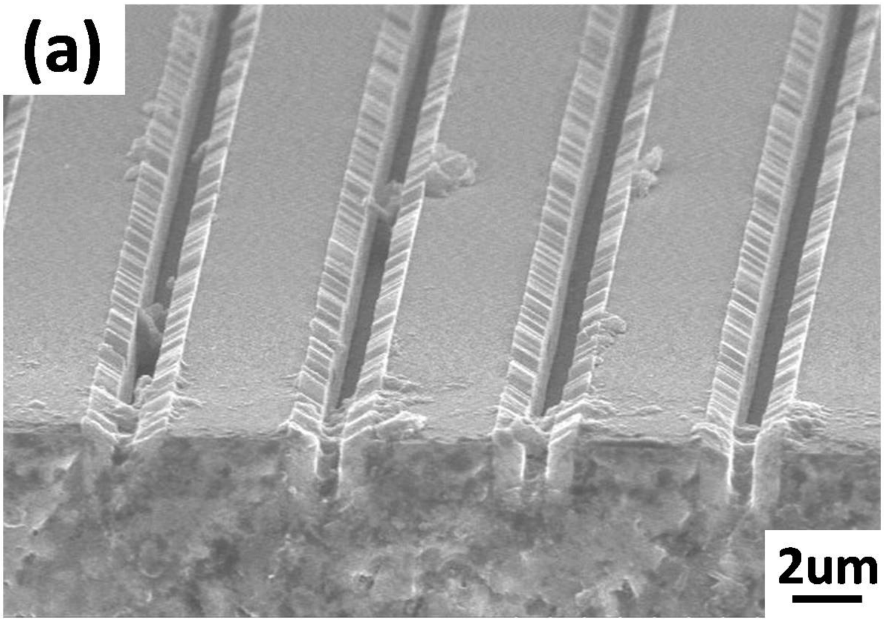

Figure 4.02. The SEM images of *a*-plane GaN grown by MOCVD on trench-patterned *m*-plane sapphire under the V/III ratio of 9000.

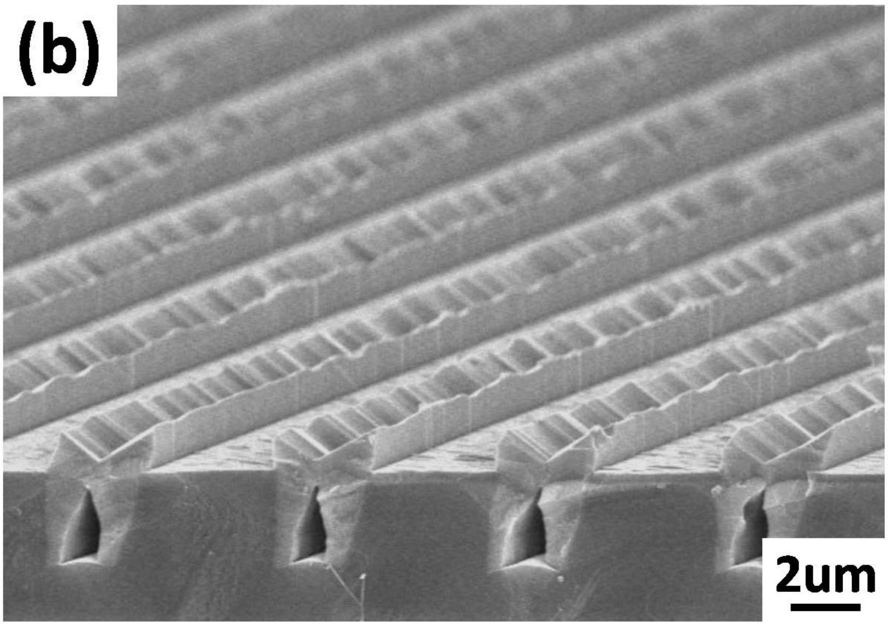

Figure 4.03. The SEM images of *a*-plane GaN grown by MOCVD on trench-patterned *m*-plane sapphire under the V/III ratio of 1800.

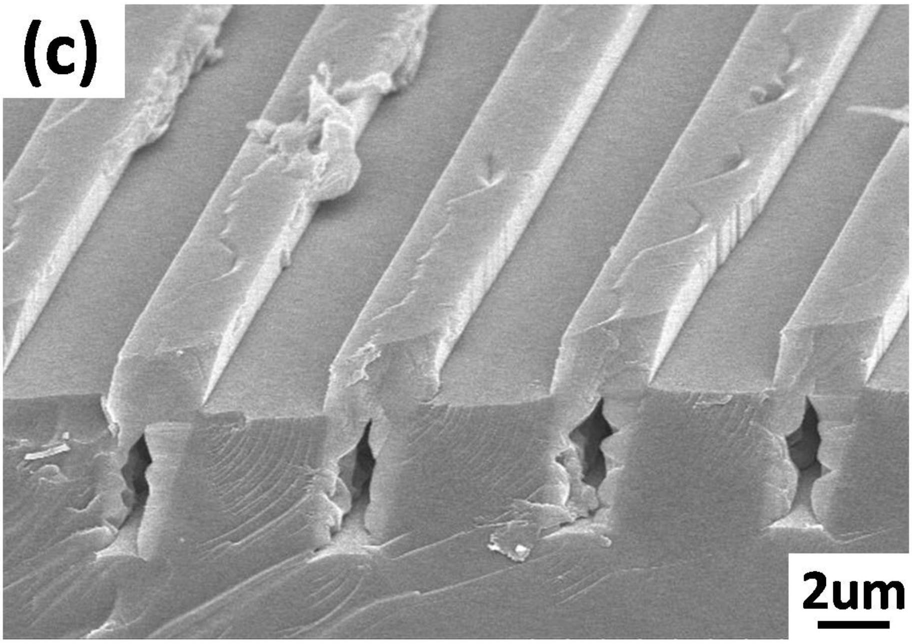

Figure 4.04. The SEM images of *a*-plane GaN grown by MOCVD on trench-patterned *m*-plane sapphire under the V/III ratio of 350.

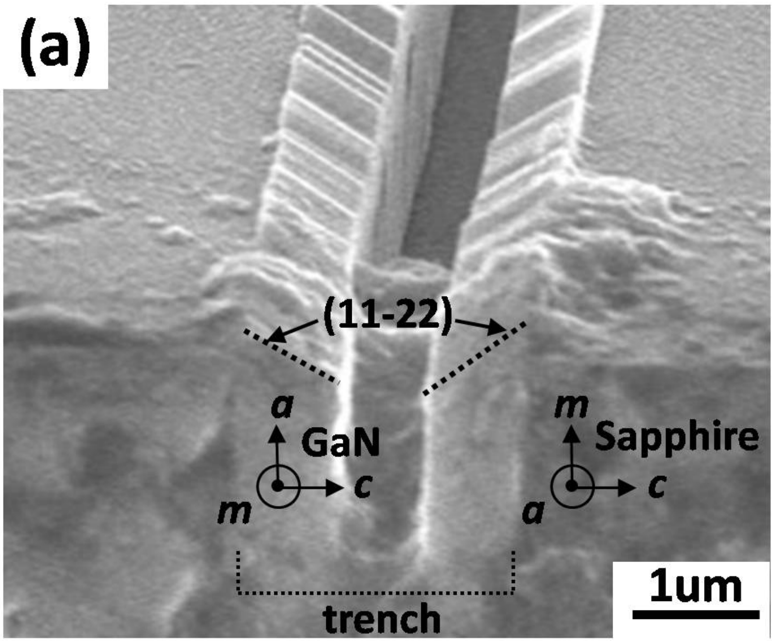

Figure 4.05. The SEM images *a*-plane GaN grown by MOCVD on trench-patterned *m*-plane sapphire under the V/III ratio of 9000. The corresponding crystal planes and orientations are depicted.

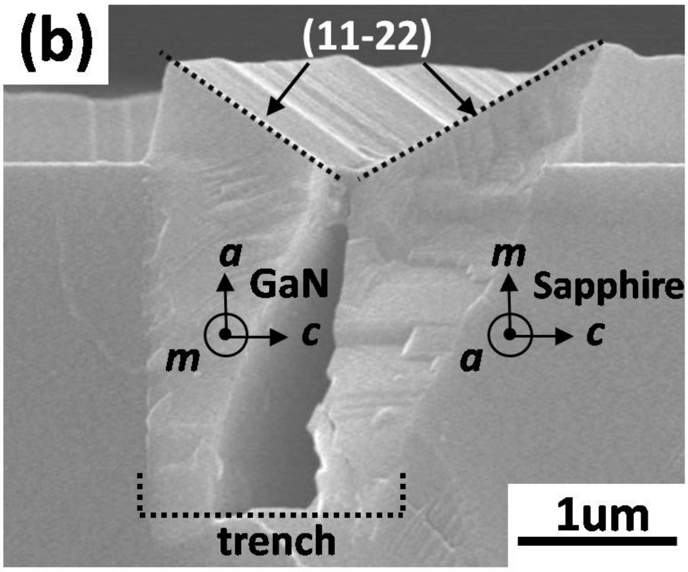

Figure 4.06. The SEM images of *a*-plane GaN grown by MOCVD on trench-patterned *m*-plane sapphire under the V/III ratio of 1800. The corresponding crystal planes and orientations are depicted.

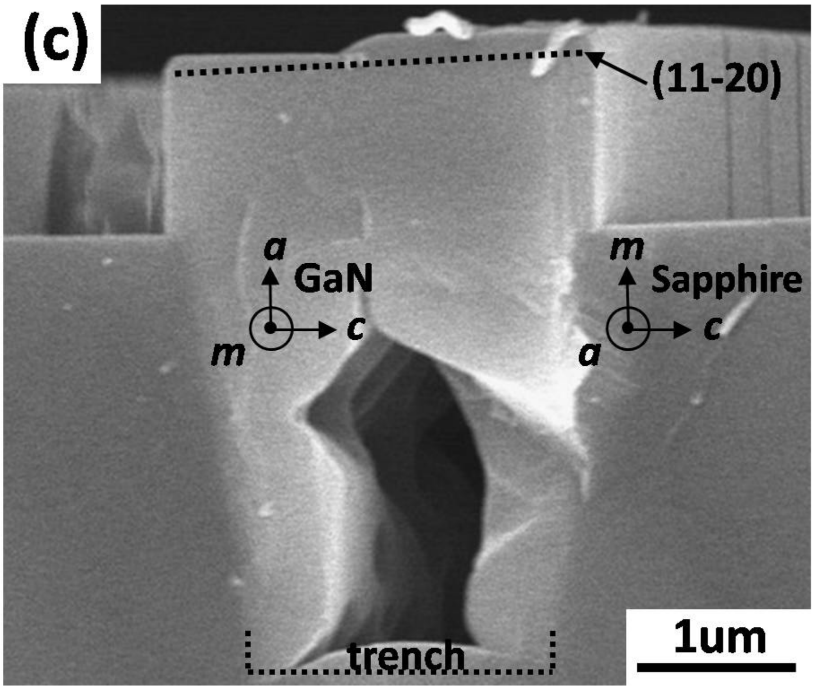

Figure 4.07. The SEM images of *a*-plane GaN grown by MOCVD on trench-patterned *m*-plane sapphire under the V/III ratio of 350. The corresponding crystal planes and orientations are depicted.

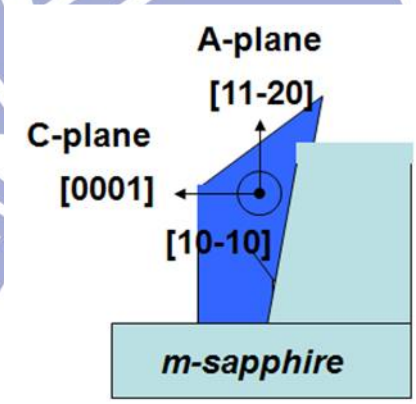

Figure 4.08. Schematics of the epitaxial mode of *a*-plane GaN on *m*-plane sapphire under the V/III ratio of 9000 by MOCVD.

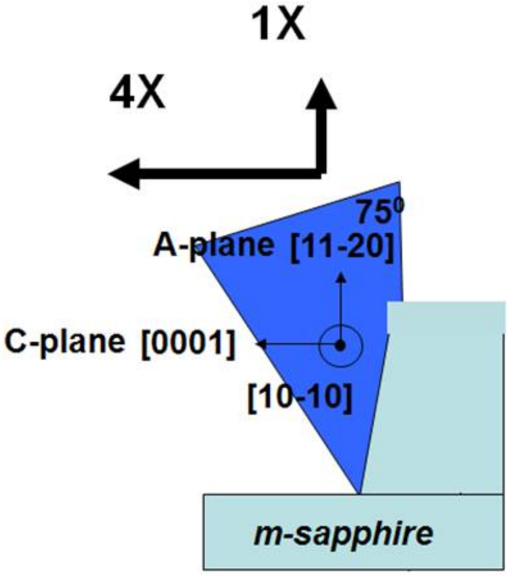

Figure 4.09. Schematics of the epitaxial mode of *a*-plane GaN on *m*-plane sapphire under the V/III ratio of 1800 by MOCVD.

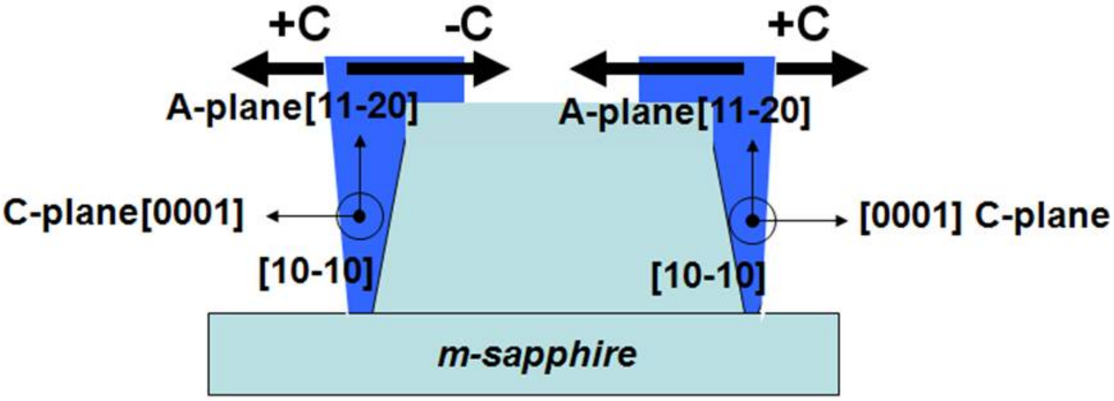

Figure 4.10. Schematics of the epitaxial mode of *a*-plane GaN on *m*-plane sapphire under the V/III ratio of 350 by MOCVD.

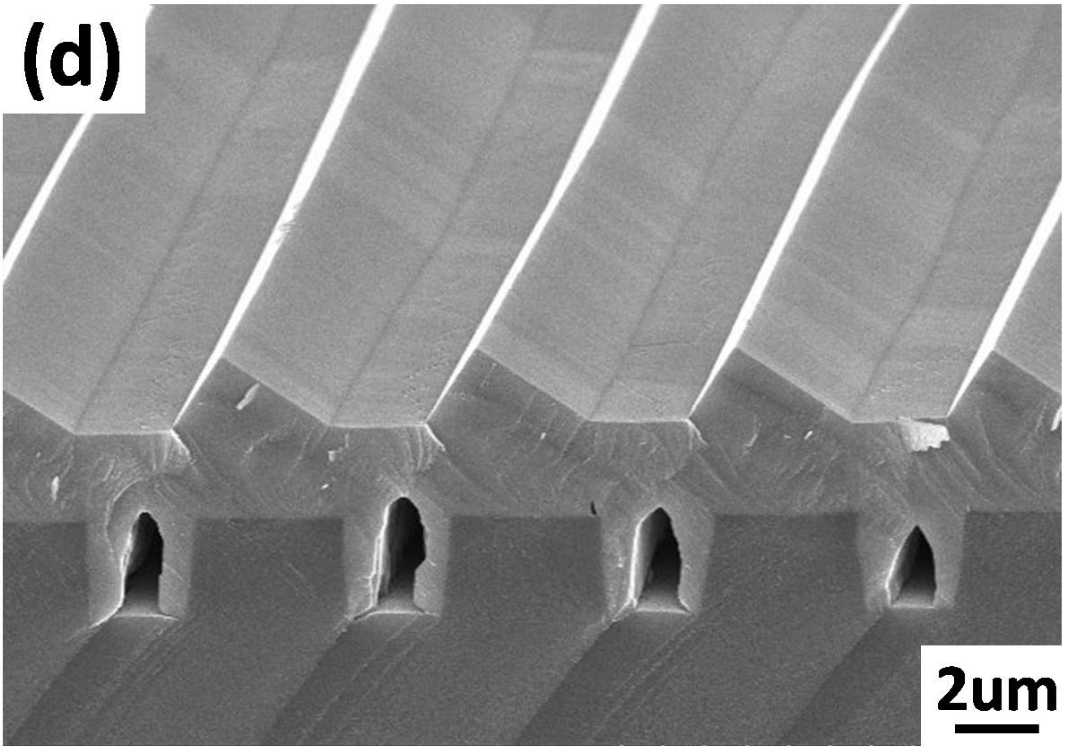

Figure 4.11. The SEM images of *a*-plane GaN grown by MOCVD on trench-patterned *m*-plane sapphire under the V/III ratio of 72.

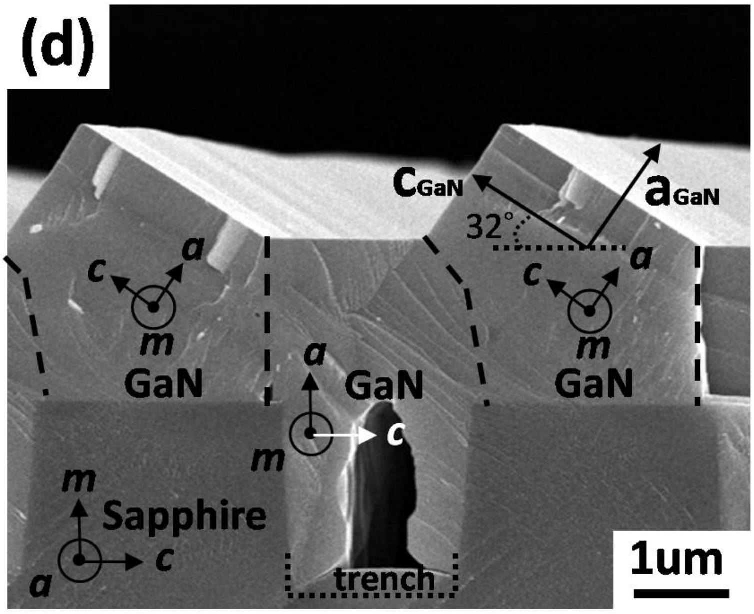

Figure 4.12. The SEM images of *a*-plane GaN grown by MOCVD on trench-patterned *m*-plane sapphire under the V/III ratio of 72. The corresponding crystal planes and orientations are depicted.

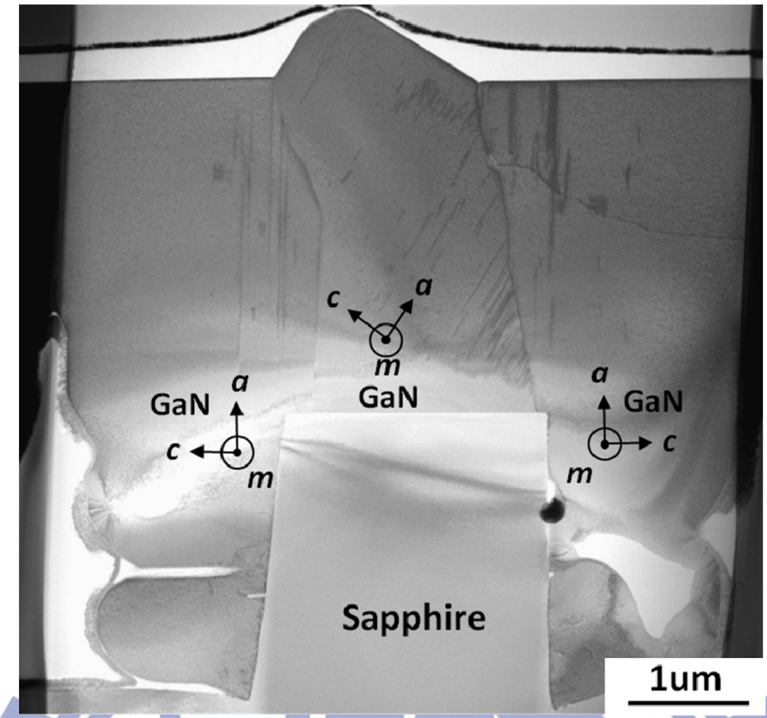

Figure 4.13. The cross-sectional TEM image of GaN grown by MOCVD under the V/III ratio of 72 with terrace/trench width 2μm/4μm. The corresponding crystal planes and orientations are depicted.

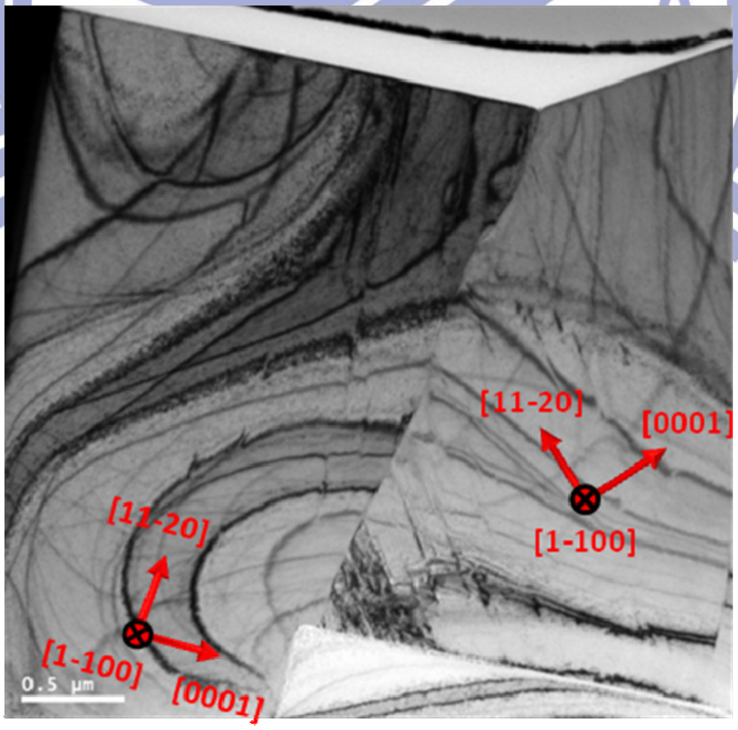

Figure 4.14. The cross-sectional TEM image of GaN grown by MOCVD under the V/III ratio of 72 with terrace/trench width 2μm/4μm. The corresponding crystal planes, orientations and defects distribution are depicted.

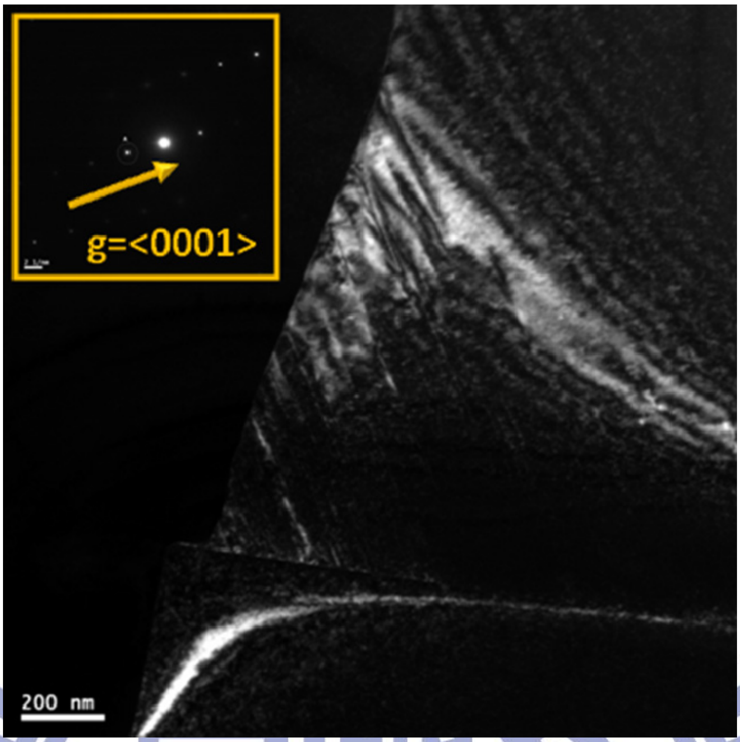

Figure 4.15. The cross-sectional TEM image of GaN grown by MOCVD under the V/III ratio of 72 with terrace/trench width 2μm/4μm. The corresponding *g* vector is along [0001] direction.

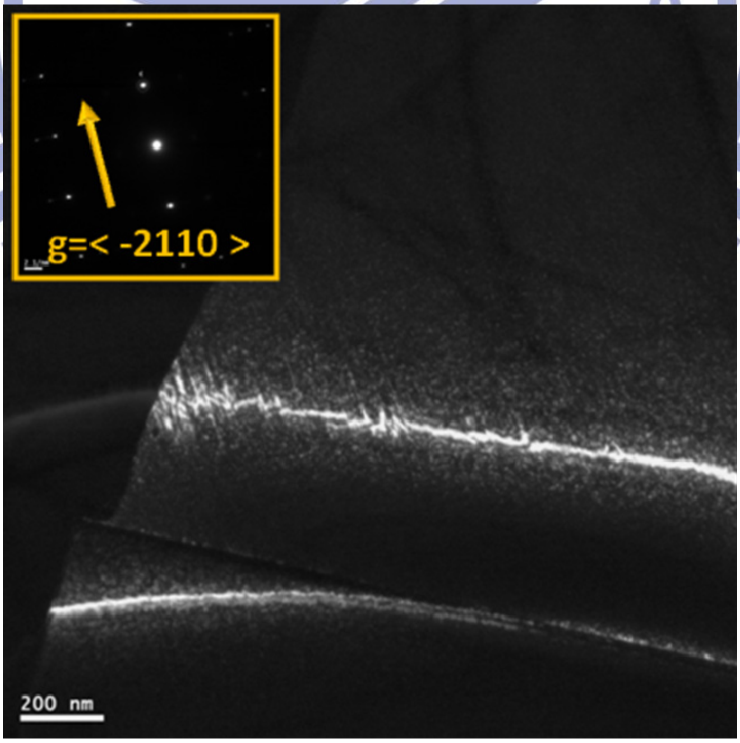

Figure 4.16. The cross-sectional TEM image of GaN grown by MOCVD under the V/III ratio of 72 with terrace/trench width 2μm/4μm. The corresponding *g* vector is along [-2110] direction.

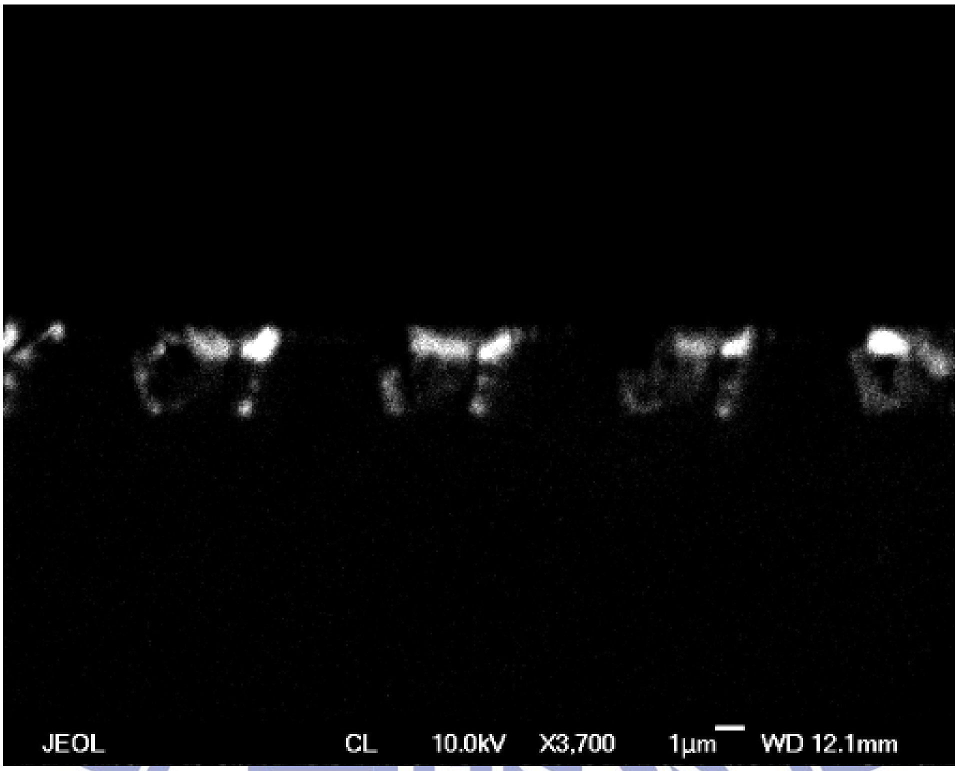

Figure 4.17. The CL images of *a*-plane GaN grown by MOCVD on trench-patterned *m*-plane sapphire under the V/III ratio of 1800.

Chapter 5

Result II –Trenched epitaxial lateral overgrowth (TELOG) *a*-Plane GaN LED on *γ*-Plane Sapphire

5.1 The Epitaxial Mode and Morphology

The preparation process flow of the patterned *a*-plane GaN template on *γ*-plane sapphire for high crystalline quality TELOG *a*-plane GaN is shown in Figure 3.09. While the stripe-patterned *a*-plane template GaN was ready for further regrowth, growth with MOCVD under different level of V/III ratio was introduced in order to achieve the smooth coalescence surface.

Under the suggestion from the experiments and results in Chapter 4, we got the possible optimal growth conditions of *a*-plane GaN grown on *γ*-plane sapphire, *i.e.* the lower V/III ratio which leads the faster advancing rate of the growth front in *c*-direction. To observe the growth mechanism in detail, the MOCVD regrowth was stopped before the complete coalescence of the *a*-plane GaN films. The SEM images of cross-sectional TELOG *a*-plane GaN by MOCVD under different level of V/III ratio and at different growth time were shown in figure 5.01~ 5.03. In Figure 5.01 and 5.02, the MOCVD regrowth conditions were controlled at V/III ratio of 500, 980°C, 30 minutes and 120 minutes respectively. Under such conditions, the advancing rate of the growth front in *a*-direction is comparable to that of +*c*-direction while the advancing rate of the growth front in –*c*-direction is scarcely comparable to them. The characterization of advancing rate of each direction can be done by dividing the length extending out of the seed-region by growth time, i.e. 30 minutes in figure 5.01. The divergence of these growth rates seems quite indifferent to the final morphology, however, as to the longer growth time, the unexpected outcome shows.

Figure 5.02 depicts out the unexpected deep-extending coalescence boundary and accompanies the stripe-like voids at the end of the coalescence boundary on the terminal surface. These defects do actually affect the further epitaxial growth of *n*-GaN, superlattices, MQWs, and *p*-GaN and lead to unrecoverable results. Thus the growth condition was tuned to a lower level of V/III to achieve a completely coalescence GaN with smooth terminal surfaces.

The regrowth result is shown in figure 5.03, where the epitaxial lateral growth GaN was completely coalescence and performed a perfect thickness without deep-extended boundaries and stripe-like voids. The formation of the stick-like shaped voids is due to the fast advancing rate of +*c*-direction of GaN and the quickly shrinking of the space between that growth front and the original seed-wall. The small crevice prevents the sources of MOCVD from diffusing into the void the thus leaves it at the bottom of the thick GaN epitaxial layer. The dimension of the residual voids are approximately 3μm in height and 300~400nm in width. These stick-like shaped voids showed no tremendous to the optical properties enhancement for its small dimension in width and far away from the position of the MWQs. However, the size of these voids is large enough to allow the chemical solution to penetrate deeply into it and perform some specific etching effects and enhancement to the optical properties of the MQWs. The related results are provided in chapter 6 here of this thesis.

Additionally, the morphology of the terminal surface of the TELOG *a*-plane GaN revealed some information about the growth mode, crystalline quality and most of all, the defects distribution. As can be seen in figure 5.04, terminal surface of the seed region are much rougher than that of the wing region. The differences of roughness lead the contrast of the surface image which does a great help in distinguishing the pattern direction after the completely coalescence regrowth.

By correlating the transmission electron microscopy observations with the terminal surface morphology, the distribution of dislocations explains the relationship. In figure 5.05, the dislocations are initiated from the seed region, the original *a*-plane GaN template on *γ*-plane sapphire, and extended upward toward the terminal surface. This would be the main cause of the formation of surface morphology in figure 5.04. The wing regions, in contrast, are almost free of dislocations and perform a perfect crystalline quality. The nature of epitaxial lateral growth of these regions leads to the smooth terminal surface and extremely low dislocation density.

The specific optical properties of the TELOG *a*-plane GaN and InGaN/GaN MQWs are seriously affected by the in-situ formed surface morphology characteristics. The corresponsive data and discussions are available in this chapter at section 5.3.

As for the coalescence behavior that cause the void in TELOG *a*-plane GaN, the defect here be named as “coalescence boundary” in figure 5.06 telling the complete story. The epitaxial lateral growth rates of GaN along +*c* and –*c* direction are fast and slow respectively, and lead to the wider wing region and a narrower one. The planes of each growth front met together and heal over the terminal surface. The slight difference of GaN rotation angle from c-plane sapphire sidewall cause the mismatch of lattice structure and forming the so called “coalescence boundary”. The coalescence boundary extends from the pinnacle of the voids and penetrates the GaN layer with the ends at the terminal surface. The existence of the coalescence boundary acts as the indication of the *+c*/*–c* polarity of the growth front and becomes an important index while the TELOG *a*-plane GaN was etched in KOH-ethylene glycol chemical solution. Moreover, the coalescence boundary, a relatively weak region, would play a special role in the whole KOH-ethylene glycol chemical solution etching process. The etching-selectivity performed a radical change under the existence of the boundary at specific temperature and KOH-concentration. The related discussion is available in chapter 6, section 6.3.

5.2 Crystalline Quality of TELOG *a*-Plane GaN and InGaN/GaN MQWs

The thorough understanding of the specific properties of nonpolar GaN is of great importance toward the full development of the territory. In this chapter, the crystalline quality of TELOG *a*-plane GaN and InGaN/GaN MQWs are discussed further via the way of investigation of XRD. A flashback here is that the threading dislocations exist in only the seed region rather than in the wing region. The correlated XRD data can reveal more information about the improvement of the crystalline quality quantatively.

Generally speaking, the threading dislocation density and basal stacking fault density in nonpolar *a*-plane GaN grown on *γ*-plane sapphire substrate are 3×10^{10}cm^{-2} and 3×10^{5}cm^{-1} respectively[5.01]. Threading dislocations play the role as nonradiative recombination centers in GaN material and restrict the internal quantum efficiency. Thus the improvement of the device performance is attributed to the essential reducing of the threading dislocation density. Here in figure 5.07 and 5.08, the crystal quality was characterized by the full-width at half maximum (FWHM) of X-ray ω-2θ curves. In the measurement of along *c*-axis, the X-ray ω-2θ curves show that the FWHM of as-grown *a*-plane GaN on γ-sapphire is 713 arcsec and decreases to the level of 464 arcsec for the TELOG *a*-plane GaN on patterned *a*-plane template. For the case that along *m*-axis, the FWHM value is decreasing dramatically from 1665 arcsec, the as-grown *a*-plane GaN on γ-sapphire, to a low level of 341 arcsec, the TELOG *a*-plane GaN on patterned *a*-plane template. It has been demonstrated that the FWHM of X-ray ω-2θ curves is close related to the defects density, especially the density of dislocations. As shown in 5.07 and 5.08, the crystal quality of *a*-plane GaN grown on patterned *a*-plane template via TELOG technique is obviously better than that grown on γ-plane sapphire directly. The crystalline quality of *a*-plane GaN epitaxial layer has been greatly improved by TELOG growth method and the threading dislocation density can be reduced effectively from 1×10^{10}cm^{-2} at seed region to 1×10^{8}cm^{-2} at wing region. These XRD results and explanations can be verified by figure 5.05, the TEM image of clear dislocation distribution of the seed and the wing region.

As for the characterization of crystalline quality *a*-plane InGaN/GaN MQWs on TELOG *a*-plane GaN epitaxial layer, the high resolution XRD (HRXRD) pattern along *c*-axis [0001] direction and *m*-axis [1-100] direction are introduced. In figure 5.09, along *c*-axis, and figure 5.10, along *m*-axis, a strongest peak located around 0 arcsec and satellite diffraction peaks are observed in each HRXRD pattern. The strongest peak in each HRXRD pattern is due to the GaN while the satellite peaks arise from the periodicity of the InGaN/GaN MQWs. The well-defined satellite peaks implies a coherent periodicity of the InGaN/GaN heterostructure and suggest the presence of abrupt interfaces of quantum-wells and barriers. In principle, the separation between the main peak (GaN) and the first-order satellite peak characterizes the average MQWs mismatch caused by tetragonal compressive deformation and leads to a determination of the indium molar fractions in the wells. The discussion of this part related to the indium contents and the atomic construction of the MQWs will not go further for the focus of this section is the crystalline quality of TELOG *a*-pane GaN and the periodicity of InGaN/GaN MQWs.

5.3 Optical Properties of TELOG *a*-Plane GaN and InGaN/GaN MQWs

To make an investigation of the optical properties of TELOG *a*-plane GaN and the InGaN/GaN MQWs at different wavelength, a cathodoluminescence (CL) microscopy is used. The CL images maps the top surface of the TELOG *a*-plane GaN at specific emission wavelength, the GaN and blue MQWs. Figure 5.11 shows the CL mapping image of the TELOG *a*-plane sample around the emission wavelength of GaN (3.35eV) together with the SEM image of that sample at a bird eyes' view. The corresponding seed and wing regions are depicted in the figure. As can be seen that the wing region are full of the bright spots which caused by the CL emission at the wavelength of GaN. However, under the same stimulation conditions, the seed regions are almost free of CL emission phenomena. The main cause of the inhomogeneity of

CL emission phenomena has been discussed in section 5.2 and figure 5.05, where indicated that the seed region are full of quantities of threading dislocations and a dislocation-free wing region. These threading dislocations act as the nonradiative center and form the near-band-edge emission [5.02] which dominates the luminescence phenomena at seed region. One thing worth noting is that the extremely strong emission intensity located locally at the boundary of seed and wing was observed, as the distribution of brighter spots lined up into white lines. This can be attributed to the transition region of the surface morphology between the bumpy seed region and the smooth wing region. It caused extra light extraction locally and formed the bright stripes. Additionally, the boundary of crystalline quality transition from seed region to wing region in the epitaxial bulk made some contributions to the phenomena expectedly, however the actual proportion of contribution of each transition regions needs more careful confirmation.

As for the cathodoluminescence emission of the TELOG *a*-plane InGaN/GaN MQWs, the excitation range was controlled around the emission wavelength of InGaN/GaN MQWs (2.80eV). Figure 5.12 shows the CL mapping image together with the SEM image of that sample at a bird eyes' view. Considering the above-mentioned dislocation-distribution-related effects, the guess of the totally suppressing of the blue (440nm) emission of the InGaN/GaN MQWs at seen region should be reasonable. This ratiocination based on the TEM images from figure 5.13~5.15. Figure 5.13 shows the terminal surface region of the *a*-plane sample including the InGaN/GaN MQWs. The structure of the MQWs at seed region is extremely bumpy and rough due to the dislocation-filled seed region, while the MQWs above the dislocation-free wing region are perfectly smooth. The magnified TEM images in figure 5.14 and 5.15 show the bumpy MQWs and smooth MQWs respectively. On the contrary, the CL mapping image of InGaN/GaN MQWs is comparatively brighter at the seed region and darker at the wing region. This is mainly caused by the bumpy terminal surface of the seed region which is in the vicinity of MQWs and providing the light-extraction enhancement. In other words, the bumpy surface acts as a compensation for the low emitting efficiency of imperfect MQWs. The MQWs above wing region can emit affirmatively under the excitation of electrons for its smooth and sharp MQWs boundaries, however the emitted light intensity extracted out of the surface are weaker than that of bumpy surface region. That is the cause of the opposite phenomena to general common ratiocination. In comparison, the relative lower contrast ratio between the seed and wing region of InGaN/GaN MQWs emission in figure 5.12 spells out the nature of weak emission of imperfect MQWs, meanwhile the relative higher contrast ratio between the seed and wing region of *a*-plane GaN represents the nature of strong emission of dislocation-free wing region, even the surface morphology had been taken into consideration.

To make a conclusion to the above-mentioned phenomena, figure 5.16 is suitable. In the spectrum of CL intensity versus the wavelength, the emission intensity around the wavelength of InGaN/GaN MQWs (2.80eV) is dominated by the seed region and that around the wavelength of GaN (3.35eV) is dominated by the wing region. The CL spectrum of the sample with electron excitation to the whole region including both the seed and wing shows exact matching peak positions to the individual ones.

5.4 Summary

To sum up, high crystalline quality and fully coalesced nonpolar *a*-plane GaN films at the thickness less than 10μm by using trenched epitaxial lateral overgrowth (TELOG) technique in MOCVD with a 3μm seed/3μm trench stripe pattern have been achieved. The +*c*-face of GaN could be much easily grown indicating that a narrower stripped GaN seeds and deeper trench etched into the surface of sapphire can derive a better quality *a*-plane TELOG GaN film for the most of the area, *i.e.* the larger wing region that cover over the surface. The length of growth period and the V/III ratio during MOCVD growth procedures are the pivotal points to achieve the fully coalesced terminal surface without the penetration of voids and imperfect boundaries to it.

The full widths at half maximum (FWHMs) of x-ray rocking curves along *c*-axis [0001] direction and *m*-axis [10-10] direction were reduced from 713 to 464 arcsec and from 1665 to 341 arcsec, respectively demonstrating the great improvement of the crystalline quality and the mitigation of the anisotropic in-plane strains between different crystal axes by TELOG.

According to the results of the cross-sectional transmission electron microscopy, the threading dislocation density in the epitaxial lateral grown wing region can be reduced largely from $1\times10^{10}cm^{-2}$ to $1\times10^{8}cm^{-2}$. It also depicted out the distribution of the dislocations clearly in the seed region rather than in the wing region and also showed the morphology of terminal surfaces above the seed and wing region. The growth structure of InGaN/GaN MQWs was observed at the same time, which is bumpy above the seed region and smooth above wing region. Meanwhile, the CL mapping showed the emission optical properties of nonpolar *a*-plane GaN and the InGaN/GaN MQWs on that. The seed and the wing region dominated the emission at wavelength around InGaN/GaN MQWs and GaN, respectively considering the emission nature of the material quality and the effects of surface textures.

The above-mentioned TELOG MOCVD technique for the growth of high crystalline quality *a*-plane GaN and InGaN/GaN MQWs provides a way toward the realm of nonpolar optoelectronics and be expected to overcome the efficiency green gap spectral range from 540~560 nm.

5.5 References

[5.01]M. D. Craven, S. H. Lim, F. Wu, J. S. Speck, and S. P. DenBaars, *Appl. Phys. Lett.* **81**, 469 (2002)

[5.02] Sung-Nam Lee et al, *Appl. Phys. Lett.*, **92**, 111106 (2008)

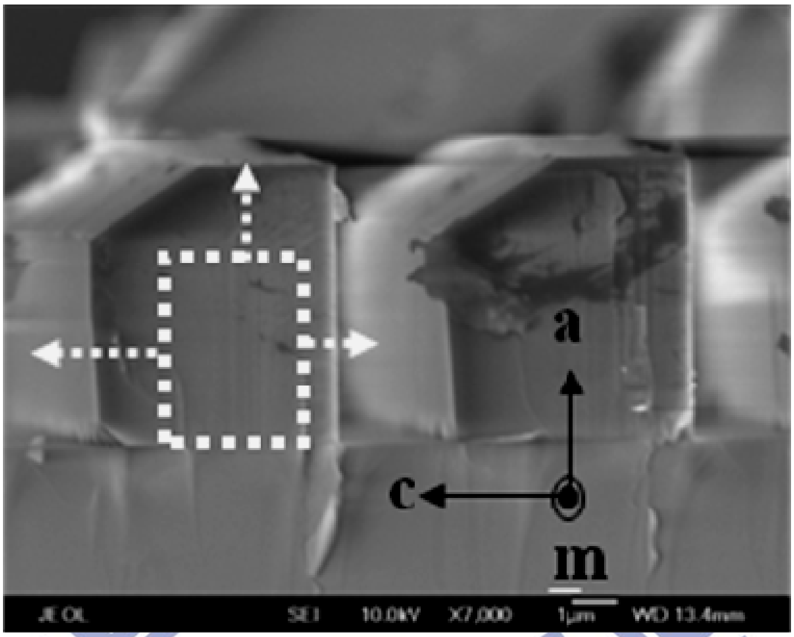

Figure 5.01. The SEM images of *a*-plane GaN grown by MOCVD using TELOG technique under the V/III ratio of 500 and 980°C. The corresponding crystal planes and orientations are depicted. Growth time is 30 min.

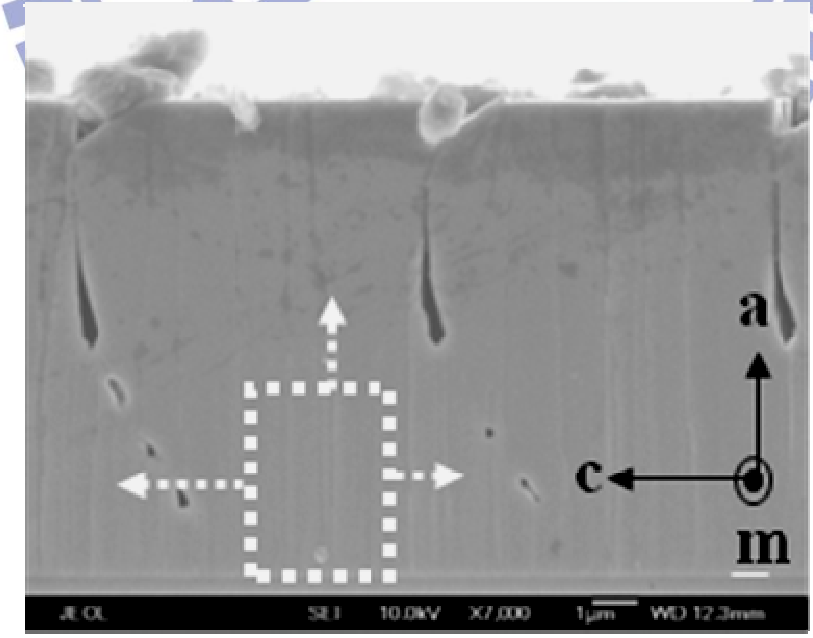

Figure 5.02. The SEM images of *a*-plane GaN grown by MOCVD using TELOG technique under the V/III ratio of 500 and 980°C. The corresponding crystal planes and orientations are depicted. Growth time is 120 min.

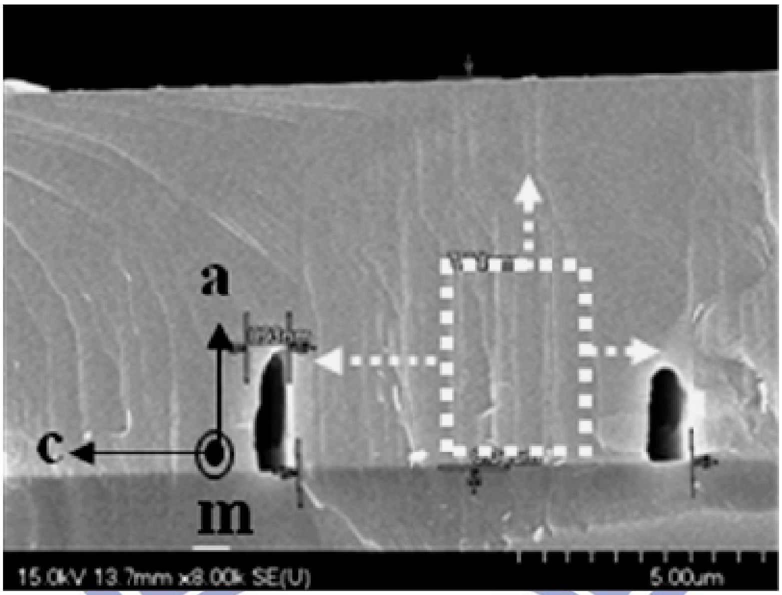

Figure 5.03. The SEM images of *a*-plane GaN grown by MOCVD using TELOG technique under the V/III ratio of 72 and 980°C. The corresponding crystal planes and orientations are depicted. Growth time is 120 min.

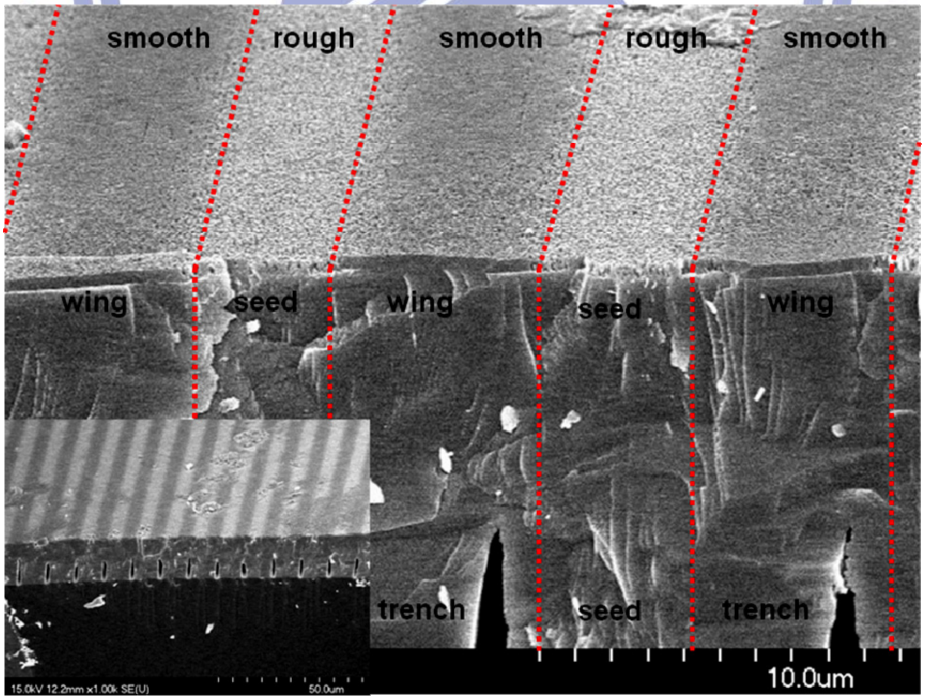

Figure 5.04. The SEM images of planar *a*-plane GaN grown by MOCVD using TELOG technique under the V/III ratio of 72 and 980°C. The corresponding seed region and the lateral wing region are depicted.

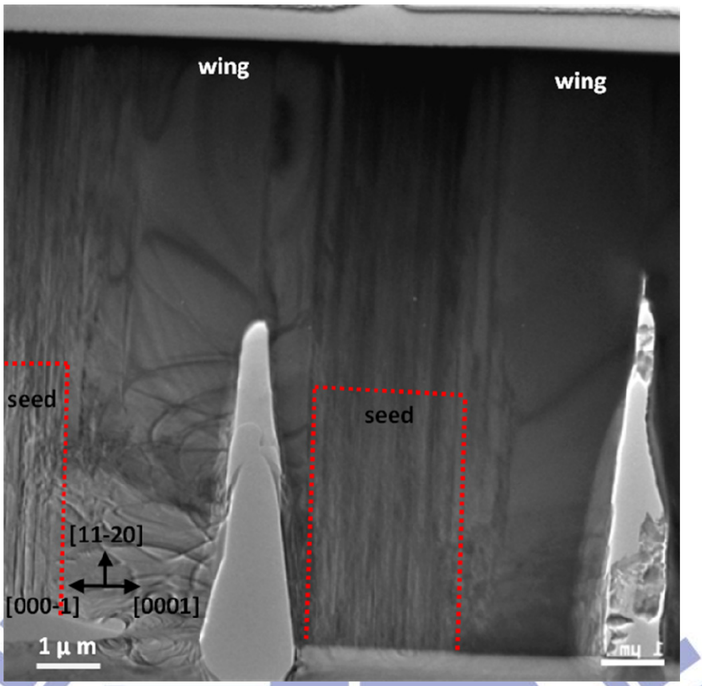

Figure 5.05. The TEM images of *a*-plane GaN grown by MOCVD using TELOG technique under the V/III ratio of 72 and 980°C. The corresponding seed region, lateral wing region and the distribution of dislocations are depicted.

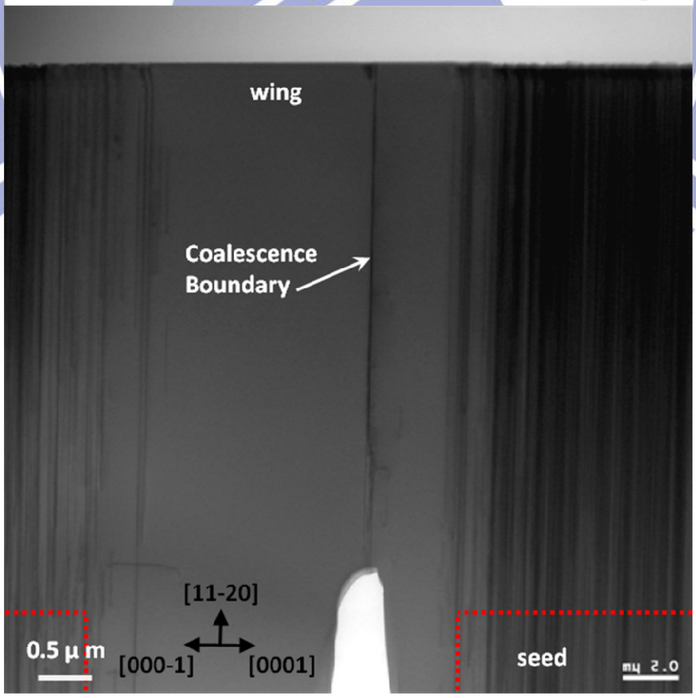

Figure 5.06. The TEM images of *a*-plane GaN grown by MOCVD using TELOG technique under the V/III ratio of 72 and 980°C. The corresponding coalescence boundary between +*c*-plane and –*c*-plane is depicted.

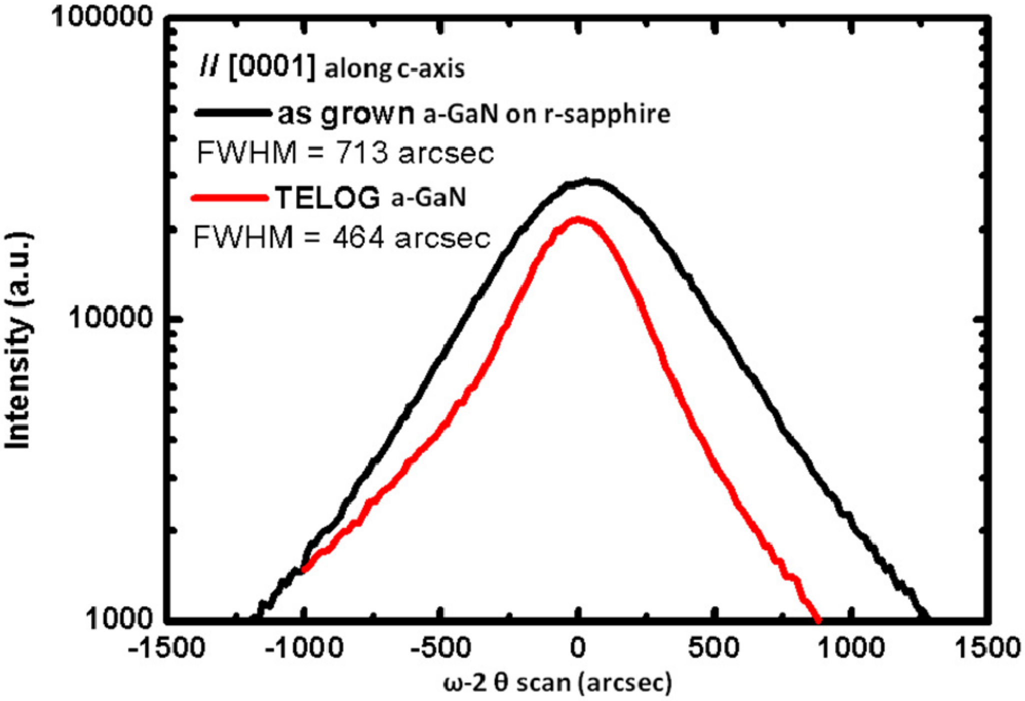

Figure 5.07. XRD *ω*-2*θ* spectrum along [0001] direction of *a*-plane GaN template and TELOG *a*-plane GaN on *γ*-plane sapphire.

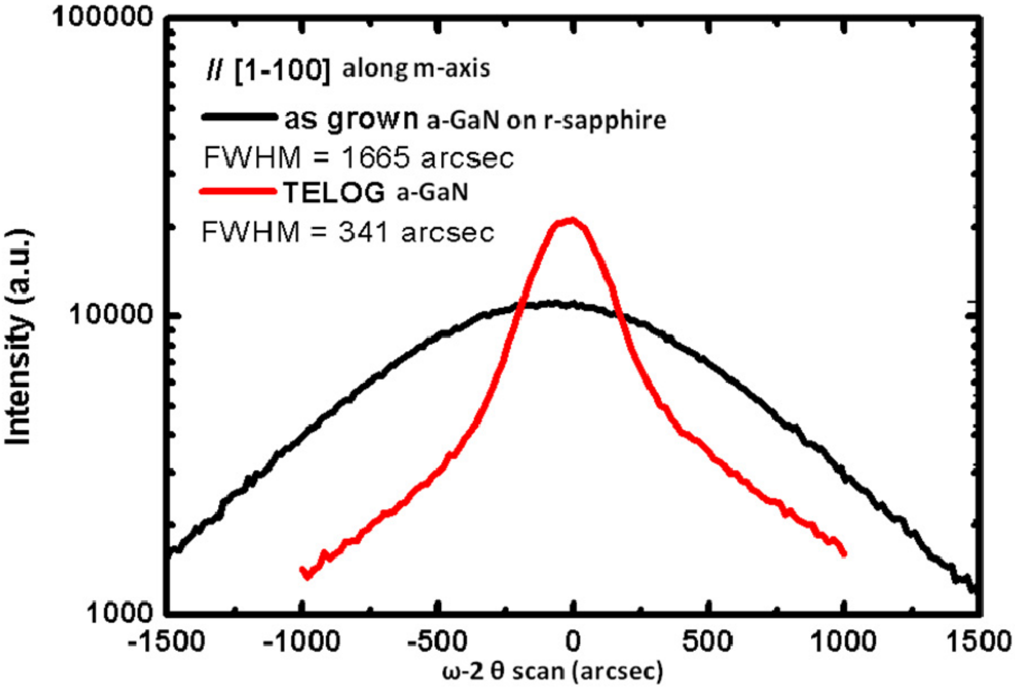

Figure 5.08. XRD *ω*-2*θ* spectrum along [1-100] direction of *a*-plane GaN template and TELOG *a*-plane GaN on *γ*-plane sapphire.

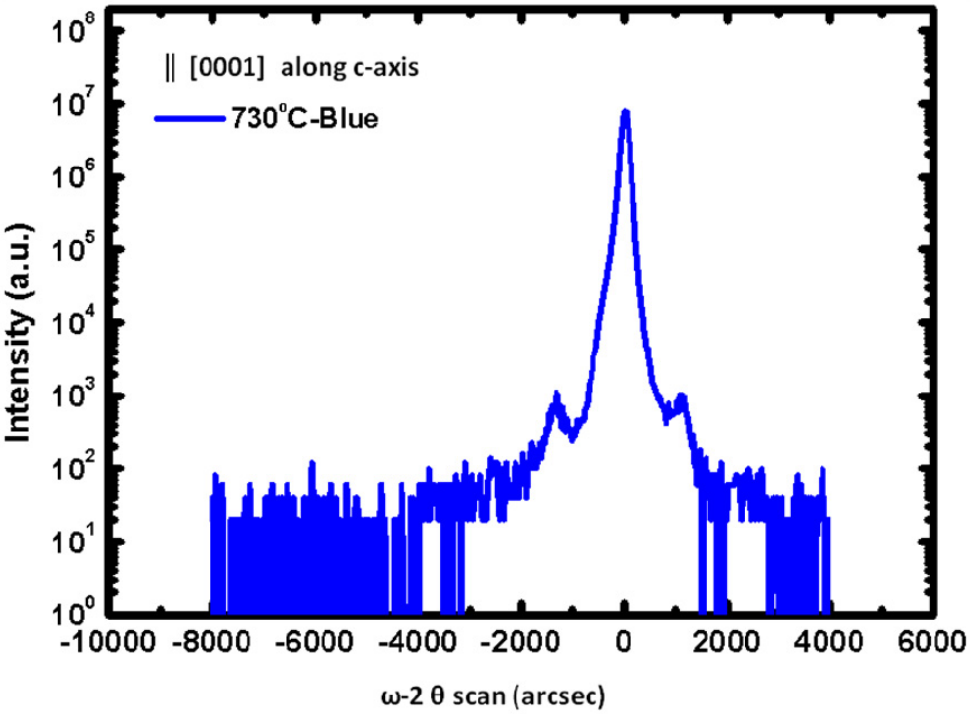

Figure 5.09. XRD ω-2θ spectrum along [0001] direction of TELOG *a*-plane InGaN/GaN MQWs on γ-plane sapphire.

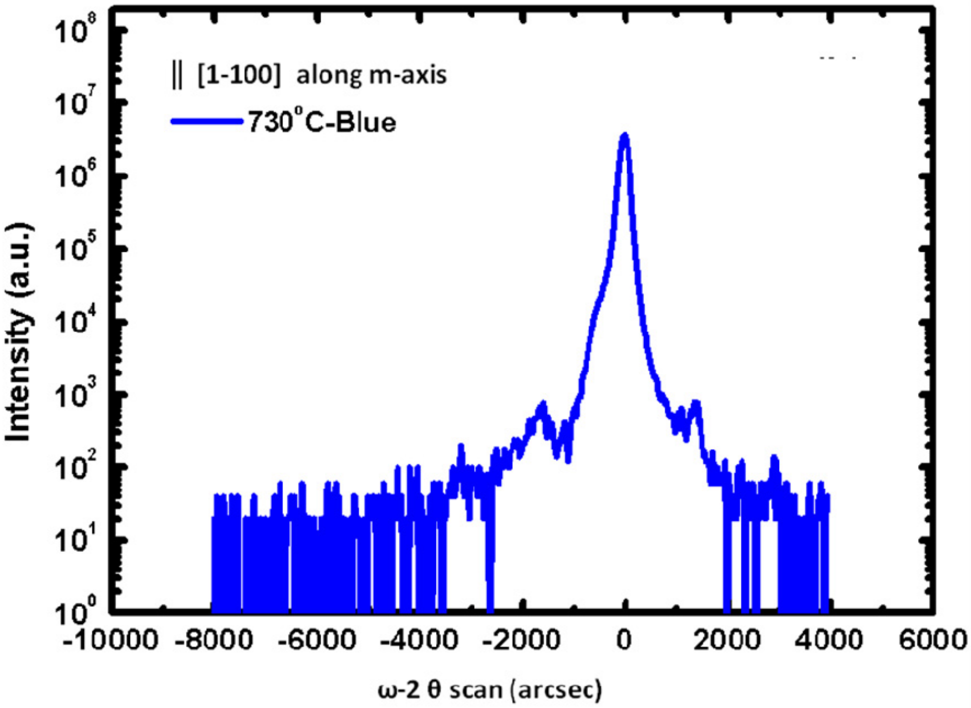

Figure 5.10. XRD ω-2θ spectrum along [1-100] direction of TELOG *a*-plane InGaN/GaN MQWs on γ-plane sapphire.

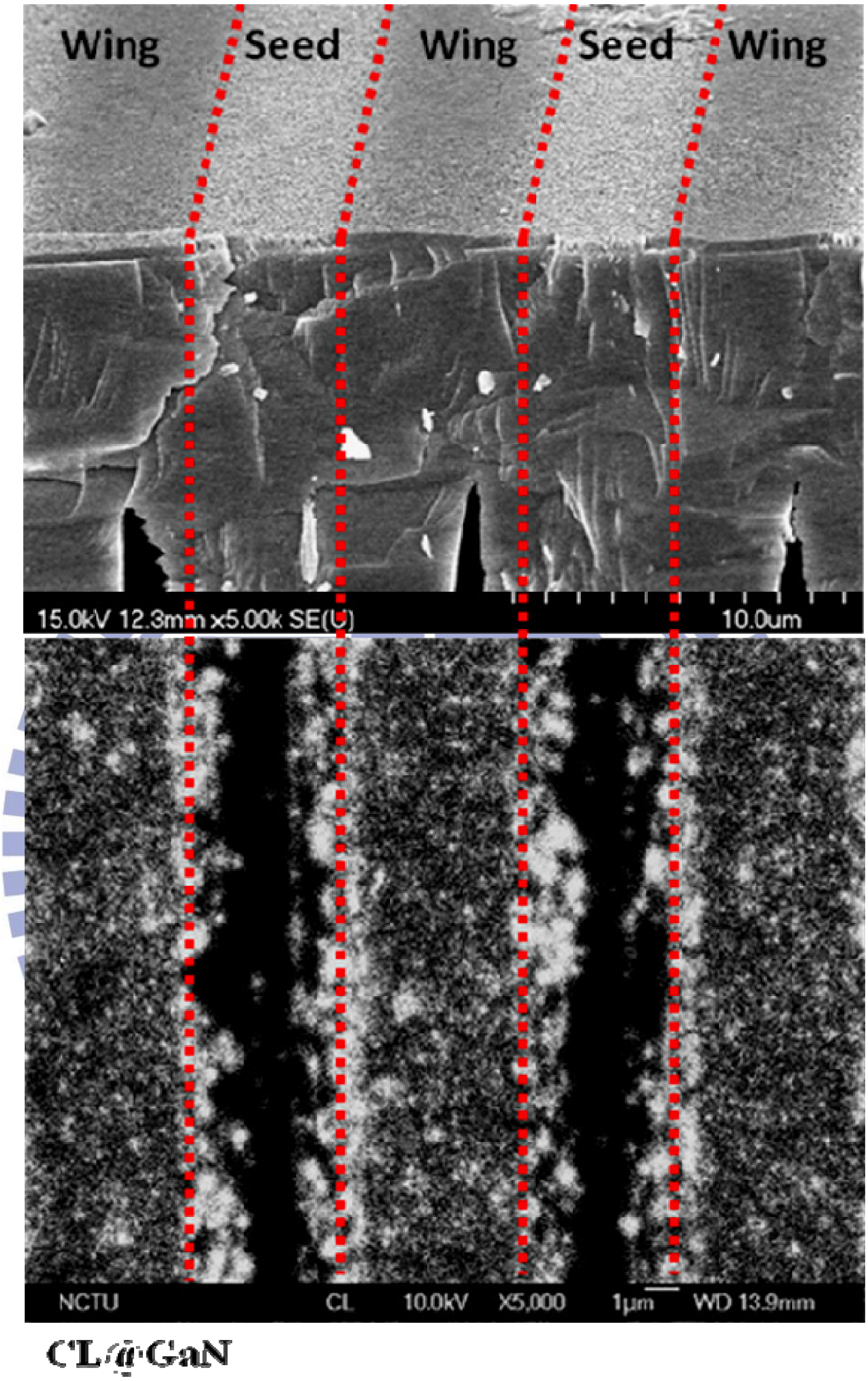

Figure 5.11. The CL mapping image at emission energy of GaN of the TELOG *a*-plane GaN and the corresponding SEM image. The corresponding seed and wing regions are depicted.

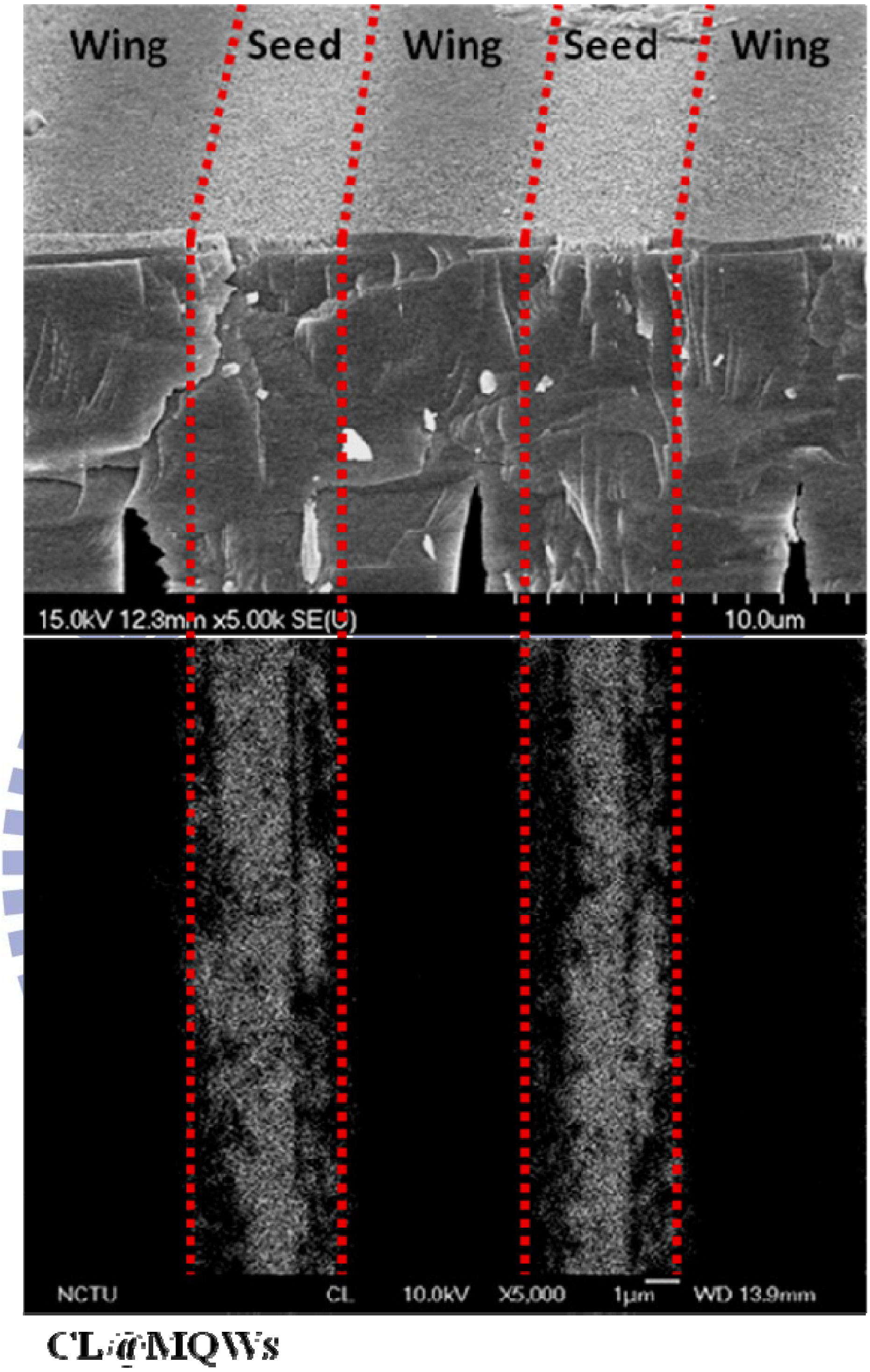

Figure 5.12. The CL mapping image at emission energy of InGaN/GaN MQWs of the TELOG *a*-plane GaN and the corresponding SEM image. The corresponding seed and wing regions are depicted.

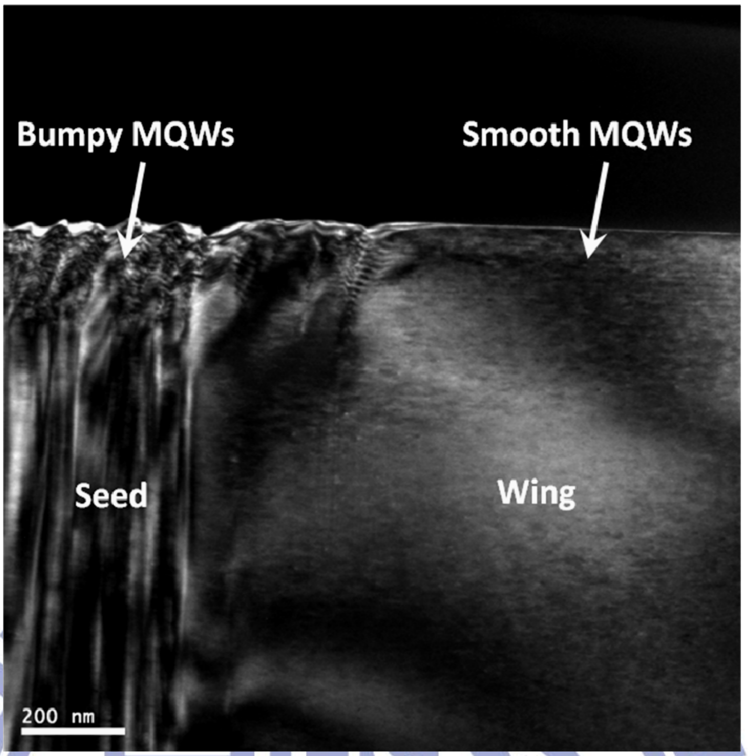

Figure 5.13. The TEM images of InGaN/GaN MQWs grown by MOCVD using TELOG technique under the V/III ratio of 72 and 980°C. The corresponding seed region, lateral wing region and the distribution of dislocations are depicted.

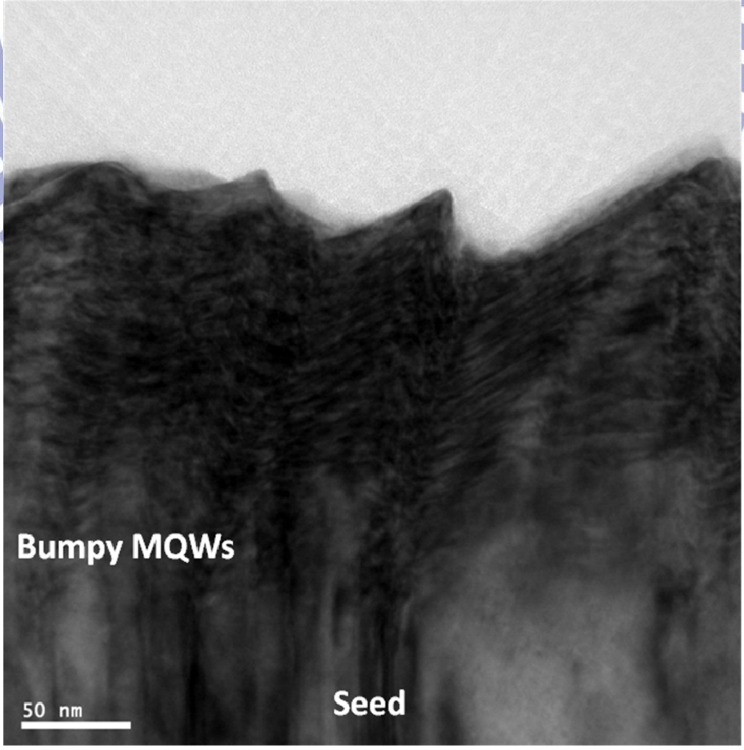

Figure 5.14. The TEM images of InGaN/GaN MQWs grown by MOCVD using TELOG technique under the V/III ratio of 72 and 980°C on the seed region.

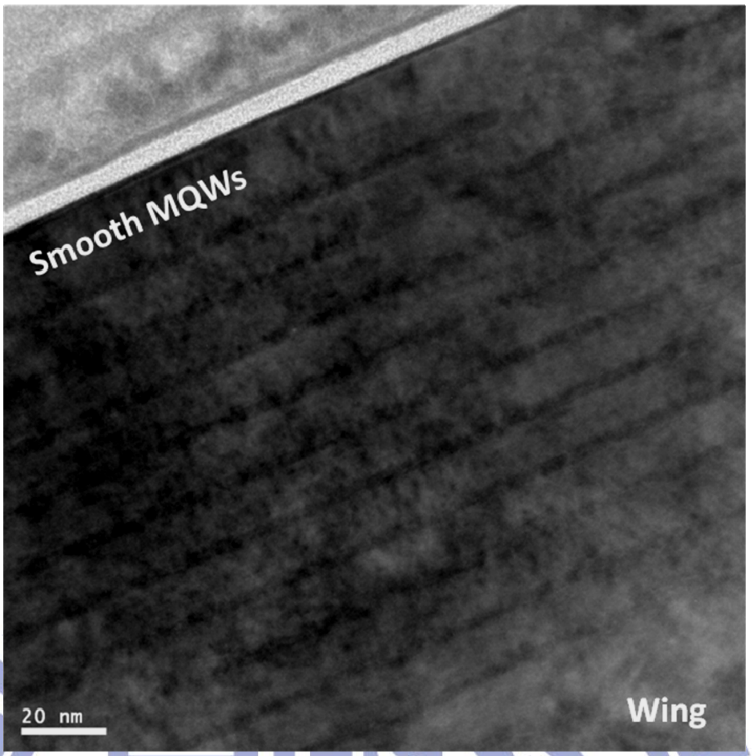

Figure 5.15. The TEM images of InGaN/GaN MQWs grown by MOCVD using TELOG technique under the V/III ratio of 72 and 980°C on the wing region.

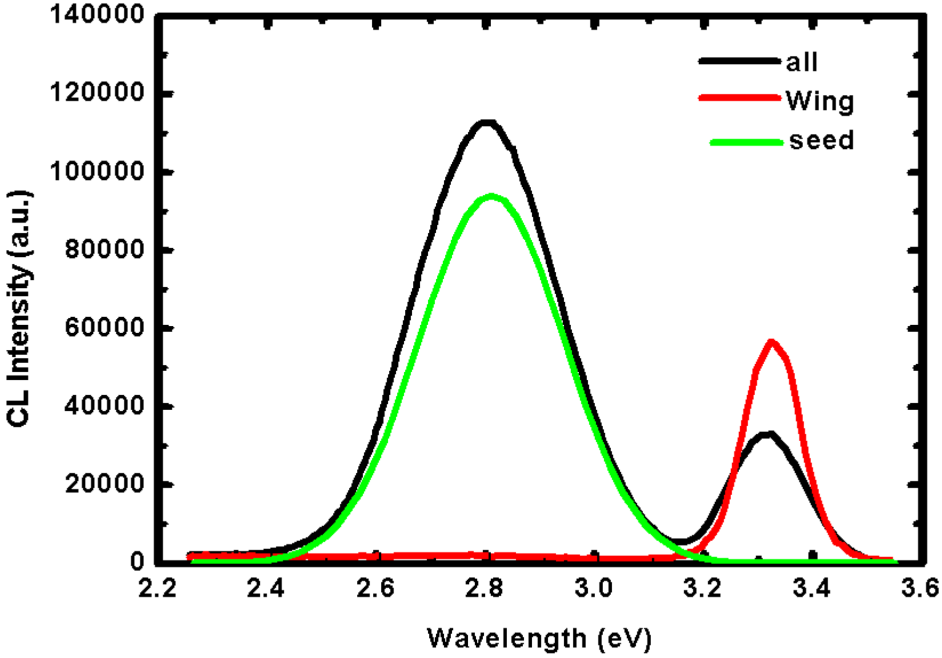

Figure 5.16. The CL mapping image at emission energy of both InGaN/GaN MQWs and GaN of the TELOG *a*-plane GaN. The peak position which corresponds to seed and wing regions are depicted.

Chapter 6

Result III – Etching of TELOG *a*-Plane GaN in KOH-Ethylene Glycol Solution

6.1 Review of Etching Mechanism of GaN in KOH-Ethylene Glycol Solution

Generally speaking, the wet chemical etching of semiconductor materials involve oxidation of its semiconductor surface and subsequent dissolution of the resulting oxides. The physical reaction process of oxidation requires holes that can be supplied either chemically or by an electrochemical circuit. Here in this discussing section of the research, the focusing point is chemical etching in aqueous etchants.

Chemical etching has a totally different etching mechanism in comparison with the electrochemical etching process. In that reaction process, no free electrical carriers or electrolyte are involved, thus, the whole etching process is not affected by external potential. The basic etching behavior can be described in structure-level as that the etchant break the atomic bonds at the semiconductor surface and form oxides that are subsequently dissolved in the etchant. In common research and engineering application region, conventional chemical etching of GaN in aqueous solution has been widely used for defect characterization, polarity identification and patterning. By distinguishing the etching behavior we observed in this experiment, chemical etching of GaN can generally be divided into two categories, namely “polarity-selective chemical etching” and “defect-selective chemical etching”. The details of these etching behaviors and the transformation between them will be discussed in section 6.2~6.4. Here in this section, a summarized etching mechanism of specific GaN crystalline planes is provided.

The vast majority of GaN semiconductors have been deposited on foreign substrates due to the lack of bulk group-III nitride single crystals. Thus, most wet etching studies have been made on such thin heteroepitaxial films, especially the *c*-plane GaN. However, the difference in the etching characteristics of Ga-polar and N-polar GaN has been revealed [6.01~6.10]. These experimental results have shown consistently that the N-polar GaN etches more readily than the Ga-polar GaN. The mechanism of the polarity-selective chemical etching was interpreted [6.11, 6.12] that the difference etching behaviors of Ga-polar and N-polar crystalline materials are due to the different state of surface bonding. This conclusion leads to the polarity-dependent etching characteristics, neither purely the surface-morphology-dependent nor purely growth-method-dependent.

The mechanism of N-polar GaN etching behavior is schematically shown in figure 6.01. In figure 6.01(a), a nitrogen terminated layer with one negatively charged dangling bond on each nitrogen atom was shown. Some hydroxide ions (OH^-) were also depicted to representing the wet chemical environment of KOH-based solution. In figure 6.01(b), hydroxide ions are initially adsorbed on the GaN surface and subsequently react with Ga atom, as the reaction, in figure 6.01(c):

$$2GaN + 3H_2O \xrightarrow{KOH} Ga_2O_3 + 2NH_3 . \qquad (6.01)$$

In figure 6.01(c), it indicated clearly that KOH acts as not only catalyst but also a solvent for the Ga_2O_3. After the Ga_2O_3 was dissolved, the N-polar surface of GaN shown again and via repeating the procedures in figure 6.01(a) to figure 6.01(d), the N-polar GaN can be effectively etched.

One thing worth noticing is that the etching mechanism did not matter which atom form the surface termination layer. The issue which needs consideration is polarity only in this research.

The etching behavior of Ga-polar GaN surface can be explained using the same set of figures in figure 6.01. Viewing the GaN from the +*c*-direction in figure 6.01(a), the Ga-terminated surface layer was initially reacted with the hydroxide ions. The etching mechanism of the first Ga layer is similar to that of N-polar etching. After the first Ga layer was removed, the inertness of Ga-polar GaN showed and prevented the surface from further etching. This behavior was ascribed to the repulsion between hydroxide ions and three occupied (negatively-charged) dangling bonds of nitrogen, which prevent the hydroxide ions from attacking the Ga atoms.

The etching mechanism in GaN (1-100) plane can be explained by the actions of hydroxide ions on the surface, similar to the aforementioned mechanism of –*c*-polar GaN. The summarized etching mechanism was depicted in figure 6.02 [6.13]. In figure 6.02(a) and 6.02(b), the OH^- ions are bound to the positively charged Ga dangling bonds. Then in figure 6.02(b) and 6.02(c), the OH^- ions attack the Ga bond connected to N atom in the layer below (Ga back bond) and be adsorbed. And finally the OH^-can react with the GaN, accompanied by the formation of Ga_2O_3 and NH_3 as shown in figure 6.02(d). These products are resolved by KOH-solution and H_2O. Via repeating the procedures in figure 6.02(a) to figure 6.02(d), the m-plane GaN can be etched.

While considering the etching behavior of GaN (11-20) plane, some differences from the aforementioned case of GaN (1-100) plane appeared. As depicted in figure 6.03[6.13], step (1) showed that OH^- ions attack Ga back bonds. These back bonds in this case are more stable than those in the (1-100) *m*-plane because the connected number of bonds to N atoms is three. In step (2), OH^- ions react with positively charged dangling bonds of top Ga surface. Unfortunately, while OH^- ions try to stay close to the positively charged dangling bonds, it will be repelled by the two negatively charged dangling bonds of N atoms. What worst is that the Ga atom is connected to two N atoms. These structures make the Ga back bonds much more inert, and the repelling force between hydroxide ions and N dangling bonds are larger than those of (1-100) *m*-planes. Therefore, a smaller number of hydroxide ions react with the Ga back bonds and leads that the etching of *a*-plane GaN cannot precede easily.

In brief, the etching mechanisms of specific GaN planes in KOH-based solution are summarized. Under normal etching temperature and concentration, the etching rate arranged in a series is –*c*-plane > *m*-plane > *a*-plane > +*c*-plane. On the basis, the results of our experiments can be explained appropriately in a punctilious frame, in section 6.2 ~ section 6.4.

6.2 Concentration, Temperature and Time Dependency of KOH Etching Tendency

Here in this section, the effects of three variables of KOH-ethylene glycol chemical solution etching including KOH-concentration, etching temperature and etching time are summarized into the nine patch diagrams in figure 6.04 ~ figure 6.07. These nine patch diagrams was constructed by etching temperature 100°C, 120°C and 140°C, KOH-concentration 5 wt. %, 10 wt. % and 20 wt. %, etching time 10 minutes, 20 minutes, 40 minutes and 80 minutes. In figure 6.04, the experimental conditions were fixed at etching time 10 minutes with different etching temperature and KOH-concentration.

Clearly it showed that in such a short etching time, only at 140°C and 20 wt. % of KOH led to “effective” etching result. The definition of “effective” etching results is the forming of perfect voids in triangular shape with specific planes. The related etching behavior (etching direction, etching-stop-planes, dominative cause included) and etching rate will be discussed in section 6.3 in detail.

While the etching time was longer, i.e. 20 minutes, figure 6.05 showed that the conditions which led to effective etching results were located in the region where etching temperature higher than 120°C *and* KOH-concentration higher than 10 wt. %. Moreover, at 40 minutes etching time, the region led to effective etching results were deeply extended into etching temperature equal to or higher than 120°C *and* KOH-concentration higher than 5 wt. %. It is depicted in figure 6.06. At the longest etching time, 80 minutes, almost all the etching conditions led to effective etching results except the condition of 100°C and 5 wt. % of KOH. The left-bottom side of figure 6.07 showed clearly the powerlessness of etching under such condition.

All the etching tendencies of different temperature, concentration and time were summarized in figure 6.08. The vertical axis represents different etching temperature from 100°C to 140°C while the horizontal one represents the KOH-concentration from 5 wt. % to 20 wt. %. The third variable, etching time, is depicted as the inclined lines which classify the etching results in figure 6.04 to 6.07 into two categories, effectively-etched and ineffectively-etched. The meaning of “effectively-etched” and “ineffectively-etched” are similar to the aforementioned definitions. Look at the illustration in figure 6.08 first. It describes the classification method of inclined line of etching time. In a specific period of etching time, T, the conditions at right-upper side of the line can perform effectively-etched triangular-shaped voids, as in the figure depicted. However, the conditions at left-bottom side of the line show only partial or slight etching results which do not accompany with the triangular-shaped voids.

The figure 6.08 has the ability of predicting the experiment conditions. For instance, under a selected etching condition of temperature and concentration, the etching time required to acquire effectively-etched triangular-shaped voids can be determined. It needs only a simple technique of intersecting the condition point with the inclined interpolating time line.

If the selected and fixed etching condition was etching time, the sets of temperature and concentration can be determined by extending straight lines toward the two axes and finding out the intersections.

Direction of refinement of figure 6.08 is a complicated process of experiment. The exact curvatures of the time lines need further investigation. Here we optimistically predict that the concave/convex shape of the time lines is strongly depending on solvent, *a*-plane GaN template quality, defects distribution, and so on.

Figure 6.09 ~ figure 6.15 show the time-tendency of etching results under different KOH concentration and temperature. In figure 6.09, the low etching temperature and low KOH concentration lead to powerlessness of etching ability no matter how long the etching time is. Figure sets of 6.10 ~ 6.12 show the time-tendency of etching results under different KOH concentration at fixed 120°C. It points out that the higher the KOH concentration, the quicker the effectively-etched triangular-shaped voids appear. The same tendency exist also in figure set of 6.13 ~ 6.15. It shows the time-tendency of etching results under different KOH concentration at fixed 140°C. The time required to effectively form the etched triangular-shaped voids are much shorter, 10 minutes, especially for the condition of 20 wt. %, 140°C.

An extremely long etching time, 160 minutes, was performed in the condition of 20 wt. %, 120°C. The result in the right-end of figure 6.12 depicts a series of trapeziums voids rather than the triangular-shaped voids aforementioned. The similar etching result can be seen in the right-end of figure 6.15 with etching time 80 minutes in solution of 20 wt. %, 140°C. The further spreading of the etching results is exactly comparable with the triangular-shaped one with no conflicts. The explanations are available in section 6.3 in detail.

6.3 Identification of Chemical Etching Behaviors and Rate Characterization of TELOG *a*-Plane GaN in KOH-Ethylene Glycol Solution

In order to identify the etching behavior of TELOG *a*-plane GaN and MQWs in KOH-Ethylene Glycol Solution, a specific etching condition which performs the etching result of every etching step is chosen. Figure 6.16 show the different degree of chemical etching in time series under 10% KOH-Ethylene Glycol solution at 120°C. The schematic description of the etching degrees and the time-dependency of it are shown in figure 6.17 with time gradually increasing from time 0 to time 4. Under rough and initial observation, the etching results are perfectly matching to that of aforementioned tendencies. However, the well-defined geometric shape of these etched-voids reveals the etching behavior that dominates during the periods. As can be seen, all the etched voids, no matter what degree of etching it performs, are confined in an isosceles triangle with the base angles ~58° and vertex angle ~ 64°. Via calculation and analysis about the crystalline structure of TELOG *a*-plane GaN, it is confirmative that the legs of the isosceles triangle are {11-22} planes.

What more interesting is that the isosceles triangle voids all aligned with their vertex angle toward the [0001] direction of GaN, i.e. the plane suffered from KOH-Ethylene Glycol chemical etching is –*c*-plane. The base plane, +*c*-planes are almost unaffected by the etching processes. The difference of etching behavior of +*c* and –*c*-planes of GaN here are exactly fitting in with the aforementioned mechanism in section 6.1. However, the etched-voids are isosceles triangle rather than rectangular voids with edges +*c*-plane, -*c*-plane, *a*-plane and –*c*-plane sapphire surface (the totally etched of the dislocation-filled seed region). A concept of "polarity-selectivity" is appropriate for explaining the result.

In the realm of polarity-selective chemical etching, the –*c*-plane is etched with extremely fast rate and the +*c*-plane remains still. And, interestingly, the shrinkage of –*c*-plane does not consist of smooth and perfect vertical crystalline planes, but a lot of corrosional small facets of {11-22} planes. As in figure 6.16, at etching time 10 min, the –*c*-plane are constructed by plenty of {11-22} facets. At etching time increasing to 20 min, the shrinkage of the –*c*-plane continues and the number of {11-22} facets decreases gradually with the size enlarges progressively. As for the 40 min etching time, the {11-22} facets are numbered and the –*c*-plane shrinkages to almost the vertex angle. Eventually the 80 min etching time gives the complete isosceles triangle constructed by two {11-22} planes as the legs and +*c*-plane as the base plane.

To note, the above-mentioned etched regions are all located in the seed region with dislocations. The homogeneous seed region under chemical etching does not form a rectangular void but an isosceles triangle. It is the polarity-selective etching mechanism that dominates the etching in these periods and obviously distribution of dislocations does no effect upon the final etching geometry, i.e. the isosceles triangle.

The study more about the dominating factors of the etching mechanism, an increasing of KOH-Ethylene Glycol Solution concentration and the etching time are performed. Figure 6.18 shows the etching result under 20% KOH-Ethylene Glycol solution at 120°C with etching time 160 min. Unlike the aforementioned isosceles triangle void, a trapezoid void forms. The dramatically change of the geometry of the etched-voids reveals a new dominating mechanism during the etching process. Observing the trapezoid void in detail, the trapezoid was constructed by an isosceles triangle with the further etched {11-22} planes upwardly and downward. The lower leg ((11-22) plane) of isosceles triangle is further etched in direction normal to (11-22) plane and stop at the sapphire surface and the boundary of seed and wing region. The completely etching of the seen region was achieved at the bottom part of the seed region. As for the upper part of the seed, the upper leg ((11-22) plane) of isosceles triangle is also further etched in direction normal to (11-22) plane; however, it shows no sign of etching-stopping. The (11-22) plane is maintained and advances upwardly in the [11-20] direction rather than in direction normal to (11-22) plane. Combining the etching results of upper and lower {11-22} planes, geometry of trapezoid forms.

Enlarging upon the results, an etching mechanism "defect-selectivity" is introduced. The advancing of the {11-22} planes stop at the seed/wing boundaries without further invading into the wing region. All the etching behavior was confined exactly in the seed region even under extreme etching conditions, i.e. high temperature and high concentration. The difference between the crystalline qualities, i.e. the amount of dislocations explains the defect-selectivity of etching well. Under extreme etching conditions, the etching behavior of polarity-selectivity stops for the etching –c-planes advancing no more into the high quality wing region. The etching continues in the [11-20] direction with inclined upper (11-22) plane and be completely confined in the dislocation-filled seed region. The determinative factor transfers from polarity to quality dramatically.

The transition point between polarity-selectivity and defect-selectivity is sometimes not sharp at all. It can be seen in figure 6.19 that polarity-selective chemical etching and defect-selective chemical etching occur at the same moment. The region of polarity-selective etching shows specific crystalline planes while the defect-selective etching does not. The combination of these two etching mechanism leads to variety of the geometry of the voids if the crystalline quality of the seed region is not good enough to be effectively recognized from the etching of {11-22} planes and the isosceles triangle. Besides, the defect-selective etching along the defective coalescence boundary and the direct growth region on seed could lead to serious damage to the MQWs on the n-GaN and destruct the light emission properties.

The way to avoid this phenomenon is maintaining the etching condition at moderate temperature and concentration and the etching time should not be too long.

The quantitative etching rate of the {11-22} planes must be measured in order to apply to further similar etching experiments. As for the requirement, the image of original void here in figure 6.20 is needed. The important information it contains is the width of the initial voids, 300~400nm.

The calculation method of the etching rate of an inclined crystalline plane must be carefully treated. For nonvertical planes, the etching rate of the plane is not measuring the enlargement of the spatial distance directly. For instance, the etching rate of {10-1-2} planes is the etching rate of vertical {10-10} planes multiplied by $\cos 46^{\circ}$, because the inclined {10-1-2} planes intersect the {10-10} planes at an angle of 46°.

In our case, the determination of etching rate of {11-22} planes is depicted in Figure 6.21. The vertical dot-line in upper-left figure of Figure 6.21 marks the original width of the void and be replicated to the other figures to indicate the start point of etching. As the aforementioned topics, the {11-22} planes intersect the {0001} planes at an angle of 58° and thus the etching rate is calculated by dividing the etching distance normal to {11-22} planes by etching time. The etching distance normal to {11-22} planes is defined as $L_{(0001)} \times \cos 58^{\circ}$ where $L_{(0001)}$ is the etching distance normal to the {0001} planes under certain etching time.

The etching rates of {11-22} planes under different conditions are summarized in Figure 6.22. It is clear that both the increasing of temperature and KOH-concentration leading to higher etching rate. The fastest etching rate that achievable in the experimental series is approximately 26.0±1.90 nm/min under the condition of 140°C, 20 wt. % KOH. The lower temperature about 120°C, 20 wt. % KOH leads to slower etching rate about 20.5±1.70 nm/min.

Look at the etching rate performances at low KOH concentration, 5 wt. %. Temperature 140°C gives the rate of 11.6±1.08 nm/min, while 120°C gives the rate of 6.34±1.33 nm/min and 100°C gives the rate of 2.35±1.67 nm/min. The etching rate decreases dramatically under such low KOH concentration and the worth noting point is that the deviation of the rate increases as the etching temperature decreases. This tendency is opposite to that of observed at high KOH concentration, 20 wt. %. Therefore, we can guess confidently that the moderate KOH concentration with moderate temperature gives the most controllable etching conditions.

The condition of 140°C with KOH concentration 10 wt. % gives an etching rate about 17.0±1.00 nm/min, and 120°C with KOH concentration 10 wt. % gives an etching rate about 13.6±0.90 nm/min. Although the etching efficiency is not as high as that of higher concentration, 20 wt. %, it provides most controllable etching conditions with smallest rate deviation. This is a compromise between the etching rate and the etching controllability.

Knowing the nature of the etching rates helps to determine the etching time in order to achieve a specific geometry of the voids in TELOG *a*-plane GaN and MQWs. These well-shaped voids would expect to enhance the light extraction ability of the nonpolar *a*-plane GaN and MQWs for the air-voids acting as the reflector and guiding the emission light from MQWs to go upwardly and out of the sample from the front surfaces. The quantitative measurements of the optical properties of the TELOG *a*-plane MQWs are available in section 6.4.

6.4 Optical Properties of TELOG *a*-Plane InGaN/GaN MQWs after KOH-Ethylene Glycol Solution Etching

The continuous-wave He-Cd laser excited photoluminescence spectrum measured at room temperature of TELOG *a*-plane InGaN/GaN MQWs is shown in Figure 6.23. The detection position is exactly normal to the TELOG *a*-plane GaN sample within the distance of approximately 10cm. The photoluminescence peak emission wavelength of the TELOG *a*-plane InGaN/GaN MQWs is 435nm whether the sample is KOH-etched or not. The intensity of these peaks, however, shows an interesting tendency. The KOH-etched sample gives higher peak than that of the original one, and this phenomenon could be explained briefly by the effects of air-void assisted light-extraction-efficiency enhancement. Confusing point is that the percentage of enhancement does not proportional to the etching time length. In general and the results above-mentioned, the longer etching time leads to larger air-void size, whether the dominating mechanism it is. Unfortunately, the photoluminescence peak intensity of the sample after 80-min-etching drops dramatically to the level of 20-min-etching one with only slight larger. The results are conflicts to the previous prediction.

By investigation in to the geometry of the void after 80 min etching, the simulation model of *TracePro* was constructed as in Figure 6.24, where the corresponding materials area depicted. The vertex angle of the isosceles triangle is designed toward the right-hand side in order to meet the SEM images in the aforementioned sections. Figure 6.25 shows the distribution of the light trajectories initiating from the InGaN/GaN MQWs and be extracted out of the sample by the isosceles triangles. There exists evidently a higher density of light trajectories in the quadrant corresponding to the upper {11-22} planes. This simulation results tell that the most effective light extraction efficiency enhancement is located at the position with a rotation of 30° toward the vertex angle, and respect to the normal of the sample.

On the basis of the above-mentioned simulation result, the experiment of angle-resolved photoluminescence is performed to acquire the exact angle of the peak position and the maximum enhancement of the light extraction efficiency by these isosceles triangles. The experiment was performed by varying the angle of the detector and the record of the photoluminescence spectra was stored. Then the peak intensity of the photoluminescence spectra at each angle was extracted out to construct the Figure 6.26. At detection angle 0°, the tendency of the intensity toward etching time is similar to that of Figure 6.23. Surprisingly, the maximum enhancement of the light extraction efficiency occurs at the angle 30°, which is consistent in the previous simulation. As in the figure, the original TELOG *a*-plane InGaN/GaN MQWs shows no obvious enhancement for its symmetric and relatively small voids. A maximum enhancement around 2.5 times occurs at the angle 30° for 40-min-etching and 20-min-etching samples. Combining the effects of the lateral width of the isosceles triangles and the number of {11-22} facets on {000-1} plane, these two etching conditions gave the similar light extraction efficiency enhancement. The gradual decay of the spectra for the detection angle >30° is mainly caused by the total internal reflection at the *p*-GaN and air boundary. The detection angle is larger than the particular critical angle with respect to the normal to the surface. The critical angle is defined as the angle of incidence above which the total internal reflection occurs.

As for the case of 80-min-etching TELOG *a*-plane InGaN/GaN MQWs, the emission intensity increases gradually and reaches a saturated value at the detection angle $>40^{\circ}$ without obvious decaying. The 80-min-etching sample provides an enhancement of the light extraction efficiency to the level of 3.5 times with wide emission angle in comparison with that of the 40- and 20-min-etching samples.

The wide light emission angle and the saturated intensity without decaying of 80-min-etching sample come from the variety of the geometry of the air-voids it has. As in Figure 6.16, 6.18 and 6.19, the long etching time would lead to many kinds of the air-void shape including the isosceles triangles, trapezoids and the mixed form which combines the polarity-selective and defect-selective etching. The light extraction comes from the combination of the variety of air-void shape making a large emission angle. The phenomenon of this enhancement of light extraction shows a great potential for lighting application with varying emission angle. Via combining the polarity-selective and defect-selective etching appropriately, the optimum air-void shape can be achieved to acquire the largest emission range with several times enhancement.

Considering the detection angle opposite to the direction of the vertex angle of the isosceles triangle, i.e. $0^{\circ} \sim -45^{\circ}$, these are enhancements approximately ~20% at every detecting angle. The amount of enhancement is not as much as those at the direction toward the vertex angle of the isosceles triangle and can be explained by the smooth and vertical +*c*-plane without any etching facets. It does not much effort on enhancing the emission into a specific angle with several times but the average improvement of the light extraction efficiency is observable, even to the extremely large detecting angle, -45°.

6.5 Summary

The etching properties, including mechanisms, geometries, rates and the related effects of TELOG *a*-plane GaN and InGaN/GaN MQWs in KOH-ethylene glycol solution are available in this chapter.

Initially, the KOH-ethylene glycol etching mechanism of ±*c*-planes, *m*-plane and *a*-plane of GaN are reviewed. Then the etching tendencies of temperatures, concentrations and times are described and can be categorized into polarity-selective etching and defect-selective etching. Theoretically, by combining these two etching mechanism and the design of the *a*-plane GaN template in TELOG techniques, almost geometry of the air-voids with any size are available.

The light extraction efficiencies got a great enhancement due to the existence of the air-voids with specific shapes. The emission intensities and the emission distribution ranges are strongly depending on the geometries of the voids, isosceles triangle or trapezoid or the mixed one.

The integration of nonpolar *a*-plane GaN and the light extraction techniques of air-voids are successfully achieved. It provides a possible way toward suppressing the internal electrical field that hinder the recombination of electrons and holes, and enhancing the light extraction ability the help more photons to leave the devices.

6.6 References

[6.01]T. Palacios, F. Calle, M. Varela, C. Ballesteros, E. Monroy, F.B. Naranjo, M.A.

Sánchez García, E. Calleja, E. Muñoz, Semicond. *Sci. Technol.* **15** (2000) 996.

[6.02]Hock M. Ng, N.G. Weimann, A. Chowdhury, *J. Appl. Phys.* **94** (2003) 650.

[6.03]Hock M. Ng, A. Chowdhury, W. Parz, N.G. Weimann, *Proceedings of the Electrochemical Society: State-of-the-Art Program on Compound Semiconductors XXXIX and Nitride and Wide Bandgap Semiconductors for Sensors, Photonics and Electronics IV*, vol. **2003–11**, 2003, p. 3.

[6.04]Hock M. Ng, W. Parz, N.G. Weimann, A. Chowdhury, *Jpn. J. Appl. Phys.* Part 2 **42** (2003) L1405.

[6.05]D. Huang, P. Visconti, K.M. Jones, M.A. Reshchikov, F. Yun, A.A. Baski, T. King, H. Morkoc¸, *Appl. Phys. Lett.* **78** (2001) 4145.

[6.06]P. Visconti, K.M. Jones, M.A. Reshchikov, R. Cingolani, H. Morkoc¸, R.J. Molnar, *Appl. Phys. Lett.* **77** (2000) 3532.

[6.07]P. Visconti, D. Huang, M.A. Reshchikov, F. Yun, T. King, A.A. Baski, R. Cingolani, C.W. Littion, J. Jasinski, Z. Liliental-Weber, H. Morkoc¸, Phys. Stat. Sol. B 228 (2) (2001) 513.

[6.08]P. Visconti, D. Huang, F. Yun, M.A. Reshchikov, T. King, R. Cingolani, J. Jasinski, Z. Liliental-Weber, H. Morkoc¸, *Phys. Status Solidi A* **190** (1) (2002) 5.

[6.09]P. Visconti, D. Huang, M.A. Reshchikov, F. Yun, R. Cingolani, D.J. Smith, J. Jasinski,W. Swider, Z. Liliental-Weber, H. Morkoc¸, *Mater. Sci. Eng. B* **93** (2002) 229.

[6.10]M. Shimizu, A. Suzuki, M.Watanabe, J. Shirakashi, K. Balakrishan, H. Okumura, (Eds.), Kentaro Onabe, Blue Laser and Light Emitting Diodes II, in: International Symposium on Blue Laser and Light Emitting Diodes II, Chiba, Japan, September 29~October 2, 1998, p. 723.

[6.11]D. Li, M. Sumiya, K. Yoshimura, Y. Suzuki, Y. Fukuda, S. Fuke, Phys. *Status*

Solidi A **180** (2000) 357.

[6.12]D. Li, M. Sumiya, S. Fuke, D. Yang, D. Que, Y. Suzuki, Y. Fukuda, *J. Appl. Phys*. **90** (2001) 4219.

[6.13]M. Itoh, T. Kinoshita, C. Koike, M. Takeuchi, K. Kawasaki, Y. Aoyagi, *Jpn. J. Appl. Phys*. **45**, No. 5A (2006) 3988

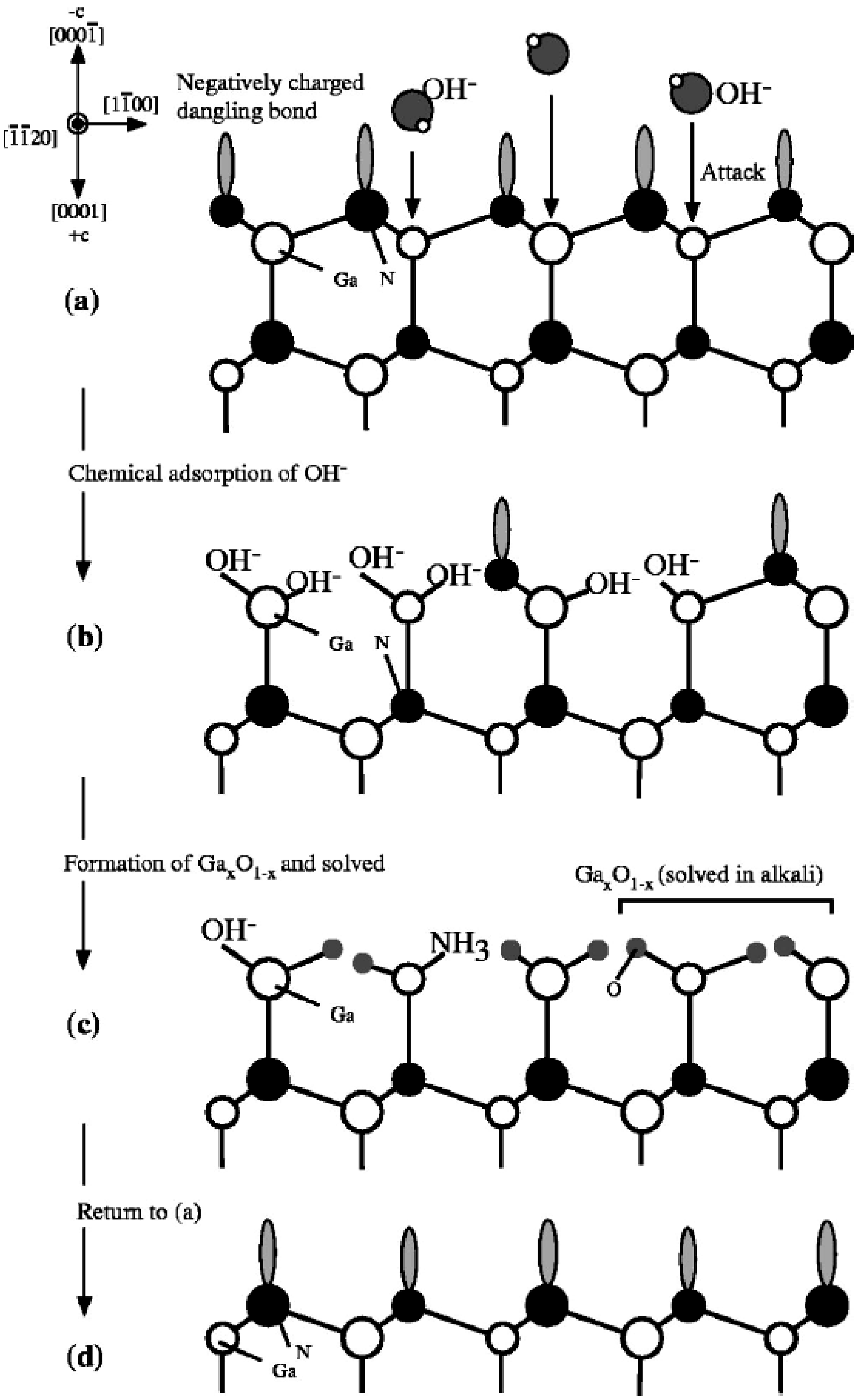

Figure 6.01. Schematic diagrams of the GaN viewed along the [-1-120] for N-polar GaN to explain the mechanism of the polarity-selective chemical etching.

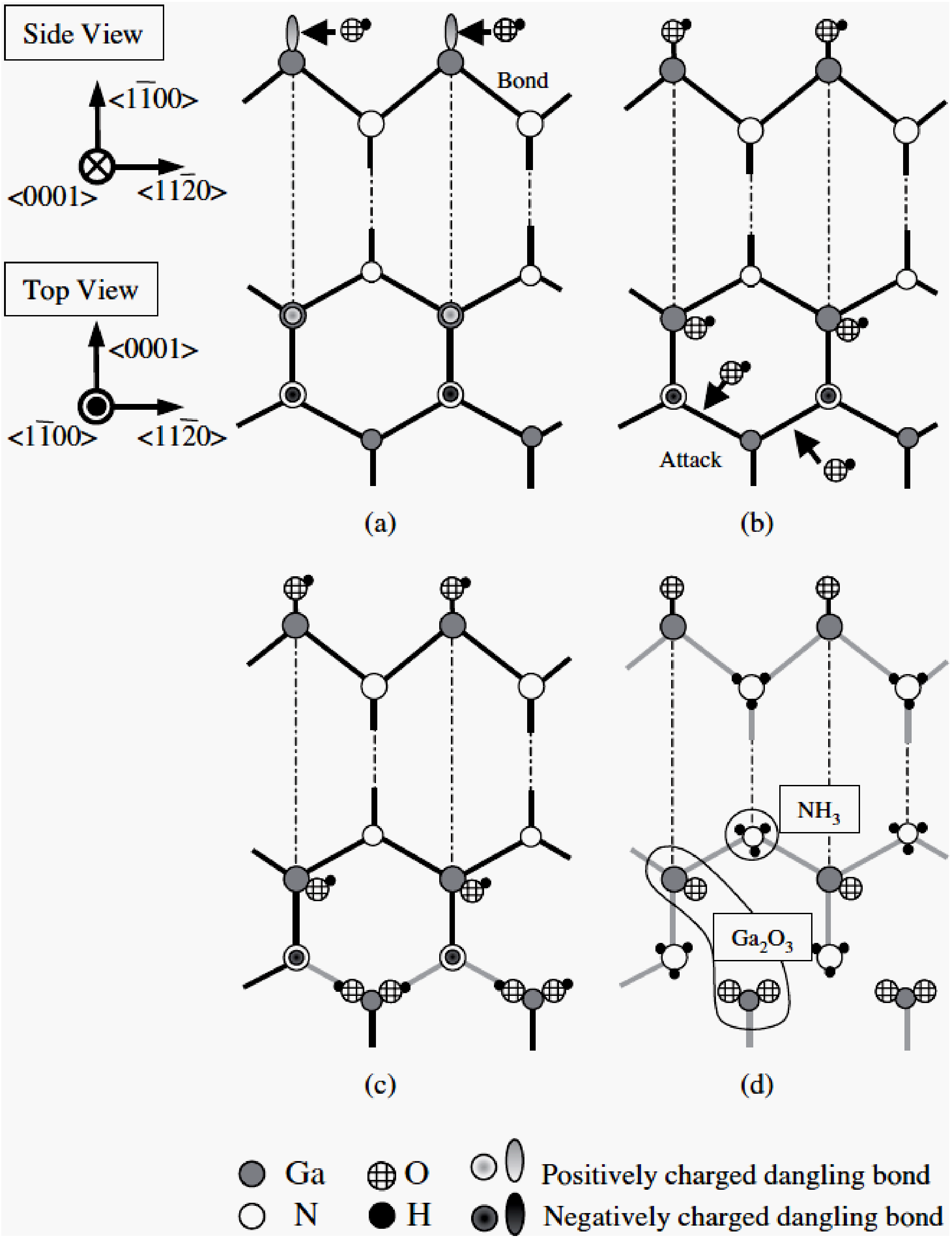

Figure 6.02. Scheme of etching mechanism of GaN (1-100) *m*-plane in top and side views.

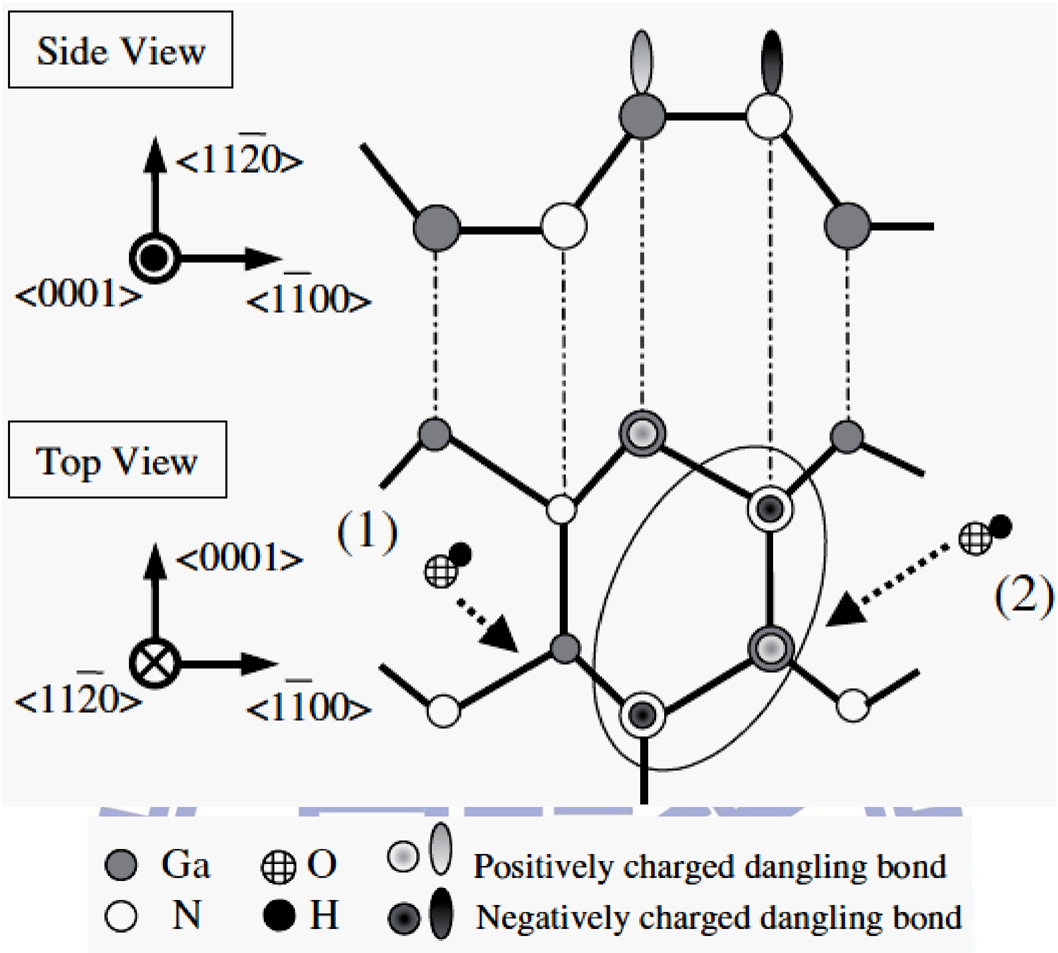

Figure 6.03. Scheme of etching mechanism of GaN (11-20) *a*-plane in top and side views.

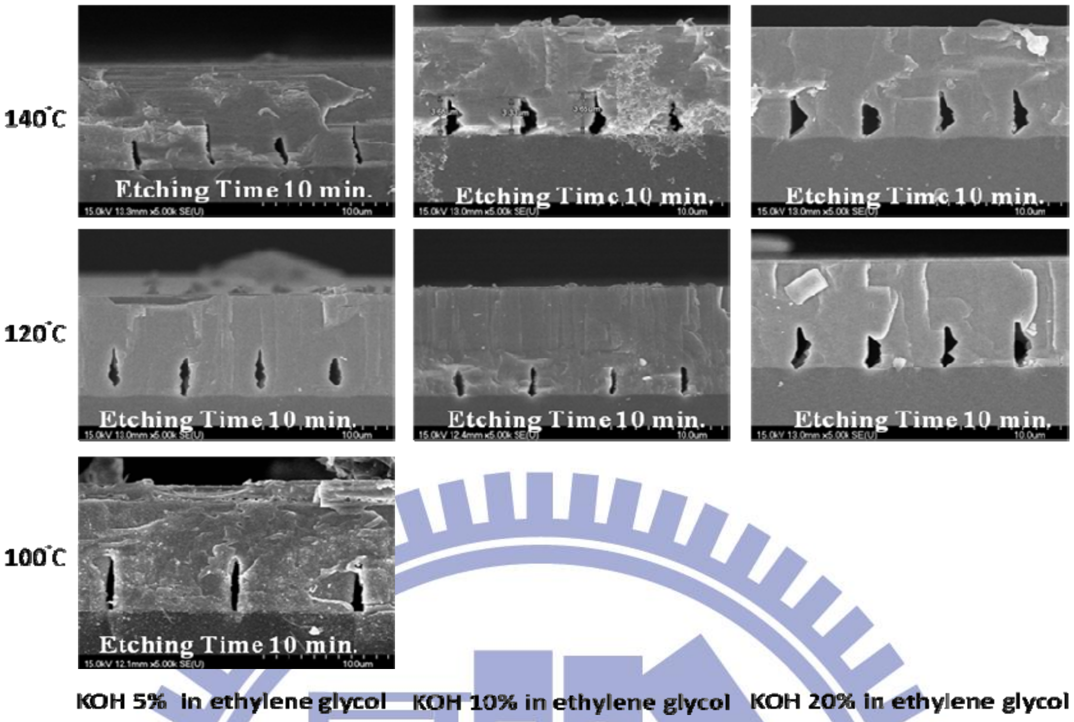

Figure 6.04. SEM images of the air-voids in TELOG *a*-plane GaN under different etching conditions at etching time 10 min.

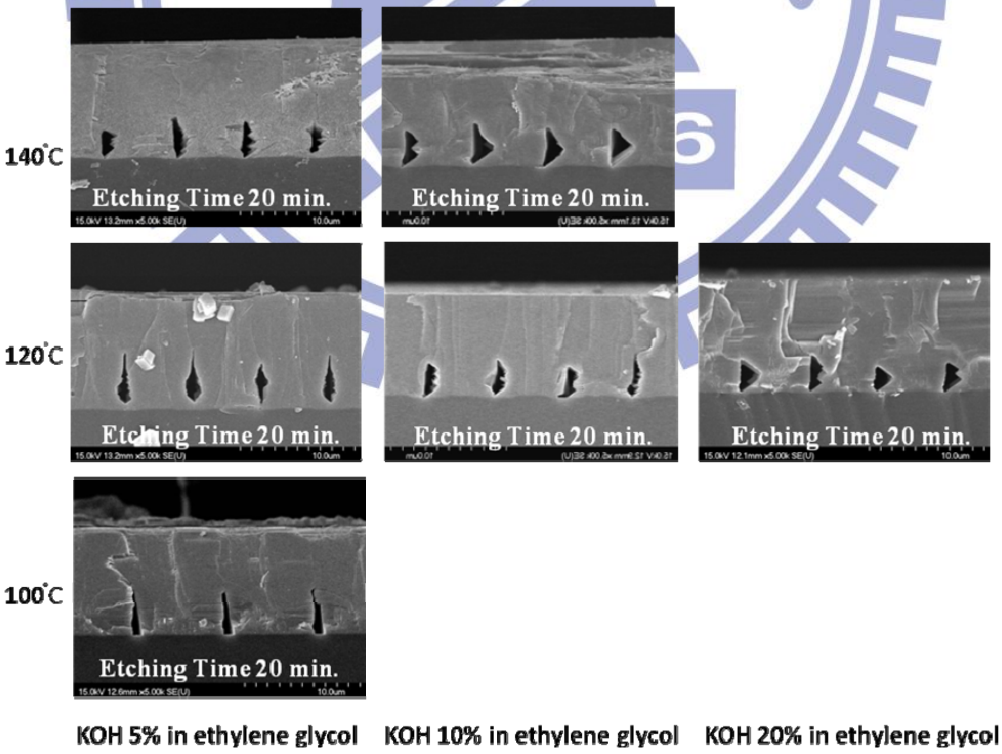

Figure 6.05. SEM images of the air-voids in TELOG *a*-plane GaN under different etching conditions at etching time 20 min.

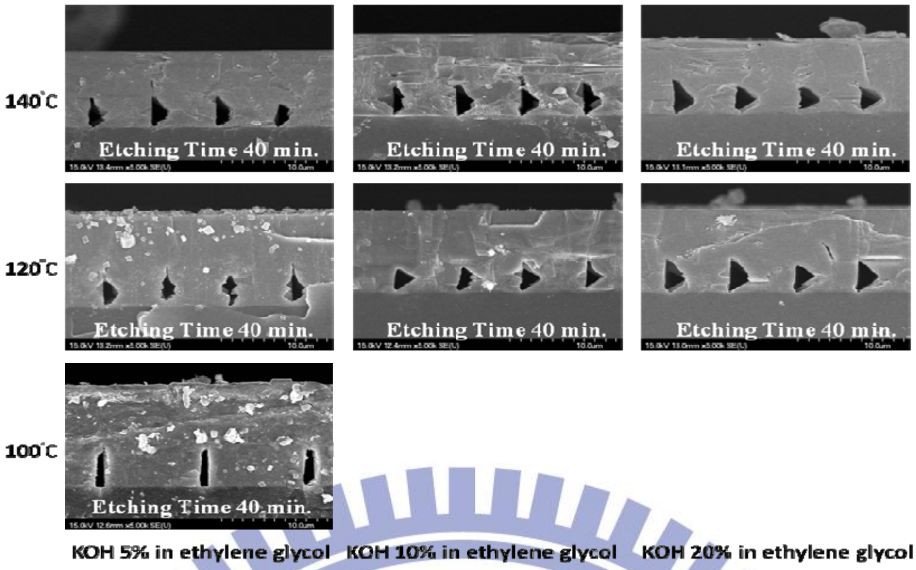

Figure 6.06. SEM images of the air-voids in TELOG *a*-plane GaN under different etching conditions at etching time 40 min.

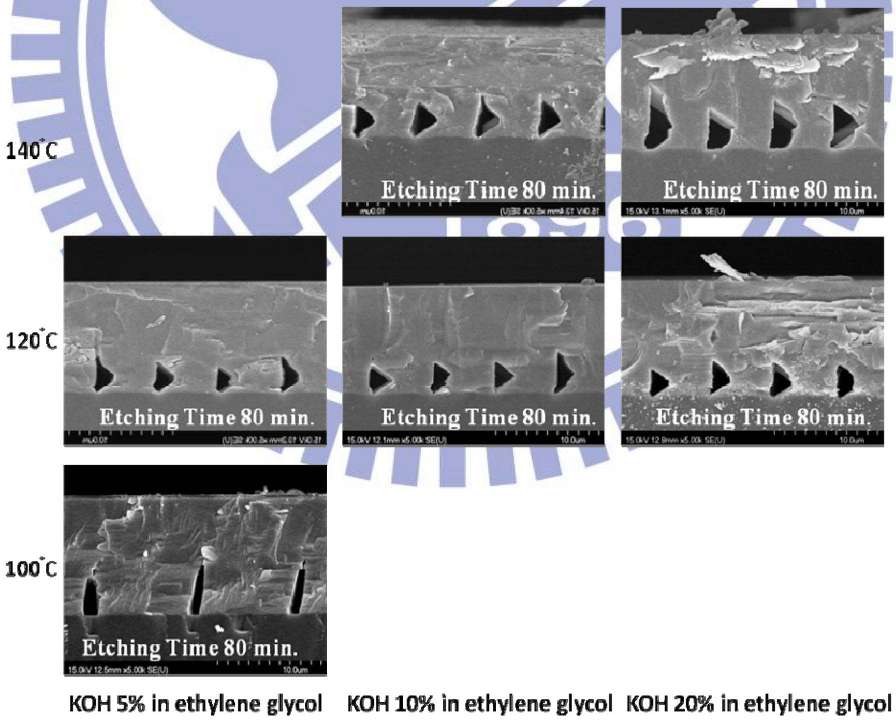

Figure 6.07. SEM images of the air-voids in TELOG *a*-plane GaN under different etching conditions at etching time 80 min.

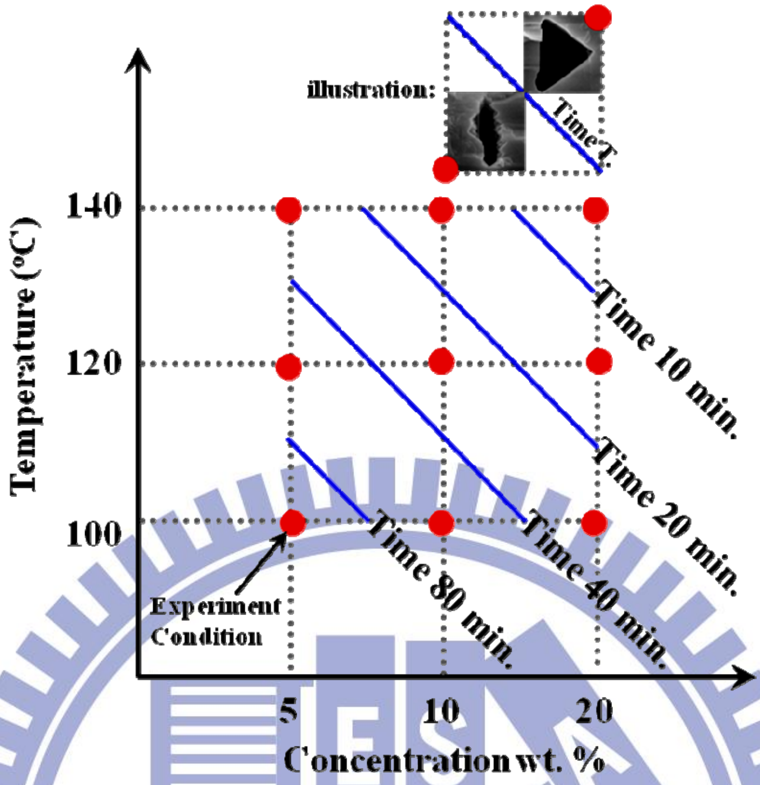

Figure 6.08. The summary of the etching results under different etching conditions. The threshold-times needed to get the isosceles triangle are shown.

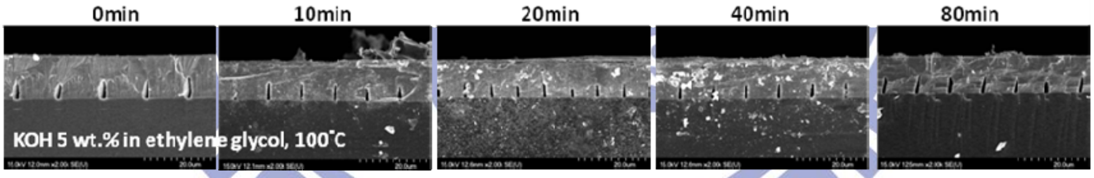

Figure 6.09. Time-dependent SEM images of the air-voids in TELOG *a*-plane GaN under KOH 5 wt. % and 100°C.

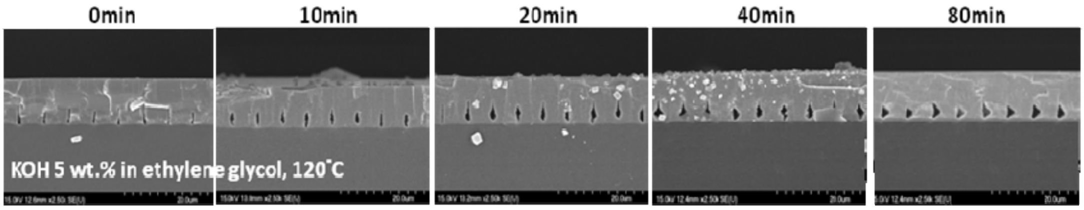

Figure 6.10. Time-dependent SEM images of the air-voids in TELOG *a*-plane GaN under KOH 5 wt. % and 120°C.

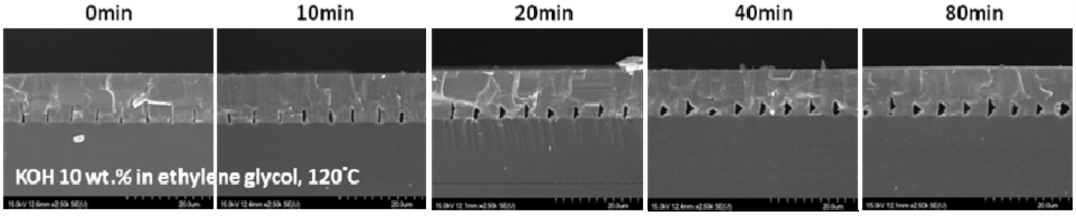

Figure 6.11. Time-dependent SEM images of the air-voids in TELOG *a*-plane GaN under KOH 10 wt. % and 120°C.

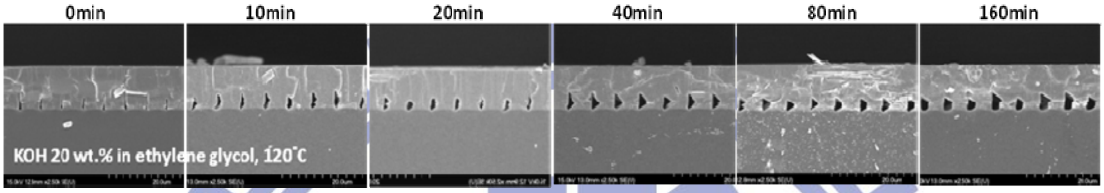

Figure 6.12. Time-dependent SEM images of the air-voids in TELOG *a*-plane GaN under KOH 20 wt. % and 120°C.

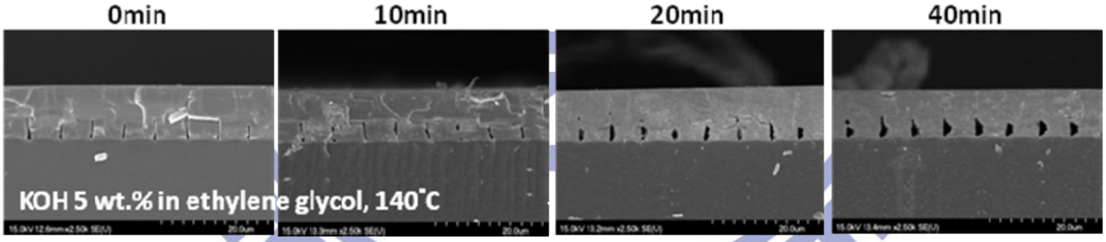

Figure 6.13. Time-dependent SEM images of the air-voids in TELOG *a*-plane GaN under KOH 5 wt. % and 140°C.

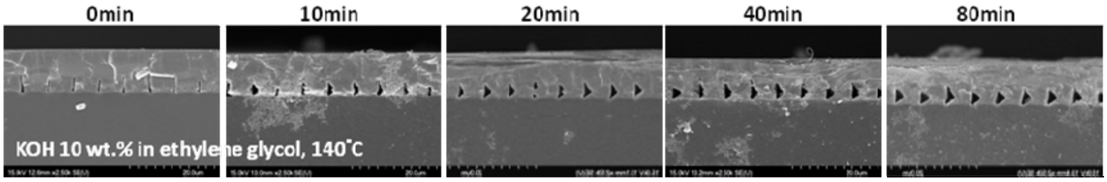

Figure 6.14. Time-dependent SEM images of the air-voids in TELOG *a*-plane GaN under KOH 10 wt. % and 140°C.

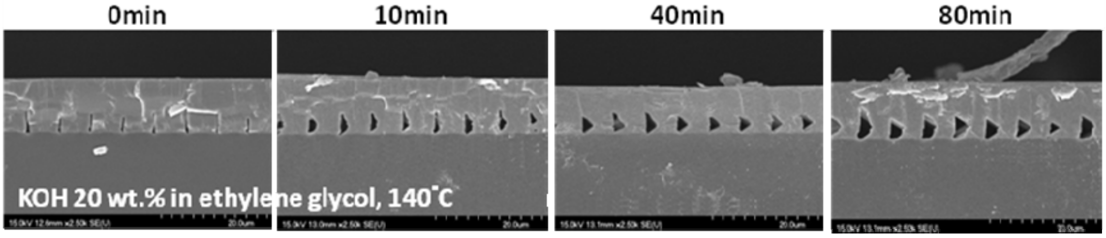

Figure 6.15. Time-dependent SEM images of the air-voids in TELOG *a*-plane GaN under KOH 20 wt. % and 140°C.

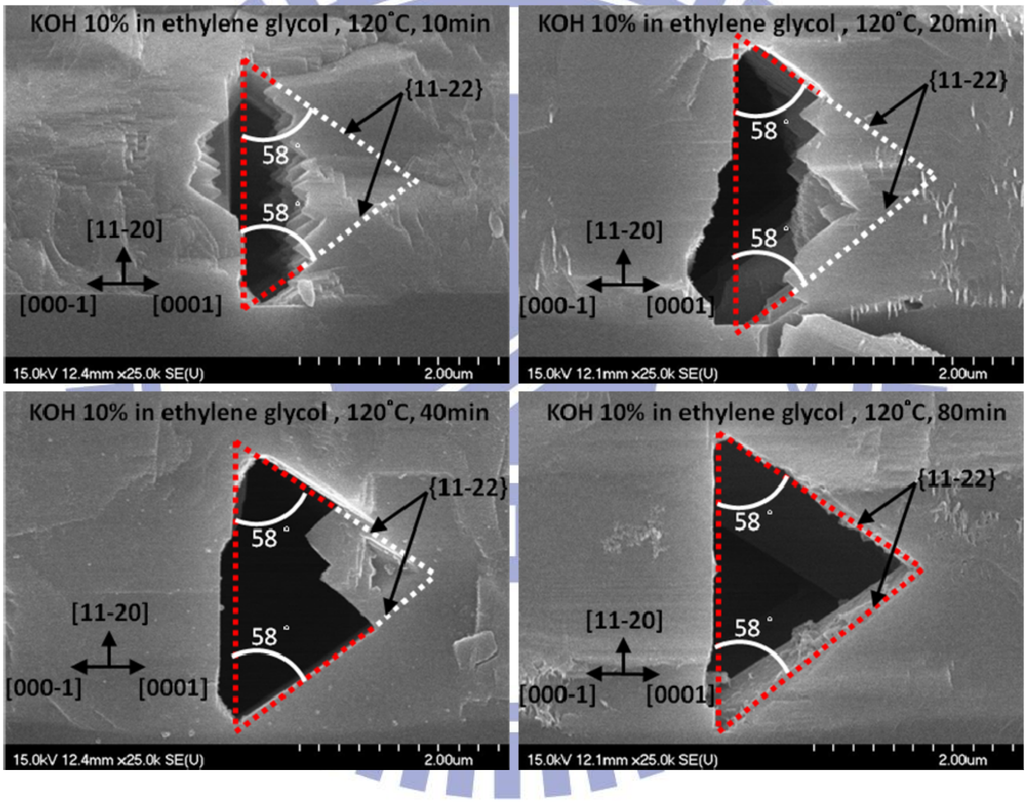

Figure 6.16. Time-dependent SEM images of the air-voids in TELOG *a*-plane GaN under KOH 10 wt. % and 120°C. The corresponding etching geometries and the related crystalline directions are depicted.

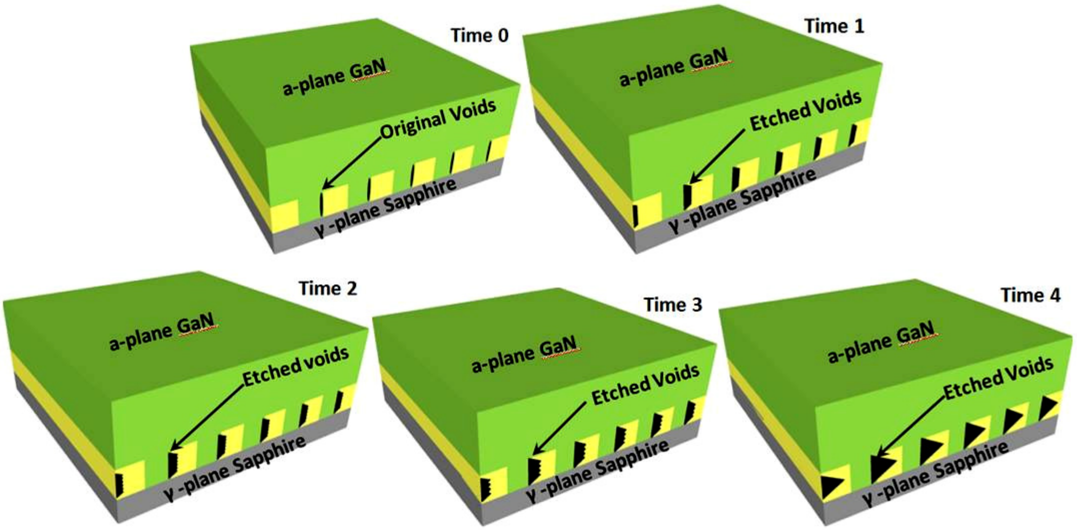

Figure 6.17. Schematic images of the air-voids in TELOG *a*-plane GaN under KOH solutions. The corresponding etching geometries and the related time are depicted.

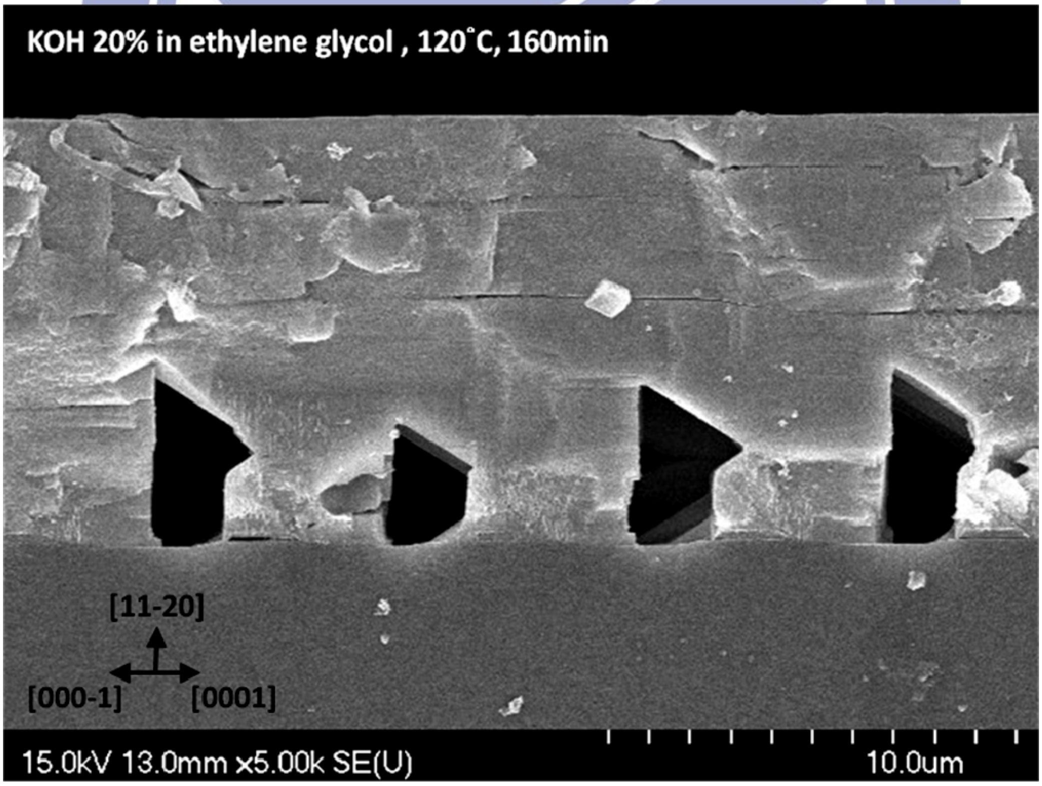

Figure 6.18. SEM images of the air-voids in TELOG *a*-plane GaN under KOH 20 wt. % and 120°C. The etching time is 160 min.

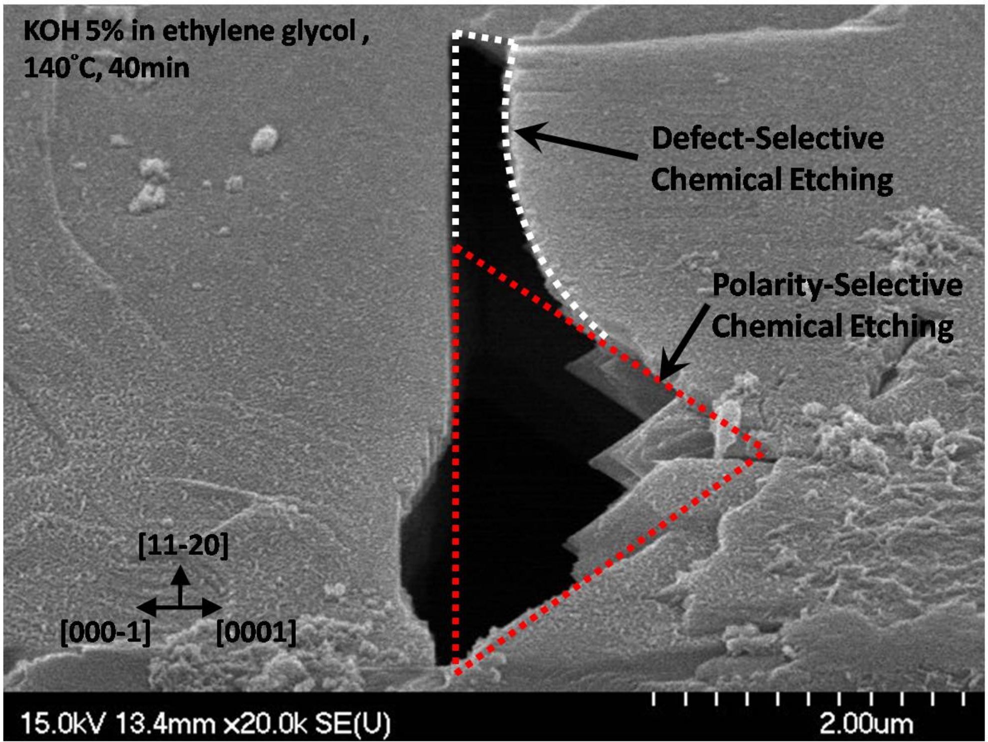

Figure 6.19. SEM images of the air-voids in TELOG *a*-plane GaN under KOH 5 wt. % and 140°C. The etching time is 40 min.

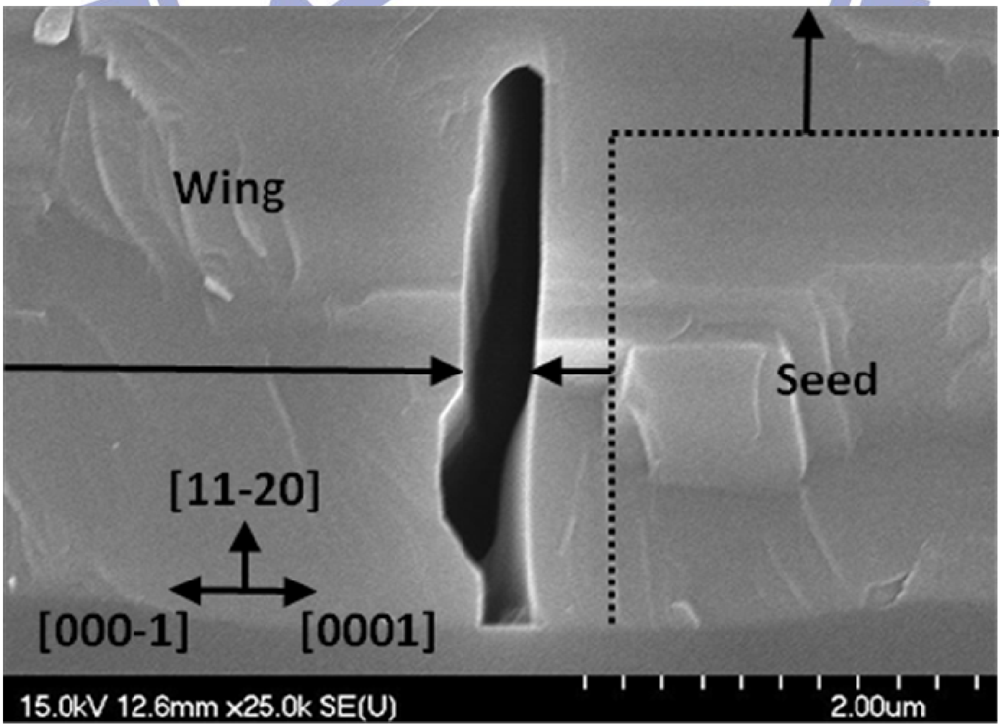

Figure 6.20. SEM images of the original air-voids in TELOG *a*-plane GaN.

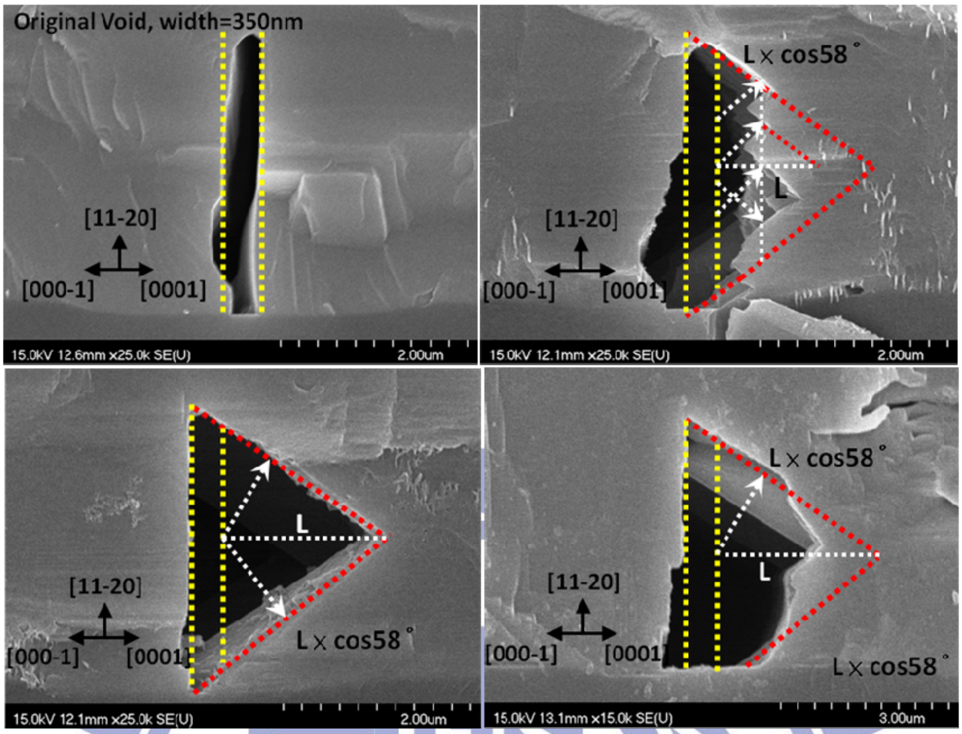

Figure 6.21. The methods of determining the etching rate of the air-voids in TELOG *a*-plane GaN under KOH etching.

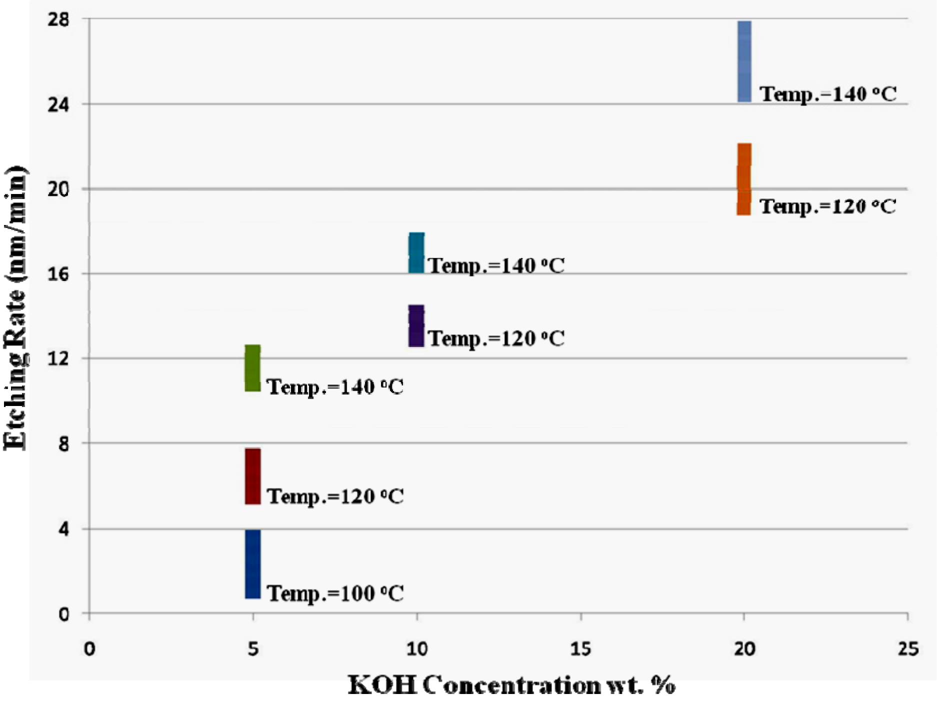

Figure 6.22. The etching rate of the air-voids in TELOG *a*-plane GaN under different KOH etching conditions.

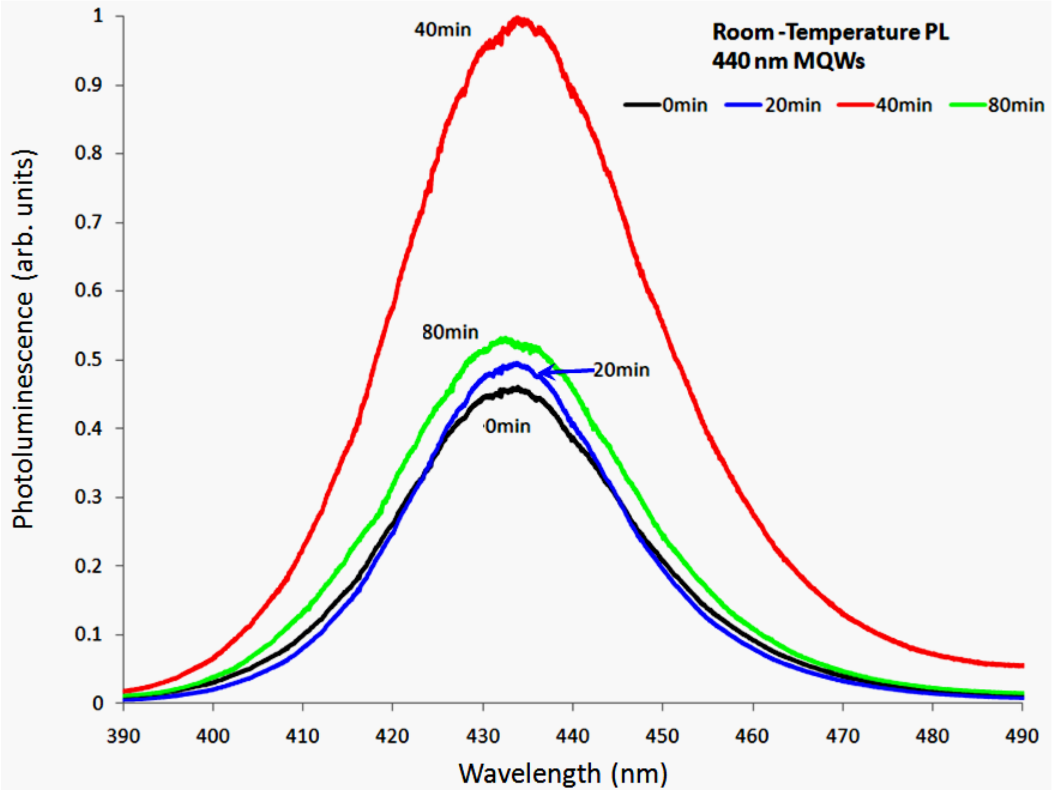

Figure 6.23. PL spectrum of the TELOG *a*-plane 440nm InGaN/GaN MQWs after different KOH etching time. The detector was located normal to the TELOG *a*-plane sample.

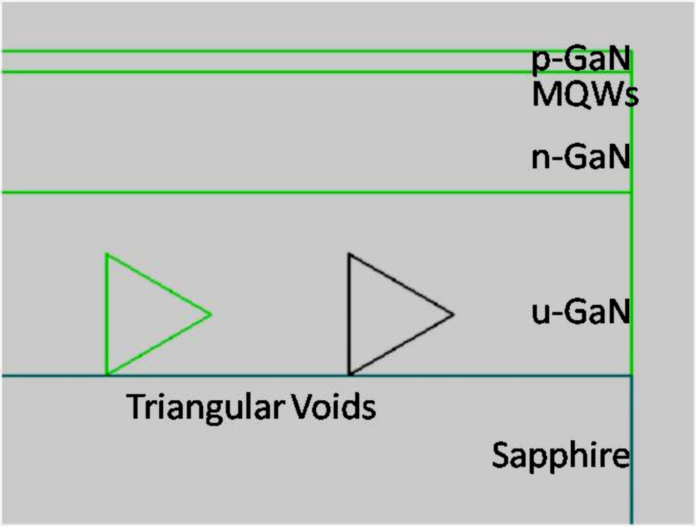

Figure 6.24. The TracePro model to simulate the effects of the air-voids on the light trajectories.

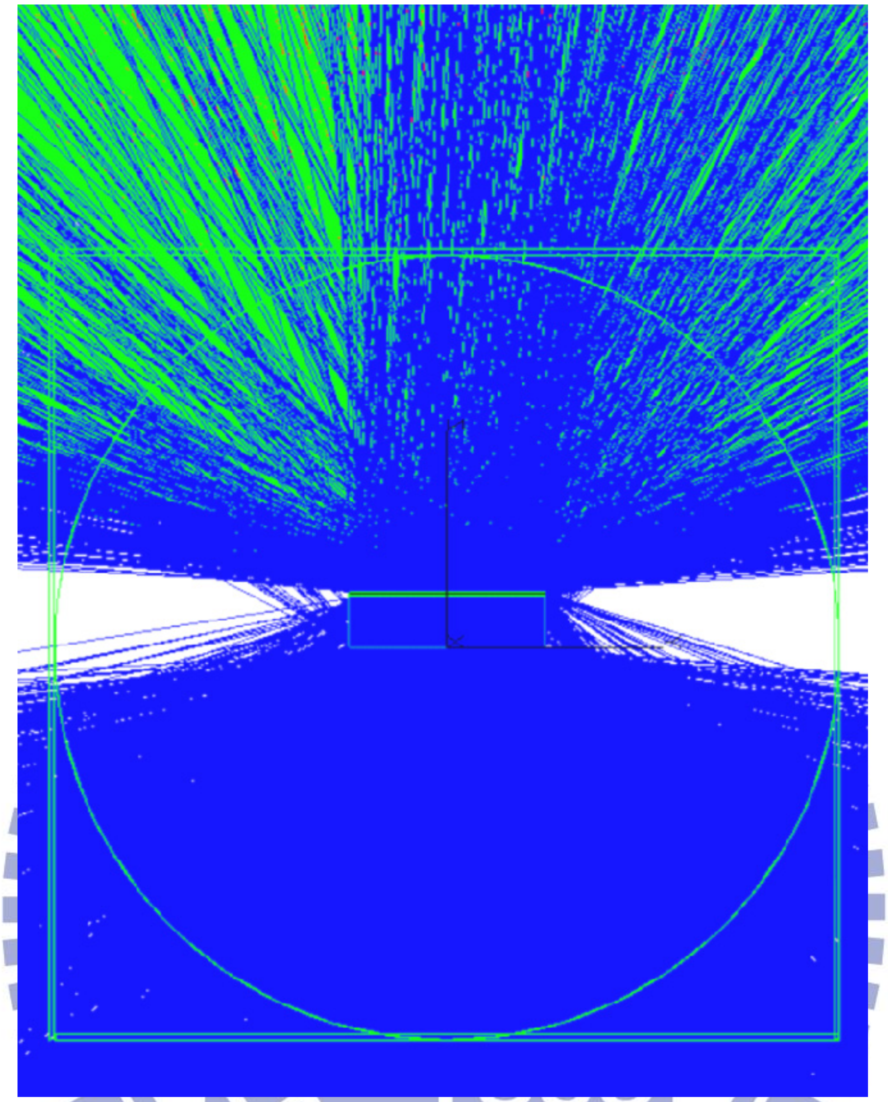

Figure 6.25. The TracePro simulation result of the effects of the air-voids on the light trajectories.

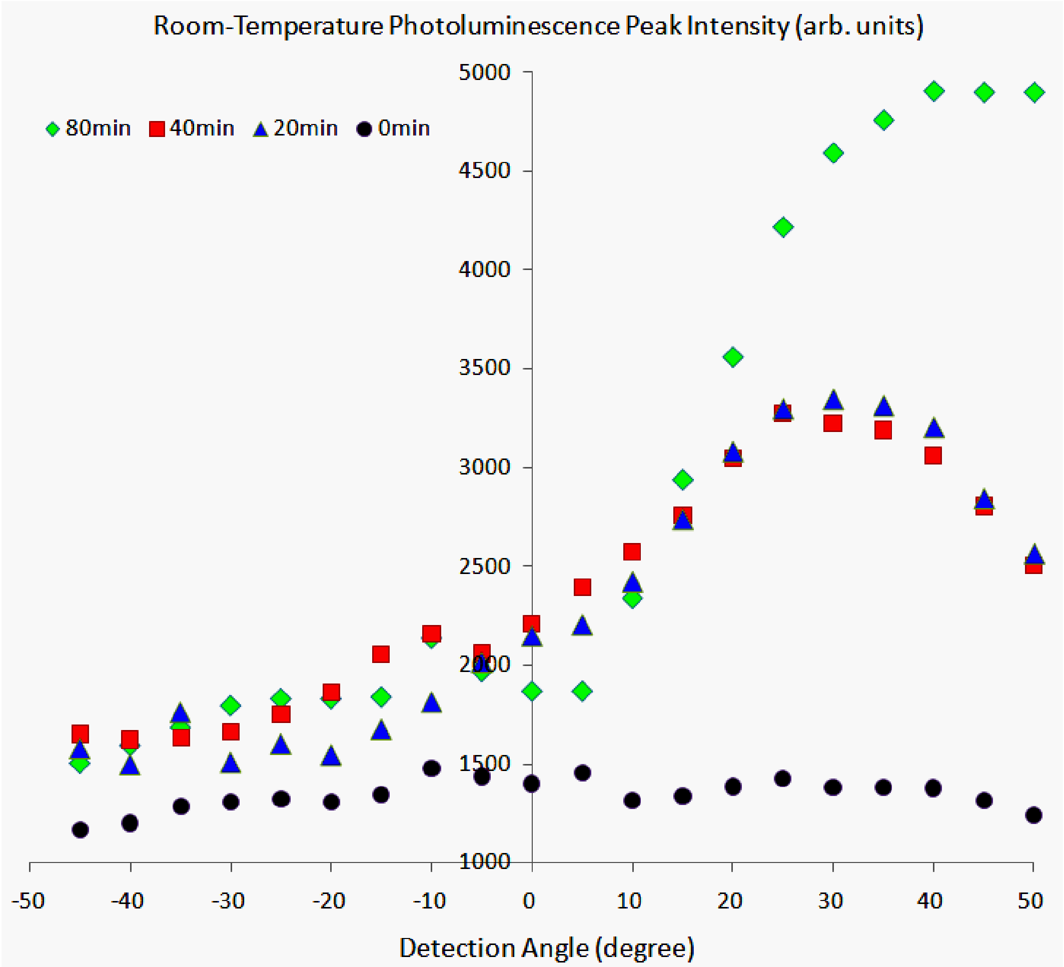

Figure 6.26. Room temperature PL intensity at varied angle. The angle variation was performed by changing (rotating) the position of detector.

Chapter 7

Conclusion and Prospects

7.1 The Acquirement of Nonpolar *a*-Plane GaN on *m*-Plane and *γ*-Plane Sapphire Substrate

Nonpolar GaN, *a*-plane GaN have been acquired on the *γ*-plane sapphire substrate via the TELOG techniques on the basis of the knowledge from *a*-plane GaN epitaxy on patterned *m*-plane sapphire.

A-plane GaN epitaxy on patterned *m*-plane sapphire shows the growth mechanism and the direction of condition tuning. What's more, the distribution of the defects also inspired the modification of substrate design and growth technique improvement. All these lead to the achievement of completely planar *a*-plane GaN on TELOG *γ*-plane sapphire substrate. The InGaN/GaN MQWs are also grown on the *a*-plane GaN with good emission qualities.

In brief, the nonpolar high quality *a*-plane GaN is available for further high-power solid state lighting application. The further efforts needed is the observation in detail the formation mechanism, the elimination and the effect of defects such as stacking faults, dislocations on the optoelectronics properties.

Another related topic is to fix the decrease in efficiency with increased current. It is often called "efficiency-droop effect". The nonpolar GaN shows great potential to overcome the giant gap of the droop effect, and under expectation, more nonpolar

GaN commercial products will come to the solid state lighting markets.

7.2 The Outcome of KOH-Ethylene Glycol-Solution-Etched TELOG Nonpolar *a*-Plane GaN and MQWs

The KOH-ethylene glycol-solution etching results are summarized in chapter 6. It provides an integration process of fabrication into the nonpolar GaN and InGaN/GaN MQWs. The power of the integration of these two methods, nonpoar and air-void engineering, explored the realm of the etching and light extraction in nonpolar devices, which is different to those of the conventional, commercial *c*-plane lighting devices.

The clarification of the etching mechanism of GaN-related materials in KOH-ethylene glycol-solution can be applied to wide region of the device fabrication of compound semiconductors. The basic, fundamental etching mechanism gives the most powerful techniques to the fabrication processes and the potential of application in variety of realms.

7.3 Future works and Prospects

The completely planar *a*-plane GaN on patterner *m*-plane sapphire needs more efforts to achievement. One possible way is covering one of the vertical side-walls of the etched trenches. The one-side-wall passivation leads to the growth of the *a*-plane GaN from the *c*-plane side-wall on only one direction. It effectively prevents the epitaxial GaN from hindering each other. On the other hand, the low-growth-rate –*c*-plane can be met by the high-growth-rate +*c*-plane and perform the coalescence *a*-plane GaN plane on patterned *m*-plane sapphire.

The KOH-ethylene glycol-solution etching results open a door to the solution of sapphire substrate lift-off. The conventional methods are laser lift-off which introduces a plenty of damages into the lighting devices. Chemical-solution based lift-method is appropriate for it introduces almost no damages to the devices. By combining the etching mechanism established in the chapter 6 of the thesis and the specific design of the TELOG seed/trench width ratio, the KOH-ethylene glycol-solution etching can effectively etch the sapphire / dislocation-filled GaN interface leading to the desired “Chemical Lift-Off”.

Another application is that the KOH-ethylene glycol-Solution can remove the low crystalline quality seed GaN and leaves the high quality lateral epitaxial part. The leaved high quality lateral epitaxial part would act as the secondary seed for further overgrowth once again. We expect that the nonpolar GaN epitaxy layer with extremely high crystalline quality over the whole plane is achievable.

Publication List

Conference：

[1] **Kai-Lin Chuang**, Jet-Rung Chang, Shih-Pang Chang, Po-Min Tu, Yu-Cheng Hsu, Wan-Yi Chen, Hsiao-Wen Zan, Tien-Chang Lu, Hao-Chung Kuo, Chun-Yen Chang, "**Growth Mechanism of Nonpolar *A*-Plane GaN on Patterned *M*-Plane Sapphire**", accepted by 2010 ***Solid State Devices and Materials (SSDM)***, Tokyo, Japan.

[2] **Kai-Lin Chuang**, Jet-Rung Chang, Po-Min Tu, Ching-Hsueh Chiu, Yun-Jin Li, Hsiao-Wen Zan, Hao-Chung Kuo, Chun-Yen Chang, "**An Investigation of GaN-Based LED with MBE Grown Nanopillars by MOCVD**", accepted by 2010 ***Solid State Devices and Materials (SSDM)***, Tokyo, Japan.

Curriculum Vitae

Name: Kai-Lin Chuang

Birthday: February 8th, 1986

Address: Room 1, 7th floor, No 15, Chia-Nan Street, Chia-Yi City,
Taiwan, R.O.C.

Education:

National Chia-Yi Senior High School
(From September, 2001 to June 2004)

Department of Materials Science and Engineering, National Chiao Tung University
(From September, 2004 to June 2008)

Institute of Electronics, National Chiao Tung University
(From September, 2008 to July 2010)

Master Thesis:

Integration of Nonpolar *A*-Plane Gallium Nitride Fabricating and Chemical Etching Processes for Lighting Efficiency Enhancement of Light-Emitting Diodes